HYPERONS IN NUCLEAR MATTER AND SU(3) CHIRAL EFFECTIVE FIELD THEORY

Dominik Gerstung

June, 2020

Technische Universität München

Technische Universität München
Physik Department
Institut für Theoretische Physik T39

Hyperons in nuclear matter and SU(3) chiral effective field theory

Dominik Gerstung, M. Sc.

Vollständiger Abdruck der von der Fakultät für Physik der Technischen Universität München zur Erlangung des akademischen Grades eines

Doktors der Naturwissenschaften (Dr. rer. nat.)

genehmigten Dissertation.

Vorsitzender:		Prof. Dr. Stefan Schönert
Prüfer der Dissertation:	1.	apl. Prof. Dr. Norbert Kaiser
	2.	Prof. Dr. Björn Garbrecht

Die Dissertation wurde am 08.06.2020 bei der Technischen Universität München eingereicht und durch die Fakultät für Physik am 29.07.2020 angenommen.

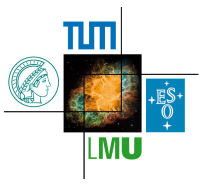

This work has been supported in part by the DFG and the NSFC through funds provided to the Sino-German CRC 110 "Symmetries and the Emergence of Structure in QCD", the Excellence Cluster "Origin and Structure of the Universe", the Excellence Cluster ORIGINS, the TUM Graduate School, and the Wilhelm und Else Heraeus-Stiftung.

ABSTRACT

The Brueckner G-matrix formalism is employed to calculate the single-particle potentials of nucleons and hyperons in isospin-symmetric nuclear matter and pure neutron matter. The underlying YN interactions consist of NLO chiral two-baryon potentials and effective density-dependent baryon-baryon interactions. We compare the chemical potential of Λs against that of neutrons in order to investigate the critical density for the onset of Λ-formation in pure neutron matter. The YNN three-body force depends on two undetermined short-distance parameters H_1 and H_2, whose ranges are explored by imposing empirical constraints from Λ-hypernuclei.

ZUSAMMENFASSUNG

Mithilfe des Brueckner G-matrix-Formalismus werden die Ein-Teilchen-Potentiale von Nukleonen und Hyperonen in Isospin-symmetrischer Kernmaterie und reiner Neutronenmaterie berechnet. Die zugrunde liegenden YN-Wechselwirkungen bestehen aus nächst-führenden chiralen Zwei-Baryon-Potentialen und effektiven dichteabhängigen Baryon-Baryon-Wechselwirkungen. Wir vergleichen das chemische Potential von Λ-Hyperonen mit dem von Neutronen, um die für die Entstehung von Λs kritische Dichte zu untersuchen. Die YNN-Dreikörperkraft hängt von zwei unbestimmten Parametern H_1 und H_2 ab, deren Wertebereich mithilfe von empirischen Bedingungen aus Λ-Hyperkernen untersucht wird.

PUBLICATIONS

1. Dominik Gerstung, Norbert Kaiser, and Wolfram Weise. “Hyperon-nucleon three-body forces and strangeness in neutron stars.”, arXiv: 2001.10563 [nucl-th] .

CONTENTS

1

INTRODUCTION

At the end of their lifetime, stars of sufficiently large mass collapse into neutron stars, with a radius in the order of 10 km and a mass typically ranging around $1.4\,M_\odot$. Their high density, which exceeds that of atomic nuclei, makes them interesting not only from an astronomical point of view, but also from a nuclear physical one. The observation of neutron stars with masses of $1.97 \pm 0.04\,M_\odot$ [2], $2.01 \pm 0.04\,M_\odot$ [3] and, more recently, $2.14^{+0.10}_{-0.09}\,M_\odot$ [4] imposes strong constraints on the equation of state (EoS) of neutron star matter.

The exact composition of neutron stars is still up to debate. While the proton and lepton fractions, which vary in the few percentage range between the multiple layers of betastable matter, has been fairly well established, further degrees of freedom are also being explored. In particular, the density in neutron stars gets so high that initial considerations indicate the appearance of Λ and Σ hyperons [5]. However, the inclusion of hyperons as additional degrees of freedom would soften the EoS too much and contradict the observation of the aforementioned heavy neutron stars. This is called the *hyperon puzzle*.

Ever since the introduction of the *strange* quantum number in the early 1950s, strangeness nuclear physics has been of much interest from both an experimental and theoretical point of view, with the Λ being the most prominent strange baryon. For a review, see Ref. [6]. In particular, numerous techniques have been applied to explore the role of strangeness in neutron stars [7–22]. For example, it was shown that the introduction of phenomenological repulsive ΛNN three-body forces may restore the required stiffness of the EoS [7].

While phenomenological models provide a very good description of the underlying interactions, both in the two-body- [23–25] and three-body-sector [26–30], there is a desire for more systematic approaches that allow for a consistent use of many-body forces. Chiral effective field theory (ChEFT) provides the necessary tool, with many-body forces arising in the same framework as two-body forces and the perturbative nature allowing for uncertainty estimates [31, 32]. Nucleon potentials are available at very high precision from SU(2) ChEFT both for two-body [33–36] and three-body forces [37–46], with three-nucleon interactions being an essential tool for calculations of nuclei [47] or fitting neutron-deuteron scattering data [37]. In the strangeness sector, the potentials are less advanced, because the limited amount of YN scattering data [48–50] makes it unfeasible to proceed to higher orders. The two-body potentials from chiral SU(3) interactions are available at NLO [51] and leading contributions to three-body forces (3BF) have been explored at NNLO [52]. Similar to the nucleon sector, hyperon-nucleon-nucleon 3BFs are essential for hypernuclei and hypernuclear matter [53–61]. Further progress has been made by transcribing the leading three-body forces to density-dependent effective two-body forces, both in the nucleonic- [62, 63] and the hyperonic sector [64].

In this work, we will utilize Brueckner theory in the Brueckner-Hartree-Fock approximation, with input potentials from ChEFT. A first study of this kind was done in Ref. [65], where YN two-body potentials were taken from ChEFT at NLO and ΛNN three-body forces were included as density dependent two-body forces. It was shown that the inclusion of 3-baryon interactions provides the expected repulsive effect on the Λ single-particle potential U_Λ [65],

indeed indicating that the onset of Λ-formation is pushed to higher densities. Similar results were obtained in Ref. [66], where also $\Lambda NN - \Sigma NN$ interactions were considered.

As a novelty, we extend the calculations to higher densities (3.5 times nuclear saturation density) and include all three-baryon interactions for strangeness $S = -1$, namely the $\Lambda NN - \Lambda NN$, $\Lambda NN - \Sigma NN$, and $\Sigma NN - \Sigma NN$ transitions. For this purpose, we derive the expressions for the density-dependent two-body interactions $\Lambda N - \Sigma N$, and $\Sigma N - \Sigma N$ in general (isospin-asymmetric) nuclear matter.

This thesis is organized as follows. First, in chapter 2 we will review how two-body potentials can be systematically built from ChEFT and focus on the YN interactions. In chapter 3, we recapitulate how three-body potentials are obtained in the same framework. Afterwards, we summarize how they are transcribed to density-dependent two-body forces and perform this procedure for the YNN 3BFs involving Λ or Σ. Chapter 4 deals with the basics of Brueckner G-matrix theory, introducing the G-matrix as the sum of in-medium ladder diagrams, which are summed to all orders by the Bethe-Goldstone equation. The single-particle potential is given in the Brueckner-Hartree-Fock approximation. The self-consistent solution of this set of coupled integral equations will then be discussed from a numerical point of view. Results are presented in chapter 5. We will spell out technical challenges and how to overcome them, compare results for nucleons in the medium against the literature and then turn to the strange sector. Finally, in chapter 6 we summarize our results.

Notations are listed in the appendix.

2

SU(3) CHIRAL EFFECTIVE FIELD THEORY

There are four fundamental forces in nature: gravity, electromagnetism, weak interaction, and strong interaction, of which the last three are described by the Standard Model of particle physics. At the *fundamental* level, the strong interactions are described by *Quantum Chromodynamics* (QCD).

In QCD the fundamental degrees of freedom are quarks and gluons, which make up all hadronic matter. Quarks are spin-$\frac{1}{2}$ fermions and come in six flavors: up (u), down (d), strange (s), charm (c), top (t), and bottom (b), sorted by their mass in ascending order. The eight gluons, on the other hand, are gauge bosons (i.e. exchange particles) of spin 1. Quarks possess a charge called *color* (red, green, or blue), historically introduced to resolve the violation of the Pauli principle for Δ^{++}-baryons (uuu) and Ω^{-}-baryons (sss). In experiments, however, we can only observe *white* (i.e. colorless) particles. This phenomenon is explained by *color-confinement*. As opposed to quantum electrodynamics (QED) where the gauge bosons (photons) are not electrically charged, the gluons actually possess a color charge and thus have self interactions. Hence the strong force does not get weaker with increasing distance, so that at some point the production of a quark-antiquark pair becomes energetically favorable over separating the quarks further. This process is observed in collider experiments, for example, when jets of colorless hadrons are detected instead of single quarks (*hadronization*).

In QCD the coupling constant α_s is not weak in general. It depends on the energy scale (*running coupling*) and decreases for high energies. This makes perturbative approaches in powers of α_s only applicable for large energies (unlike QED, for example, with $\alpha \approx \frac{1}{137}$). Due to this difficulty, numerical techniques to solve QCD by lattice simulations [69–72] have been developed in the past. Some insights into QCD can also be obtained by the large-N_C expansion, with N_C the number of colors [73–75]. One approach in particular, chiral effective field theory (ChEFT), is very successful for the low energy regime and will be the basis of the calculations in this work. Therefore, this chapter is dedicated to the introduction of ChEFT on a fundamental level, exhibiting the key ideas and components. We follow [31, 32, 76], to which the interested reader is referred for more details. First, we will review the basics of QCD and highlight its symmetry properties. After that, we show how ChEFT naturally arises from spontaneous symmetry breaking and construct the building blocks used to assemble the chiral Lagrangians. Then the mesonic and baryonic SU(3) Lagrangians are given up to the orders required for the further discussion. Finally, the resulting two-baryon potentials are presented.

2.1 QUANTUM CHROMODYNAMICS

The free quark Lagrangian of QCD reads

$$\mathcal{L}_{\text{QCD,free}} = \sum_{f,c} \bar{q}_f^{(c)} (i\not{\partial} - m_f) q_f^{(c)} \,, \tag{2.1}$$

with the sum going over six flavors $f \in \{u, d, s, c, t, b\}$ and three colors $c \in \{r, g, b\}$ for a total of 18 terms. For the sake of brevity, all quark fields will be merged into a multi-component vector q, with the masses m_f becoming an appropriately structured diagonal matrix m.

2.1.1 *Symmetries of QCD*

Symmetries are an indisposable tool in physics, giving valuable insights into systems and processes. QCD possesses a variety of symmetries, of which a few will be discussed in the subsections below. A key feature of symmetries is stated by Noether's theorem:

For every generator of a continuous symmetry, there exists a conserved current.

Formally, an infinitesimal transformation of the form

$$\phi(x) \to \phi(x) + \alpha \Delta\phi(x)\,, \tag{2.2}$$

with a parameter α and associated field change $\Delta\phi(x)$, which leaves the Lagrangian $\mathcal{L}(\phi, \partial_\mu\phi)$ invariant, gives rise to the conserved current

$$j^\mu(x) = \frac{\partial\mathcal{L}}{\partial(\partial_\mu\phi)}\Delta\phi, \qquad \text{with } \partial_\mu j^\mu(x) = 0\,. \tag{2.3}$$

Equivalently, the charge

$$Q = \int j^0 d^3x, \qquad \text{with } \partial_0 Q = 0 \tag{2.4}$$

is time-independent.

Discrete symmetries

Before we deal with continuous symmetries, we consider discrete ones first. The QCD Lagrangian is invariant under the transformations

- charge conjugation C (particle $\leftrightarrow$ antiparticle interchange)
- parity P (space inversion)
- time reversal T

with quarks transforming under them as

$$\begin{aligned} C : q(t,\vec{x}) &\to -i(q\gamma^0\gamma^2)^T\,, \\ \bar{q}(t,\vec{x}) &\to -i(\gamma^0\gamma^2\bar{q})^T\,, \end{aligned} \tag{2.5}$$

$$\begin{aligned} P : q(t,\vec{x}) &\to \gamma^0 q(t,-\vec{x})\,, \\ \bar{q}(t,\vec{x}) &\to \bar{q}(t,-\vec{x})\gamma^0\,, \end{aligned} \tag{2.6}$$

$$\begin{aligned} T : q(t,\vec{x}) &\to \gamma^1\gamma^3 q(-t,\vec{x})\,, \\ \bar{q}(t,\vec{x}) &\to -\bar{q}(-t,\vec{x})\gamma^1\gamma^3\,. \end{aligned} \tag{2.7}$$

As a side remark, we note that experiments indicate that gravity, electromagnetism, and the strong force are C, P, and T invariant. However, the weak interaction was found to be parity-violating in 1956 [77] and CP-violating in 1964 [78]. The strong interaction could potentially

violate CP symmetry through the so-called θ-term, but no conclusive observations have been made. Actually, measurements of the (upper limit) of the neutron electric-dipole moment [79] set severe limits on the magnitude of this violation. Strong CP-violation remains an open problem in nuclear and particle physics. In any case, up to now all observed processes in nature exhibit CPT symmetry.

$SU(3)_C$ color symmetry

Even though the strong force acts on color charge, it does not distinguish between different colors. Therefore, the Lagrangian has a global symmetry under unitary transformations within color space:

$$\begin{pmatrix} q'_r \\ q'_g \\ q'_b \end{pmatrix} = q' = Uq = U \begin{pmatrix} q_r \\ q_g \\ q_b \end{pmatrix}, \qquad U \in \mathrm{SU}(3)\,. \tag{2.8}$$

When this symmetry holds at each point in space-time individually, the symmetry group $\mathrm{SU}(3)_C$ is said to be *local*, i.e. we require the invariance to still hold under a coordinate-dependent transformation $U = U(x)$. To accommodate for the extra term that arises from the product rule of the partial derivative in eq.(2.1), the derivative must be promoted to a covariant one:

$$D_\mu \coloneqq \partial_\mu - ig\Gamma_\mu \tag{2.9}$$

by introducing 8 gauge fields A^a_μ (identified with the gluons) via the hermitian and traceless[1] connection

$$\Gamma_\mu = \sum_{a=1}^{8} A^a_\mu \frac{\lambda_a}{2}\,, \tag{2.10}$$

with the Gell-Mann matrices λ_a. The gluon field constitutes a further building block for the QCD Lagrangian, allowing to build a Lorentz tensor by introducing the gluon field-strength

$$G^c_{\mu\nu} = \frac{i}{g}[D_\mu, D_\nu] = \partial_\mu A^c_\mu - \partial_\nu A^c_\mu + g f^{cde} A^d_\mu A^e_\nu\,, \tag{2.11}$$

with f^{cde} the (totally antisymmetric) structure constants of the $\mathfrak{su}(3)$ Lie algebra. The full[2] QCD Lagrangian then reads:

$$\mathcal{L} = q(i\not{D} - m)q - \frac{1}{4} G_{\mu\nu,a} G^{\mu\nu}_a\,. \tag{2.12}$$

In total, QCD is classified as a non-abelian gauge theory with an $\mathrm{SU}(3)_C$ symmetry. Therefore, it is a special case of a Yang-Mills theory.

1 A priori, we could use non-traceless matrices as well and accordingly have transformations $U \in U(3)$. However, this would imply the existence of color-singlet gluons. The associated long-range strong forces are not observed.

2 In principle one could also add the CP-violating term $\mathcal{L} = \frac{g_c^2 \theta}{64\pi^2} \epsilon_{\mu\nu\rho\sigma} G^{\mu\nu,a} G^{\rho\sigma,a}$.

2.1.1.1 *Chiral SU(N_f) symmetry*

In the limit of massless quarks (*chiral limit*), the left- and right-handed components of quarks, $q_{L,R}$, are independently invariant under flavor transformations, which is called *chiral symmetry*. The corresponding projection operators are

$$q_{R,L} \coloneqq P_{R,L}\, q\,, \qquad \text{with} \quad P_{R,L} = \frac{1}{2}(1 \pm \gamma_5)\,. \tag{2.13}$$

The name left- and right-handed stems from the fact that in the massless limit, free Dirac particles are eigenstates of the helicity operator, which projects a particle's spin onto its momentum:

$$\hat{h} q_{L,R} = \pm q_{L,R}\,, \qquad \text{with } \hat{h} = \frac{\vec{\sigma}\cdot\vec{p}}{|\vec{p}|}\,. \tag{2.14}$$

In the chiral limit, the Lagrangian becomes

$$\mathcal{L} = \bar{q}_R i \not{D} q_R + \bar{q}_L i \not{D} q_L - \frac{1}{4} G_{\mu\nu,a} G_a^{\mu\nu}\,, \tag{2.15}$$

with an apparent independence of the right- and left-handed quarks. The Lagrangian then is invariant under continuous unitary transformations in flavour space, denoted by the symmetry group $\mathrm{U}(N_f)_L \times \mathrm{U}(N_f)_R \cong \mathrm{SU}(N_f)_L \times \mathrm{SU}(N_f)_R \times \mathrm{U}(1)_L \times \mathrm{U}(1)_R$, with N_f being the number of (light) flavors, which is chosen to be either 2 (up, down) or 3 (up, down, strange)[3], of which the latter is adopted in this work. From these continuous symmetries, we get $8+8+1+1=18$ right- and left-handed Noether currents:

$$L_\mu^a = \bar{q}_L \gamma_\mu \frac{\lambda_a}{2} q_L\,, \tag{2.16}$$

$$R_\mu^a = \bar{q}_R \gamma_\mu \frac{\lambda_a}{2} q_R\,, \tag{2.17}$$

$$L_\mu = \bar{q}_L \gamma_\mu q_L\,, \tag{2.18}$$

$$R_\mu = \bar{q}_R \gamma_\mu q_R\,. \tag{2.19}$$

For the further discussion, it is instructive to combine them into vector and axial vector currents:

$$V_\mu^a = R_\mu^a + L_\mu^a = \bar{q}\gamma_\mu \frac{\lambda_a}{2} q\,, \tag{2.20}$$

$$A_\mu^a = R_\mu^a - L_\mu^a = \bar{q}\gamma_\mu\gamma_5 \frac{\lambda_a}{2} q\,, \tag{2.21}$$

$$V_\mu = R_\mu + L_\mu = \bar{q}\gamma_\mu q\,, \tag{2.22}$$

$$A_\mu = R_\mu - L_\mu = \bar{q}\gamma_\mu\gamma_5 q\,. \tag{2.23}$$

The corresponding conserved charges, as given by eq. (2.4), generate a Lie algebra

$$\left[Q_{L,R}^a, Q_{L,R}^b\right] = i f_{abc} Q_{L,R}^c\,, \tag{2.24}$$

$$\left[Q_L^a, Q_R^b\right] = 0\,, \tag{2.25}$$

$$\left[Q_{L,R}^a, Q_V\right] = 0\,. \tag{2.26}$$

The symmetry group may now equivalently be written as $\mathrm{SU}(3)_L \times \mathrm{SU}(3)_R \times \mathrm{U}(1)_V \times \mathrm{U}(1)_A$.

While being conserved in the classical field theory, the singlet axial current $A_\mu = \bar{q}\gamma_\mu\gamma_5 q$ is not conserved at the quantum level any more, which is referred to as the *chiral anomaly*.[4]

3 The masses of the charm, top and bottom quarks are too large, making larger flavor symmetry groups unfeasible.

4 The Adler-Bell-Jackiw anomaly [80–82] is responsible for the processes $\gamma \to \gamma\gamma$ or $\pi^0 \to \gamma\gamma$.

Therefore it is common to say that QCD possesses a $\mathrm{SU}(3)_L \times \mathrm{SU}(3)_R \times \mathrm{U}(1)_V$ symmetry in the chiral limit.

2.1.2 *Spontaneous symmetry breaking*

There is strong experimental evidence to assume that the axial symmetry of the Lagrangian is spontaneously broken, i.e. it is a symmetry of the system, but not of the ground state:
Since Q_V^a commutes with the Hamiltonian and has negative parity, one would naively expect the existence of degenerate doublets of opposite parity, but these are not observed. For example, the ρ meson ($J^P = 1^-$) has a 1^+ partner, the a_1 meson, but their masses of 770 MeV and 1230 MeV, respectively, are too different for them to be seen as degenerate. Consequently, this naive realization of chiral symmetry turns out to be false, which points to the aforementioned broken symmetry in the ground state: $Q_A^a |0\rangle \neq 0$. In such a situation Goldstone's theorem applies: [83, 84]

> For every generator of a spontaneously broken continuous symmetry, there exists one massless boson, called a (Nambu-)Goldstone boson.

Since the axial symmetry has eight generators, this gives rise to eight Goldstone bosons, which are identified with the three pions $(\pi^\pm, \pi^0)$, the four kaons $(K^\pm, K^0, \bar{K}^0)$ and the eta-meson (η). In the simpler case of $N_f = 2$, there would be only three broken generators, whose corresponding Goldstone bosons are identified with the pions.

The above discussion is only approximate, because we have assumed vanishing quark masses, i.e. $m_{u,d,s} = 0$. Once the masses are set to their finite values, the left- and right handed quark fields get coupled via the mass term

$$\mathcal{L}_M = \bar{q} M q = q_L m q_R + q_R m q_L \,, \tag{2.27}$$

which breaks some of the flavor symmetries. Now the octet vector currents A_μ^a and V_μ^a are not conserved anymore in general. V_μ^a are still conserved in the SU(3) limit $0 \neq m_u = m_d = m_s$. The singlet vector current is always conserved, even for non-vanishing and different quark masses. It corresponds to baryon number conservation.

The mass terms also have a consequence for Goldstone's theorem: Since the axial symmetry is not exact in the first place, the Goldstone bosons are no more massless, but receive a mass whose square is proportional to the extent of the chiral symmetry breaking. They are then referred to as *pseudo-Goldstone bosons*. Since the strange quark's mass is much larger than those of the up and down quarks, axial SU(3) is more broken than axial SU(2), leading to the kaons and η having a higher mass than the pions.

2.1.3 *External field method*

A particular object of interest in quantum field theory are Green's functions (also known as correlation functions), which are vacuum expectation values of time-ordered products of e.g. currents. Divergences thereof can be related to other Green's functions. These relations are called *Ward identities*. If the Green's function contains at least one V_μ^a or A_μ^a, the emerging relation is called a *chiral Ward identity*.

Since there exist infinitely many identities, it is more useful to formally combine all Green's functions into a generating functional. Consequently, the Ward identities express its invariance properties. Following the approach of Ref. [85], the generating functional reads

$$\exp(iZ[v,a,s,p]) = \langle 0|\, T \exp\left(i \int d^4x \mathcal{L}_{\text{ext}} \right) |0\rangle \ , \tag{2.28}$$

where we have introduced the 8 (hermitian) vector, axial-vector, scalar, and pseudoscalar external sources

$$v^\mu = \sum_{a=1}^{8} v_a^\mu \frac{\lambda_a}{2} \, , \qquad a^\mu = \sum_{a=1}^{8} a_a^\mu \frac{\lambda_a}{2} \, , \qquad s = \sum_{a=1}^{8} s_a \frac{\lambda_a}{2} + s_0 \, , \qquad p = \sum_{a=1}^{8} p_a \frac{\lambda_a}{2} \, , \tag{2.29}$$

with an implicit space-time dependence. Now Green's functions can be expressed as functional derivatives of $\exp(iZ[v,a,s,p])$ with respect to the external sources.

In QCD the external sources v, a, s, p couple to the vector, axial-vector, scalar and pseudoscalar quark current densities respectively via the additional Lagrangian

$$\mathcal{L}_{\text{ext}} = \bar{q}\gamma^\mu(v_\mu + \gamma_5 a_\mu)q - \bar{q}(s - i\gamma_5 p)q \, . \tag{2.30}$$

Note that the symmetry-breaking mass term $\mathcal{L}_M$ in eq. (2.27) can be recovered by setting $v = a = p = 0$ and $s = diag(m_u, m_d, m_s)$. In order for $\mathcal{L}_{\text{QCD}} + L_{\text{ext}}$ to be invariant under local $\text{SU}(3)_L \times \text{SU}(3)_R$ flavour transformations, the sources must obey the transformation rules[5]

$$v_\mu + a_\mu \to R(v_\mu + a_\mu)R^\dagger + iR\partial_\mu R^\dagger \, , \tag{2.31}$$

$$v_\mu - a_\mu \to L(v_\mu - a_\mu)L^\dagger + iL\partial_\mu L^\dagger \, , \tag{2.32}$$

$$s + ip \to R(s + ip)L^\dagger \, , \tag{2.33}$$

$$s - ip \to L(s - ip)R^\dagger \, , \tag{2.34}$$

with $R, L \in \text{SU}(3)_{R,L}$.

As a side remark, we note that another advantage of this approach is that the coupling to electroweak gauge fields follows by equating certain external vector and axial vector sources with the $W^\pm$ and Z^0 boson fields.

2.2 EFFECTIVE FIELD THEORIES

An effective field theory (EFT) is a low-energy approximation to an underlying theory, where only the lightest degrees of freedom are kept and more massive, particles responsible for the short-distance behavior, are encoded in low-energy constants.

ChEFT is such a low-energy approximation to QCD by treating Goldstone bosons and heavy matter fields (baryons) as explicit degrees of freedom. EFTs are realized by the most general Lagrangian that is consistent with the underlying symmetries:

> "If one writes down the most general possible Lagrangian, including all terms consistent with assumed symmetry principles, and then calculates matrix elements

5 The transformation properties of $s \pm ip$ are verified by decomposing eq. (2.30) into chiral components: $\bar{q}(s - i\gamma_5 p)q = \bar{q}_L(s - ip)q_R + \bar{q}_R(s + ip)q_L$

> with this Lagrangian to any given order of perturbation theory, the result will simply be the most general possible S-matrix consistent with analyticity, perturbative unitarity, cluster decomposition, and the assumed symmetry principles."[86]

The color symmetry $\mathrm{SU}(3)_C$ is not an issue here because of the colorless active degrees of freedom in the EFT. Chiral symmetry and discrete symmetries of QCD require more attention and will be dealt with in subsequent sections.

However, one particular challenge of this approach is that an infinite number of terms will arise in the effective Lagrangian, which at first sight makes calculations prohibitively complex. However, there is a way of ranking each term (and thus every Feynman diagram) by the magnitude of its contribution, through the so-called *power counting*. Up to a given order, there is then only a finite number of terms, accompanied by low-energy-constants (LECs) that parametrize the unresolved short-distance ($\widehat{=}$ high energy) behavior. These LECs can either be obtained from fits to experimental data or computed from the underlying theory.

Every diagram is assigned a certain power $(q/\Lambda_\chi)^\nu$ of the ratio between the involved momentum q and the chiral symmetry breaking scale $\Lambda_\chi \approx 1$ GeV. In particular, for the purely mesonic Lagrangians one finds for the exponent

$$\nu = 2 + 2L + \sum_i v_i \Delta_i \,, \tag{2.35}$$

with L the number of loops and v_i the number of vertices with dimension Δ_i. Here, Δ_i itself is calculated as $d_i - 2$, with d_i being the order of the Lagrangian term which the vertex comes from. If baryons B are involved, the power counting of a connected diagram reads [32]

$$\nu = -4 + 2B + 2L + \sum_i v_i \Delta_i, \qquad \Delta_i = d_i + \frac{b_i}{2} - 2 \,, \tag{2.36}$$

with b_i the number of baryon lines at the vertex i.

2.3 BUILDING BLOCKS OF THE CHIRAL LAGRANGIAN

The goal in this section is to establish a systematic way of constructing the chiral Lagrangian to arbitrary orders by identifying basic "building blocks", whose transformation properties under $G = \mathrm{SU}(3)_L \times \mathrm{SU}(3)_R$, C, and P are well defined.

At higher orders in particular, it becomes important to find a systematic way to construct the complete Lagrangians, especially to reduce the number of redundant terms. The idea is that we want the building blocks to all have the same homogeneous transformation property

$$X \xrightarrow{G} K X K^\dagger \,, \tag{2.37}$$

with $K \in \mathrm{SU}(3)$, which will be defined soon.
In the end, taking the traces over any product of such building blocks will result in a chirally invariant Lagrangian. This will be done explicitly in section 2.4. A list of all final building blocks is given in table 2.1.

building block	P	C	h.c.	order
u_μ	$-$	$+$	$+$	$\mathcal{O}(q^1)$
$\chi_\pm$	$\pm$	$+$	$\pm$	$\mathcal{O}(q^2)$
$f^\pm_{\mu\nu}$	$\pm$	$\mp$	$\pm$	$\mathcal{O}(q^2)$
$(\bar{B}B)$	$+$	$+$	$+$	$\mathcal{O}(q^0)$
$(\bar{B}\gamma_5 B)$	$-$	$+$	$-$	$\mathcal{O}(q^1)$
$(\bar{B}\gamma_\mu B)$	$+$	$-$	$+$	$\mathcal{O}(q^0)$
$(\bar{B}\gamma_5\gamma_\mu B)$	$-$	$+$	$+$	$\mathcal{O}(q^0)$
$(\bar{B}\sigma_{\mu\nu} B)$	$+$	$-$	$+$	$\mathcal{O}(q^0)$

Table 2.1: Transformation properties and chiral order of the building blocks of the effective Lagrangian. All of them transform under G as $X \to KXK^\dagger$. Under parity, a building block X transforms as $X \xrightarrow{P} \pm X$, under charge conjugation as $X \xrightarrow{C} \pm X^T$ and under hermitian conjugation as $X \to X^\dagger = \pm X$. The signs corresponding to each transformation are given in the respective column.

The first chiral building block represents the mesons, for which a convenient way is to collect them in a unitary matrix $U(x)$. It comprises all eight meson fields $\phi_1(x), \ldots, \phi_8(x)$ and has the transformation property

$$U(x) \to RU(x)L^\dagger\,, \tag{2.38}$$

$$U(x)^\dagger \to L^\dagger U(x) R\,, \qquad \text{for } (L,R) \in \mathrm{SU}(3)_L \times \mathrm{SU}(3)_R\,. \tag{2.39}$$

The most common way to express U in terms of ϕ_a is by using the exponential parametrization $U(x) = \exp(i\phi(x)/f_0)$ with the Goldstone boson fields collected as

$$\phi(x) = \sum_{a=1}^{8} \lambda_a \phi_a(x) = \begin{pmatrix} \pi^0 + \frac{1}{\sqrt{3}}\eta & \sqrt{2}\pi^+ & \sqrt{2}K^+ \\ \sqrt{2}\pi^- & -\pi^0 + \frac{1}{\sqrt{3}}\eta & \sqrt{2}K^0 \\ \sqrt{K^-} & \sqrt{2}\bar{K}^0 & -\frac{2}{\sqrt{3}}\eta \end{pmatrix} \tag{2.40}$$

and the pseudoscalar decay constant f_0 in the chiral limit.[6] For instance, it can be related to the pion decay constant (in the chiral limit) entering the decay $\pi^+ \to \mu^+\nu_\mu$ of charged pions.

In order to arrive at the transformation behavior in eq. (2.37), one first introduces - as an auxiliary quantity - the square root of U which transforms like

$$u \coloneqq \sqrt{U} \to \sqrt{RUL^\dagger} =: R\sqrt{U}K^\dagger = K\sqrt{U}L^\dagger. \tag{2.41}$$

The relation defines the compensator field $K \in \mathrm{SU}(3)$ as

$$K(L,R,U) = \sqrt{RUL^\dagger}^{-1} R\sqrt{U}\,. \tag{2.42}$$

Morever, one introduces the quantity

$$u_\mu \coloneqq i\left[u^\dagger(\partial_\mu - ir_\mu)u - u(\partial_\mu - il_\mu)u^\dagger\right]\,, \tag{2.43}$$

6 At lowest order, all pseudoscalar mesons share the same decay constant. This degeneracy will be removed at higher orders when SU(3) symmetry breaking is taken into account. [87]

which has the desired transformation property $u_\mu \to K u_\mu K^\dagger$.

Explicit chiral symmetry-breaking shows up in the QCD Lagrangian via the mass term (2.27). More generally, consider the scalar and pseudoscalar external sources in eq. (2.30). This motivates the quantity $\chi \coloneqq 2B_0(s+ip)$ and the $X \to KXK^\dagger$ transformation behavior holds for

$$\chi_\pm \coloneqq u^\dagger \chi u^\dagger \pm u \chi^\dagger u \,. \tag{2.44}$$

Since $\mathrm{SU}(3)_L \times \mathrm{SU}(3)_R$ has been promoted to a local symmetry, one has to work with a covariant derivative:

$$D_\mu X \coloneqq \partial_\mu X - i r_\mu X + i X l_\mu \,, \tag{2.45}$$

with r_μ the gauge field for $\mathrm{SU}(3)_R$ and l_μ that for $\mathrm{SU}(3)_L$. Accordingly, one gets the field strength tensors:

$$f^R_{\mu\nu} \coloneqq \partial_\mu r_\nu - \partial_\nu r_\mu - i\,[r_\mu, r_\nu] \,, \tag{2.46}$$

$$f^L_{\mu\nu} \coloneqq \partial_\mu l_\nu - \partial_\nu l_\mu - i\,[l_\mu, l_\nu] \,, \tag{2.47}$$

which transform as

$$f^R_{\mu\nu} \xrightarrow{G} R f^R_{\mu\nu} R^\dagger \,, \qquad\qquad f^L_{\mu\nu} \xrightarrow{G} L f^L_{\mu\nu} L^\dagger \,. \tag{2.48}$$

The required transformation property $X \to KXK^\dagger$ is obtained for the quantities

$$f^\pm_{\mu\nu} = u f^L_{\mu\nu} u^\dagger + u^\dagger f^R_{\mu\nu} u \,.$$

Finally, let us turn to baryonic building blocks. The traceless 3×3 matrix B that comprises the octet baryons has the form

$$B = \begin{pmatrix} \frac{1}{\sqrt{2}}\Sigma^0 + \frac{1}{\sqrt{6}}\Lambda & \Sigma^+ & p \\ \Sigma^- & -\frac{1}{\sqrt{2}}\Sigma^0 + \frac{1}{\sqrt{6}}\Lambda & n \\ \Xi^- & \Xi^0 & \frac{-2}{\sqrt{6}}\Lambda \end{pmatrix} \tag{2.49}$$

and it possesses the transformation property $B \xrightarrow{G} K B K^\dagger$.

Now we have all basic building blocks: u_μ, $\chi_\pm$, $f^\pm_{\mu\nu}$, and B. We still have to consider their derivatives. Just like for $\mathrm{SU}(3)_C$ in QCD, the transformations from G are local and thus the derivative must be promoted to a covariant one

$$D_\mu X = \partial_\mu X + [\Gamma_\mu, X] \,, \tag{2.50}$$

with the chiral connection

$$\Gamma_\mu = \frac{1}{2}\left(u^\dagger(\partial_\mu - i r_\mu) u + u(\partial_\mu - i l_\mu) u^\dagger \right) . \tag{2.51}$$

Note that this covariant derivative only applies to objects that transform as $X \to KXK^\dagger$. For building blocks that transform like U the covariant derivative defined in eq. (2.45) is appropriate.

Before we combine all these building blocks into a Lagrangian, we need to know of which chiral order they are. The mesonic building block u_μ scales as $\mathcal{O}(q^1)$, because u is $\mathcal{O}(q^0)$ and a derivative in eq. (2.43) counts as q^1. χ scales as $\mathcal{O}(q^2)$, because it involves the quark masses, which scale as two powers of the meson masses, as shown in eq. (2.58).
The sources r_μ and l_μ scale as $\mathcal{O}(q^1)$ because of eq. (2.45), so $f_{\mu\nu}^{L/R}$ is $\mathcal{O}(q^2)$ and consequently $f_{\mu\nu}^{\pm}$ as well.

The baryon field B counts as $\mathcal{O}(q^0)$. Unlike the other building blocks, the derivative $D_\mu B$ of the baryon field counts as $\mathcal{O}(q^0)$ as well, because of the large baryon mass. However, subtracting the mass results in a small quantity $(i\not{D} - M_0)B \sim \mathcal{O}(q^1)$.

The chiral orders of all relevant building blocks, together with that of baryon bilinears, are summarized in table 2.1.

2.4 MESONIC LAGRANGIAN

Using the building blocks, we can construct the chiral Lagrangian to arbitrary orders. The chiral orders of the mesonic Lagrangian are always even, because quark masses come as powers of q^2 ($\chi_\pm \sim \mathcal{O}(q^2)$), whereas derivatives ($\mathcal{O}(q^1)$) have to be contracted to form Lorentz scalars. At lowest order $\mathcal{O}(p^2)$, it reads

$$\mathcal{L}_2 = \frac{f_0^2}{4}\operatorname{tr}(u_\mu u^\mu + \chi_+) \tag{2.52}$$

$$= \frac{f_0^2}{4}\operatorname{tr}\Big(D_\mu U D^\mu U^\dagger\Big) + \frac{f_0^2}{4}\operatorname{tr}\Big(\chi U^\dagger + U\chi^\dagger\Big)\,. \tag{2.53}$$

It contains two low-energy constants: f_0 and B_0 (hidden in χ).

One can identify f_0 with the meson decay constant by applying Noether's theorem to the ungauged Lagrangian in the chiral limit, $\mathcal{L} = \frac{f_0^2}{4}\operatorname{tr}\big(\partial_\mu U \partial^\mu U^\dagger\big)$, and obtaining the (conserved) left and right handed currents

$$J_L^{\mu,a} = i\frac{f_0^2}{4}\operatorname{tr}\Big(\lambda_a \partial^\mu U^\dagger U\Big)\,, \tag{2.54}$$

$$J_R^{\mu,a} = -i\frac{f_0^2}{4}\operatorname{tr}\Big(\lambda_a U \partial^\mu U^\dagger\Big)\,. \tag{2.55}$$

Then the single-meson decay is completely determined by the axial-vector current transition matrix element, which is proportial to f_0 via

$$\big\langle 0\big|A^{\mu,a}(x)\big|\phi^b(p)\big\rangle = ip^\mu f_0 e^{-ip\cdot x}\delta^{ab}\,, \tag{2.56}$$

One can show that B_0 is related to the chiral quark condensate via

$$3F_0^2 B_0 = -\langle 0|\,\bar{q}q\,|0\rangle\,. \tag{2.57}$$

Looking at the mass-terms in eq. (2.53) (i.e. those quadratic in the meson fields) for $s + ip = \mathrm{diag}(m_u, m_d, m_s)$, one finds in the isospin limit ($m_u = m_d = m$):

$$M_\pi^2 = 2B_0 m\,, \tag{2.58}$$

$$M_K^2 = B_0(m + m_s)\,, \tag{2.59}$$

$$M_\eta^2 = \frac{2}{3}B_0(m + 2m_s)\,. \tag{2.60}$$

Since only two independent parameters $B_0 m$ and $B_0 m_s$ are involved, the masses satisfy the famous Gell-Mann-Okubo relation

$$4M_K^2 = 3M_\eta^2 + M_\pi^2\,, \tag{2.61}$$

which is accurate at the few percent level.

2.5 MESON-BARYON LAGRANGIAN

At lowest order, $\mathcal{O}(q)$, the Lagrangian was first constructed in Ref. [87] and it reads

$$\mathcal{L}_{MB}^{(1)} = \mathrm{tr}\big(\bar{B}(i\not{D} - M_0)B\big) - \frac{D}{2}\,\mathrm{tr}\big(\bar{B}\gamma^\mu\gamma_5\{u_\mu, B\}\big) - \frac{F}{2}\,\mathrm{tr}\big(\bar{B}\gamma^\mu\gamma_5\,[u_\mu, B]\big)\,, \tag{2.62}$$

with the baryon octet mass M_0 in the chiral limit and the axial vector coupling constants D and F, which are obtained from semi-leptonic decays $B \to B' + \ell + \bar{\nu}_\ell$. At tree level, they have the approximate values $D \approx 0.8$ and $F \approx 0.5$ [88].
For later purposes it is useful to rewrite this Lagrangian in the particle basis:

$$\mathcal{L}_{BB\phi} = \sum_{i,j,k} \frac{1}{2f_0} N_{B_i B_j \phi_k} (\bar{B}_i \gamma^\mu \gamma_5 B_j)(\partial_\mu \phi_k)\,, \tag{2.63}$$

with the coupling constants $N_{B_i B_j \phi_k}$ between an incoming baryon B_i, outgoing baryon B_j, and a meson ϕ_k.

The $\mathcal{O}(q^2)$ contribution was originally developed in Ref. [89] and reduced to its minimal form in Ref. [90]. For our purpose, the relevant terms - given in particle basis - are

$$\begin{aligned}
\mathcal{L} = &- \sum_{c^f = b_D, b_F, b_0} \frac{c^f}{4f_0^2} \sum_{i,j,k,l=1}^{8} N^f_{\phi_{k_j}^{\ i}\phi_l} (\bar{B}_i B_j)\phi_k \phi_l \\
&+ \sum_{c^f = b_1, b_2, b_3, b_4} \frac{c^f}{f_0^2} \sum_{i,j,k,l=1}^{8} N^f_{\phi_{k_j}^{\ i}\phi_l} (\bar{B}_i B_j)\partial_\mu\phi_k \partial^\mu \phi_l \\
&+ \sum_{c^f = d_1, d_2, d_3} \frac{ic^f}{f_0^2} \sum_{i,j,k,l=1}^{8} N^f_{\phi_{k_j}^{\ i}\phi_l} (\bar{B}_i \sigma_{\mu\nu} B_j)\partial^\mu\phi_k \partial^\nu \phi_l\,,
\end{aligned} \tag{2.64}$$

with the coupling constants $N^f_{\phi_{k_j}^{\ i}\phi_l}$ between two baryons and two mesons. Note that the first three terms proportional to b_D, b_F, b_0 involve the quark masses m and m_s.

2.6 BARYON-BARYON INTERACTION

The SU(3) contact Lagrangian has been constructed in Ref. [91] at leading order $\mathcal{O}(q^0)$ and was extended to order $\mathcal{O}(q^2)$ in Ref. [92]. We summarize only those results which are of interest for the present work. The resulting potential takes the form of a linear combination of the following spin- and momentum- dependent operators:

$$\begin{aligned}
&P_1 = 1, && P_2 = \vec{\sigma}_1 \cdot \vec{\sigma}_2\,,\\
&P_3 = (\vec{\sigma}_1 \cdot \vec{q})\,(\vec{\sigma}_2 \cdot \vec{q}) - \frac{1}{3}\vec{\sigma}_1 \cdot \vec{\sigma}_2\ \vec{q}^{\,2}, && P_4 = \frac{i}{2}(\vec{\sigma}_1 + \vec{\sigma}_2) \cdot \vec{n}\,,\\
&P_5 = (\vec{\sigma}_1 \cdot \vec{n})\,(\vec{\sigma}_2 \cdot \vec{n})\,, && P_6 = \frac{i}{2}(\vec{\sigma}_1 - \vec{\sigma}_2) \cdot \vec{n}\,,\\
&P_7 = (\vec{\sigma}_1 \cdot \vec{k})(\vec{\sigma}_2 \cdot \vec{q}) + (\vec{\sigma}_1 \cdot \vec{q})(\vec{\sigma}_2 \cdot \vec{k})\,, && P_8 = (\vec{\sigma}_1 \cdot \vec{k})(\vec{\sigma}_2 \cdot \vec{q}) - (\vec{\sigma}_1 \cdot \vec{q})(\vec{\sigma}_2 \cdot \vec{k})\,,
\end{aligned} \tag{2.65}$$

with $\vec{q} = \vec{p}_f - \vec{p}_i$, $\vec{k} = (\vec{p}_f + \vec{p}_i)/2$ and $\vec{n} = \vec{k} \times \vec{q}$, where $\vec{p}_i$ and $\vec{p}_f$ are initial and final momenta. For all operators the decomposition to partial waves is given in appendix B of [93].

Each of the two interacting baryons corresponds to an octet representation **8** of SU(3). Their tensor product decomposes into irreducible representations as $\mathbf{8} \otimes \mathbf{8} = \mathbf{27}_s \oplus \mathbf{10^*}_a \oplus \mathbf{10}_a \oplus \mathbf{8}_a \oplus \mathbf{8}_s \oplus \mathbf{1}_s$, where s and a refer to the symmetry and antisymmetry with respect to particle exchange, respectively. Since SU(3)-invariant interactions do not mix representations, we can classify the interactions by the representation of the two-particle state and redefine the LECs accordingly.

The total two-baryon wave-function needs to be antisymmetric, so an even/odd flavor representation needs to combine with an odd/even partial wave, respectively: $\mathbf{27}_s$, $\mathbf{8}_s$, and $\mathbf{1}_s$ combine with ${}^1S_0$, ${}^3P_0$, ${}^3P_1$, and ${}^3P_2$, providing $3 \cdot 5 = 15$ constants. $\mathbf{10^*}_a$, $\mathbf{10}_a$, and $\mathbf{8}_a$ combine with ${}^3S_1$, ${}^1P_1$, ${}^3D_1$, and ${}^3D_1 \leftrightarrow {}^3S_1$, yielding $3 \cdot 4 = 12$ constants. One more LEC c^{8as} characterizes the singlet-triplet transition ${}^1P_1 \leftrightarrow {}^3P_1$ that belongs to the transition between $\mathbf{8}_a$ and $\mathbf{8}_s$. Moreover, there are 12 LECs $c_\chi^{1,\dots,12}$ parametrizing SU(3) breaking. An example of the contact potential reads

$$\left\langle NN, {}^1S_0 \right| V \left| NN, {}^1S_0 \right\rangle = \tilde{c}_{{}^1S_0}^{27} + c_{{}^1S_0}^{27}(p_i^2 + p_f^2) + \frac{1}{2}c_\chi^1(m_K^2 - m_\pi^2)\,, \tag{2.66}$$

with a complete list given in Table 10 of Ref. [92].

The meson-exchange contributions are obtained from the meson-baryon Lagrangian (2.62) and the corresponding one-meson-exchange potential reads

$$V_{B_1B_2 \to B_3B_4}^{OBE} = -f_{B_1B_3\phi} f_{B_2B_4\phi} \cdot \frac{(\vec{\sigma}_1 \cdot \vec{q})\,(\vec{\sigma}_2 \cdot \vec{q})}{\vec{q}^{\,2} + m_\phi^2} \tag{2.67}$$

with the baryon-baryon-meson coupling constants $f_{B_iB_j\phi}$, the momentum transfer $\vec{q}$ and mass m_ϕ of the exchanged pseudoscalar meson.

Two-meson exchanges are calculated from one-loop diagrams, namely the planar box, crossed box, triangle, and football diagrams. Detailed expressions are given in appendix A of Ref. [92].

After partial wave projection of the potential, a coupled-channel Lippmann-Schwinger equation is solved for the T-matrix:

$$T^{\rho''\rho',J}_{\nu''\nu'}(k'',k';\sqrt{s}) \\ = V^{\rho''\rho',J}_{\nu''\nu'}(k'',k') + \sum_{\rho,\nu}\int_0^\infty \frac{dk\ k^2}{(2\pi)^3} V^{\rho''\rho,J}_{\nu''\nu}(k'',k)\frac{2\mu_\nu}{k_\nu^2 - k^2 + i\epsilon} T^{\rho\rho',J}_{\nu\nu'}(k,k';\sqrt{s})\,, \tag{2.68}$$

where ν denotes the two-baryon channel, ρ the partial wave, and J the total angular momentum. $\sqrt{s}$ is the center-of-mass energy, k_ν the center-of-mass momentum, and μ_ν the reduced baryon mass in channel ν.

Note that there are two different fitting procedures to the experimental data points [48–50, 94, 95], both which impose SU(3) flavour symmetry to reduce the number of LECs, which in the present notation corresponds to setting $c^i_\chi = 0$.
The first fit, NLO13 [51], utilizes SU(3) symmetry by fitting the P-wave LECs to NN data. The number of remaining P-wave LECs that need to fitted to YN data thus gets reduced from 10 to 6, while all of the 13 S-wave LECs are fitted to YN data.
The second fit, NLO19, extends this idea and uses NN data for fitting S-wave LECs, further reducing the number of contact terms that need to be fitted to YN data from 13 to 10 [96].
For an extensive comparison between these potentials, see [96].

3

3-BODY FORCES

We start by recapitulating the construction of the leading three-body interaction including the exchange of one or two octet mesons, as given in [52]. Then we illustrate the process of decuplet saturation and show how density-dependent 2BFs are obtained from 3BFs, following Ref. [64]. Finally, we extend the calculations of [64] to density-dependent ΛN-ΣN and ΣN-ΣN 2BFs in isospin-asymmetric nuclear matter.

3.1 LEADING THREE-BARYON LAGRANGIAN

The leading three-body contact Lagrangian has been derived in [52] and consists of 18 terms and associated LECs. In the particle basis, it reads

$$\begin{aligned}\mathcal{L}^{\ BBB}_{\ BBB} = \sum_{i,j,k,l,m,n=1}^{8} & \tilde{N}^{1}_{\substack{lmn\\ijk}}(\bar{B}_l B_i)(\bar{B}_m B_j)(\bar{B}_n B_k) \\ & + \tilde{N}^{2}_{\substack{lmn\\ijk}}(\bar{B}_l \sigma_a B_i)(\bar{B}_m \sigma_a B_j)(\bar{B}_n B_k) \\ & + \tilde{N}^{3}_{\substack{lmn\\ijk}}(\bar{B}_l B_i)(\bar{B}_m \sigma_a B_j)(\bar{B}_n \sigma_a B_k) \\ & + \tilde{N}^{4}_{\substack{lmn\\ijk}}(\bar{B}_l B_i)(\bar{B}_m \sigma_a B_j)(\bar{B}_n \sigma_a B_k) \\ & + \tilde{N}^{5}_{\substack{lmn\\ijk}} i\epsilon_{abc}(\bar{B}_l \sigma_a B_i)(\bar{B}_m \sigma_b B_j)(\bar{B}_n \sigma_c B_k)\,. \end{aligned} \tag{3.1}$$

The corresponding fully antisymmetrized potential for $B_1B_2B_3 \to B_4B_5B_6$ boils down to the form

$$V = -\left[N^{1}_{\substack{456\\123}} + N^{2}_{\substack{456\\123}}\vec{\sigma}_A\cdot\vec{\sigma}_B + N^{3}_{\substack{456\\123}}\vec{\sigma}_A\cdot\vec{\sigma}_C + N^{4}_{\substack{456\\123}}\vec{\sigma}_B\cdot\vec{\sigma}_C + N^{5}_{\substack{456\\123}} i\vec{\sigma}_A\cdot(\vec{\sigma}_B\times\vec{\sigma}_C)\right], \tag{3.2}$$

with $N^{i}_{\substack{456\\123}}$ obtained from $\tilde{N}^{f}_{\substack{lmn\\ijk}}$ by fully antisymmetrizing it. $\tilde{N}^{f}_{\substack{lmn\\ijk}}$ is a combination of the 18 LECs and SU(3) coefficients obtained by evaluating the flavor traces in the original Lagrangian in [52]. The indices A, B, C label the spin space attached to each baryon line.

The one-meson exchange contributions (c.f. figure 3.1b) require a two-baryon-one-meson contact vertex from the meson-baryon Lagrangian (2.63) and a four-baryon-one-meson vertex given by the respective Lagrangian in [52], which in particle basis reads

$$\begin{aligned}\mathcal{L}^{\ BB}_{\ BB\phi} = & \sum_{f=1}^{10}\frac{D_f}{f_0}\sum_{i,j,k,l,m=1}^{8} N^{f}_{\substack{ik\\jl\,\phi_m}}(\bar{B}_i B_j)(\bar{B}_k\vec{\sigma}B_l)\cdot\vec{\nabla}\phi_m \\ & + \sum_{f=11}^{14}\frac{D_f}{f_0}\sum_{i,j,k,l,m=1}^{8} N^{f}_{\substack{ik\\jl\,\phi_m}}\, i\left[(\bar{B}_i\vec{\sigma}B_j)\times(\bar{B}_k\vec{\sigma}B_l)\right]\cdot\vec{\nabla}\phi_m\,. \end{aligned} \tag{3.3}$$

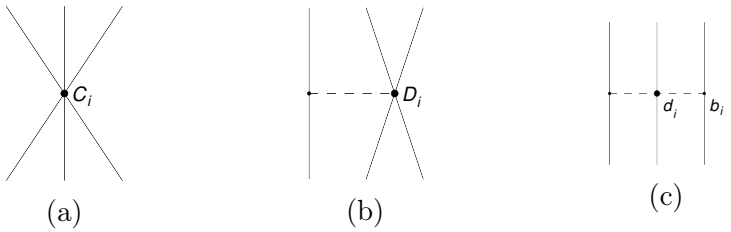

Figure 3.1: Leading contributions to the (irreducible) three-baryon interaction: (a) contact term, (b) one-meson exchange, and (c) two-meson exchange. Small and large dots refer to vertex dimensions of 0 and 1, respectively.

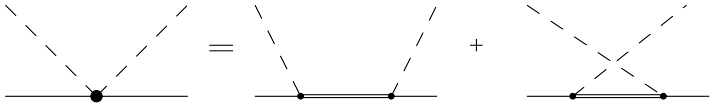

Figure 3.2: Decuplet saturation of the two-meson contact vertex. Octet baryons are represented by a single line, decuplet baryons by a double line.

In the end, the three-body potential takes the form

$$V = \frac{1}{2f_0^2}\frac{\vec{\sigma}_A\cdot\vec{q}}{\vec{q}^2+m_\phi^2}\left[N_1\vec{\sigma}_B\cdot\vec{q}+N_2\vec{\sigma}_C\cdot\vec{q}+N_3 i(\vec{\sigma}_B\times\vec{\sigma}_C)\cdot\vec{q}\right], \tag{3.4}$$

with $N_{1,2,3}$ being combinations of two-baryon-one-meson and four-baryon-one-meson LECs $N_{B_iB_j\phi_k}$ and $N_{\substack{ik\\jl}\phi_m}$ as defined in eqs. (2.63) and (3.3).

The two-meson exchange also requires the meson-baryon Lagrangian (2.62) both at order $\mathcal{O}(q)$ and $\mathcal{O}(q^2)$, given in eqs. (2.63) and (2.64), respectively. The corresponding three-body potential reads

$$V = \frac{-1}{4f_0^4}\frac{\vec{\sigma}_A\cdot\vec{q}_1\quad\vec{\sigma}_C\cdot\vec{q}_2}{(\vec{q}_1^{\,2}+m_{\phi_1}^2)(\vec{q}_2^{\,2}+m_{\phi_2}^2)}\left[N_1'+N_2'\,\vec{q}_1\cdot\vec{q}_2+N_3'\,i(\vec{q}_1\times\vec{q}_2)\cdot\vec{\sigma}_B\right] \tag{3.5}$$

with $N'_{1,2,3}$ being combinations of two two-baryon-one-meson and one two-baryon-two-meson LECs $N_{B_iB_j\phi_k}$ and $N^{f}_{\phi_k\,\substack{i\\j}\,\phi_l}$ as defined in eqs. (2.63) and (2.64). The masses and momenta of the two exchanged particles are denoted by $m_{\phi_{1,2}}$ and $\vec{q}_{1,2}$, respectively.

3.2 ESTIMATION OF LECS THROUGH DECUPLET BARYON SATURATION

The problem of having very little experimental data is even more severe in the three-baryon sector. The large number of LECs in the Lagrangians (2.63), (2.64), and (3.3) makes it unfeasible to fit all to observables. In that situation estimates via decuplet baryon saturation can be obtained as sketched in figures 3.2, 3.3, 3.4. For this purpose, one needs two new Lagrangians: one for the transition between octect and decuplet baryons involving a meson and one for the contact vertices between three octet and one decuplet baryon, both given in Ref. [52]. The important feature is that only three LECs are introduced by these Lagrangians. One, denoted C, for the mesonic octet-decuplet transition (c.f. figure 3.5a) and two, H_1 and H_2, for the contact vertex (c.f. figure 3.5b). While $H_{1,2}$ are a priori unknown, the value of C can be inferred from the $\Delta\to\pi N$ decay and large-N_C considerations as $C=\frac{3}{4}g_A\approx 0.95$.

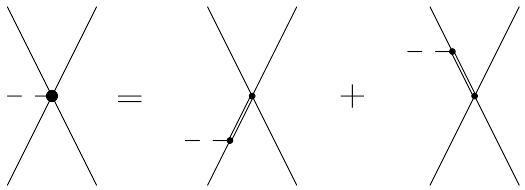

Figure 3.3: Decuplet saturation of the four-baryon-one-meson vertex.

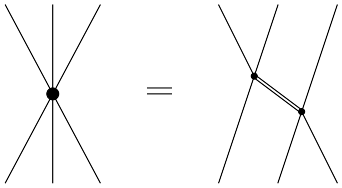

Figure 3.4: Decuplet saturation of the six-baryon contact vertex.

With decuplet saturation, the parameters C_i, D_i, b_i, and d_i can be expressed through C, $H_{1,2}$, and the average decuplet-octet baryon mass-splitting $\Delta \approx 270$ MeV in the form

$$b_i, d_i \propto \frac{C^2}{\Delta}\,, \qquad C_i = \frac{1}{\Delta}(\alpha H_1 + \beta H_2)\,, \tag{3.6}$$

$$D_i = \frac{C}{\Delta}(\alpha H_1^2 + \beta H_1 H_2 + \gamma H_2^2)\,. \tag{3.7}$$

Because of the comparably small value of the mass-splitting $\Delta \approx 270$ MeV in relation to the chiral breakdown scale Λ_χ, the LECs in the decuplet saturation will become "unnaturally" large. Therefore, these NNLO contributions are promoted to NLO.

3.3 REDUCTION OF THREE-BODY FORCES TO DENSITY DEPENDENT TWO-BODY POTENTIALS

In this section, we prepare the three-baryon forces for usage in two-body Brueckner calculations, closely following Ref. [64]. This is done by integrating one nucleon over the Fermi sea of the medium, effectively converting three-body interactions into density-dependent two-body potentials. Diagrammatically, this is represented by closing one incoming with one outgoing baryon line and indicating the Fermi sea contribution by a double-line on the loop. This decoration symbolizes the *medium insertion* $\theta\big(k_F^3 - \big|\vec{k}\big|\big)$ of the in-medium baryon propagator. Formally, the two-body potential is calculated as

$$V_{12} = \sum_B tr_{\sigma_3} \int_{\left|\vec{k}\right| \leq k_F^B} \frac{d^3k}{(2\pi)^3} V_{123}\,, \tag{3.8}$$

with a sum over all species B (protons and neutrons) in the Fermi sea, a spin trace over the third particle, and a momentum integral over the filled Fermi sea.

Depending on the number of exchanged pions and the closing of nucleon lines, there are 6 different topologies (c.f. figure 3.6).

Three arise from two-pion-exchange: Topology 1 is obtained by closing the second nucleon line to itself, effectively introducing a modification of the pion propagator. To get topology 2, the second and third nucleon line are joined in order (a) or vice versa (b). The third topology is realized by joining the first and third nucleon lines.

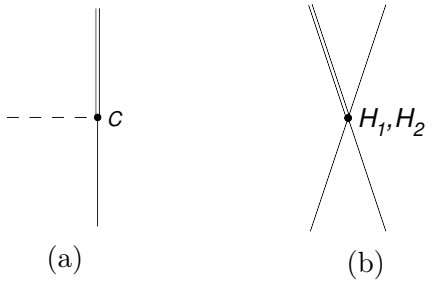

Figure 3.5: Two new vertices associated with the decuplet saturation procedure. The meson-octet-decuplet vertex in (a) introduces the LEC C, while the three-octet-one-decuplet contact-vertex in (b) introduces H_1 and H_2.

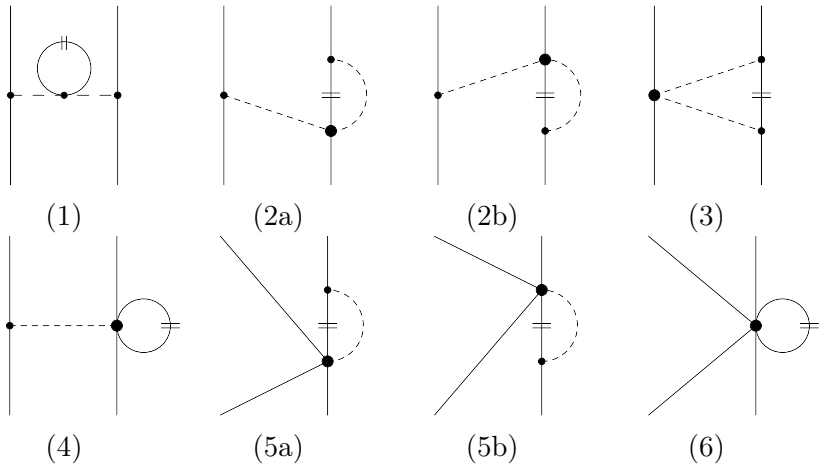

Figure 3.6: Different topologies for the density-dependent two-body potential arising from the closing of nucleon lines.

Two topologies stem from one-meson-exchange: Diagram 4 corresponds to the closing of a nucleon line of the contact vertex and constitutes to a density-dependent modification of the one-pion exchange. In topology 5 one nucleon line is joined to a nucleon on the other side of the contact vertex.

The last topology 6 originates from the six-baryon contact interaction by closing two nucleon lines. It modifies the two-baryon contact potential.

In the same way, results for density-dependent NN potentials in symmetric nuclear matter have been obtained in Ref. [63], whereas the extension to asymmetric nuclear matter was derived in Ref. [62]. For the LECs related to the three-nucleon force, we take the values $c_D = -0.2, c_E = -0.205$ as given in Ref. [97]. Furthermore, we employ the off-shell extension $p^2 \to \frac{1}{2}(p'^2 + p^2)$, with p (p') the initial (final) center of mass momentum of baryons, as suggested in Ref. [63].

In Ref. [64], the medium corrections have been calculated from contact and pion-exchange contributions [1] to the ΛN-ΛN interaction in general asymmetric nuclear matter and for ΛN-ΣN and ΣN-ΣN interactions in symmetric nuclear matter. A special feature of these results

1 The exchange of heavier mesons, kaons or η, contributes at shorter distances. Therefore, their contribution is understood to be parameterized by the contact terms.

is that for the ΛN-ΛN interaction the LECs H_1 and H_2 only contribute in the combination $H' \coloneqq H_1 + 3H_2$, thus reducing the variability of this interaction. A similar feature does not apply for ΛN-ΣN and ΣN-ΣN.

In this work, we extend the aforementioned ΛN-ΣN and ΣN-ΣN calculations to asymmetric nuclear matter. The explicit results obtained in the particle basis are given in appendix B. In the case of symmetric nuclear matter, they coincide with the results given in Ref. [64].

Since the LECs H_1 and H_2 are not empirically constrained, they serve as a good tool for tuning the results of the Brueckner calculations. We will investigate this in further detail in section 5.3.5.

Note that we only include three-body forces that involve a single hyperon, while interactions with two or three hyperons are neglected. Since we are investigating the onset of Λ formation, there is no Λ (or Σ) Fermi sea that would contribute to the medium insertion of a YYY three-body interaction. The same applies to YYN forces.

4

BRUECKNER THEORY

In this chapter, we will introduce Brueckner theory and lay the groundwork for our calculations of the hyperon single-particle potentials in nuclear matter. This chapter follows Refs. [98, 99].

4.1 FOUNDATION

Brueckner theory is a non-relativistic many-body approach that has been mostly applied to nuclear matter. It is based on the hole-line expansion of Goldstone, which is a linked-cluster perturbation series. It works for any number of particles, with the only requirement that the ground state is not degenerate.
Nuclear matter is a hypothetical, infinitely large system of equal parts protons and neutrons of uniform density in which the Coulomb force is switched off. The system possesses a translational invariance, which provides a great simplification to the calculation, since the wave functions are plane waves. Originally formulated to calculate the energy per particle E/A at fixed density ρ, Brueckner theory also allows to calculate more detailed properties like the single-particle energies of the constituents.

We start with a Hamiltonian of the system that consists of the kinetic energies of all A particles and the two-body interactions between all pairs of particles:

$$H = T + V = \sum_{i=1}^{A} T_i + \sum_{i<j}^{A} v_{ij} \,. \tag{4.1}$$

However, it is not yet possible to perform a perturbative expansion in V, because v_{ij} contains a very strong short-range repulsion. Therefore, one defines a new unperturbed Hamiltonian H_0 and its perturbation H_1 as

$$H = H_0 + H_1 \,, \qquad \text{with} \qquad H_0 = \sum_{i=1}^{A} (T_i + U_i), \quad H_1 = \sum_{i<j}^{A} v_{ij} - \sum_{i=1}^{A} U_i \tag{4.2}$$

where the single-particle potential U_i of particle i is chosen in such a way that H_1 is reasonably "small". Due to its auxiliary nature, the total Hamiltonian does not depend on U_i, so the results of the calculations should be independent of it. However, certain choices of U_i will make the expansion series converge faster than others. This will be specified in detail later on.
The unperturbed ground state $|\Phi_0\rangle$ and the exact ground state $|\Psi\rangle$ of the many-body system obey

$$H_0 \,|\Phi_0\rangle = E_0 \,|\Phi_0\rangle \qquad \text{and} \tag{4.3}$$

$$H \,|\Psi\rangle = E \,|\Psi\rangle \,. \tag{4.4}$$

With this, the Goldstone expansion for the energy shift $\Delta E = E - E_0$ reads [100]

$$\Delta E = \sum_{\substack{n=0 \\ L}}^{\infty} \langle \Phi_0 | \, H_1 \left(\frac{1}{E_0 - H_0} H_1 \right)^n |\Phi_0\rangle \tag{4.5}$$

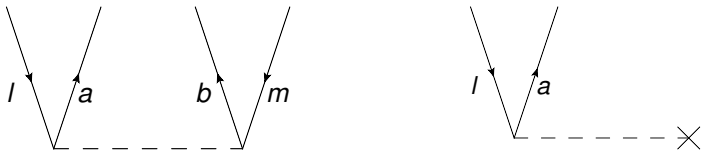

Figure 4.1: Diagrammatic representation of V (left) and U_i (right) as a dashed line, acting on $|\Phi_0\rangle$. Upward and downward lines denote particles and holes, respectively. In second quantization, the interactions read $\langle ab|\, v_{ij}\, |lm\rangle\, a_a^\dagger a_b^\dagger a_m a_l$ and $\langle a|\, U_i\, |l\rangle\, a_a^\dagger a_l$, so that creation operators $a^\dagger$ are identified with outgoing lines and annihilation operators a with incoming lines.

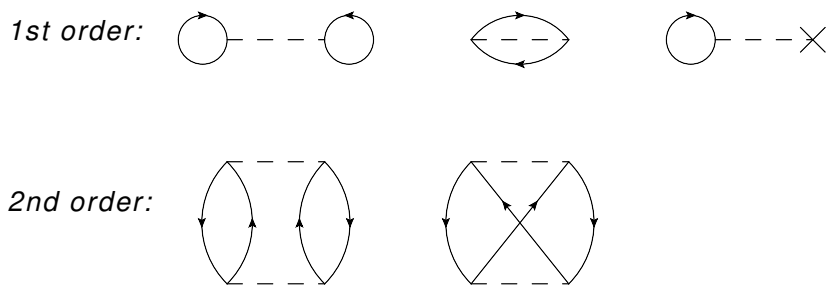

Figure 4.2: Diagrammatic representation of the first two orders of the Goldstone expansion. The diagrams are read from bottom to top, with the state $|\Phi\rangle_0$, corresponding to no particles or holes, at both ends. Second order diagrams that involve only a single particle- or hole-line do not contribute because of momentum conservation.

where $\sum_L$ indicates that only connected diagrams are to be included in the sum.[1] The action of the two constituents U_i and V of H_1 on a state can be represented in diagrams, as shown in figures 4.1. The first two orders of the Goldstone expansion (4.5) are shown in figure 4.2. Note that for every intermediate state, the energy denominator $E_0 - H_0$ is calculated as the sum of hole energies minus the sum of particle energies.
To first order, the total energy reads

$$E = \sum_{n\leq A} \langle n|\, T\, |n\rangle + \frac{1}{2} \sum_{m,n\leq A} \left(\langle mn|\, v\, |mn\rangle - \langle mn|\, v\, |nm\rangle\right). \tag{4.6}$$

One cannot use this expansion for nuclear matter calculations, because of the strong short-range repulsion in V, which would make the series divergent. Hence, one has to replace it with a better-behaved quantity, namely Brueckner's reaction matrix G. It is obtained by adding up an infinite series of ladder-diagrams, effectively summing V up to all orders (see fig. 4.3).
While performing the ladder resummation, the energy denominator (hole energies minus particle energies) changes with each interaction V. However, there are certain terms that all energy denominators have in common and do not change throughout the resummation. In the example of fig. 4.3, the energies of the two holes lines on the outside of each diagram contribute to every denominator. Such terms are collected in the so-called starting energy ω. The energy denominator e can therefore be written as the starting energy minus the energies of the two intermediate particles p and q:

$$e = \omega - E_p - E_q\,. \tag{4.7}$$

1 Goldstone's achievement was to show that the disconnected graphs arising in the general perturbation series cancel in every order

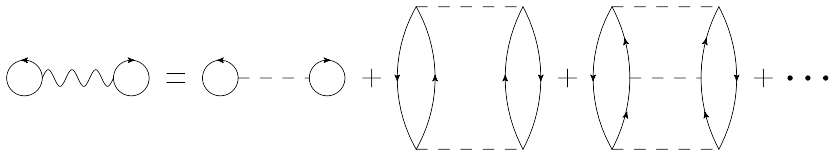

Figure 4.3: One example of the ladder summation $G = V + V(Q/e)G$. G is represented as wiggly line. This summation may also occur as part of larger diagrams.

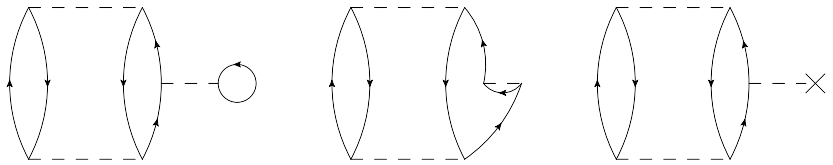

Figure 4.4: Three diagrams (bubble interaction, exchange bubble, and U interaction, respectively) whose contributions cancel each other by choosing $U = U_{HF}$. Similar cancellations occur if the interactions happen on a hole line. Furthermore, these cancellations are preserved under replacement of the bare interactions V with the reaction matrix G.

In the end, the summation of ladder diagrams reads

$$G(\omega) = V + V\,\frac{Q}{e}\,V + V\,\frac{Q}{e}\,V\,\frac{Q}{e}\,V + ... = V + V\,\frac{Q}{e}\,G(\omega) \tag{4.8}$$

where the Pauli blocking operator Q ensures that intermediate particle states are from above the occupied Fermi sea:

$$Q\,|pq\rangle = \begin{cases} |pq\rangle & k_p, k_q > k_F\,, \\ 0 & \text{else}\,. \end{cases} \tag{4.9}$$

Although this series looks divergent to any given order (because of the strong repulsion in V), the infinite ladder summation for G is well-behaved. This divergence behavior makes a full solution (as opposed to an iterative one) of eq. (4.8) mandatory, a circumstance that will be discussed later on.

As mentioned before, the auxiliary nature of U_i allows us to choose it in such a way that it is most beneficial for the convergence behavior of the series. The most famous choice is the Hartree-Fock potential U_{HF}:

$$\langle p|\,U_{HF}\,|q\rangle = \sum_{n\leq A} \left(\langle pn|\,V\,|qn\rangle - \langle pn|\,V\,|nq\rangle\right), \tag{4.10}$$

with the idea of cancelling a certain subgroup of diagrams, one example of which is given in fig. 4.4. When switching to the Brueckner G-matrix, the single-particle potential becomes

$$U(k_m) = \sum_{n\leq A} \langle mn|\,G(\omega)\,|mn\rangle_A \tag{4.11}$$

where the subscript A denotes antisymmetrization. Returning to the starting energy ω, it can be shown that by choosing it on-shell, this leads to cancellations in higher order diagrams. Bethe, Brandow, and Petschek furthermore have proved that this holds to any order in perturbation

theory [101], so that the on-shell condition can also be used for the G-matrix. We finally arrive at

$$U(k_m) = \sum_{n \leq A} \langle mn| \, G(\omega = E_m + E_n) \, |mn\rangle_A \ . \tag{4.12}$$

4.2 FORMALISM

We employ conventional Brueckner theory in leading order of the hole-line expansion (i.e. two hole-lines), the so-called *Brueckner-Hartree-Fock (BHF)* approximation.
Explicit formulas in the particle basis have been worked out in Ref. [99] and are now recapitulated in this section.

Two incoming baryons B_1 and B_2 have the momenta $\vec{k}_1$ and $\vec{k}_2$ and masses M_1 and M_2, respectively. The total and relative momentum are then given by

$$\vec{K} = \vec{k}_1 + \vec{k}_2, \qquad \vec{k} = \frac{\xi_{12}\vec{k}_1 - \vec{k}_2}{1+\xi_{12}}, \qquad \text{with} \ \ \xi_{12} = \frac{M_2}{M_1} \, . \tag{4.13}$$

The Bethe-Goldstone equation (BGE), realizing the ladder resummation (4.8), is first projected onto partial waves. For a given total angular momentum J, total momentum K and starting energy ω, it reads

$$\begin{aligned} G^{\rho''\rho',J}_{\nu''\nu'}(k'',k';K,\omega) &= V^{\rho''\rho',J}_{\nu''\nu'}(k'',k') \\ &+ \sum_{\rho,\nu} \int_0^\infty \frac{dk \ k^2}{(2\pi)^3} V^{\rho''\rho,J}_{\nu''\nu}(k'',k) \frac{\bar{Q}_\nu(K,k)}{\bar{e}_\nu(K,k;\omega) + i\varepsilon} G^{\rho\rho',J}_{\nu\nu'}(k,k';K,\omega) \end{aligned} \tag{4.14}$$

where $\rho = (SL)$ denotes the partial wave with S the spin and L the orbital angular momentum, while $\nu = (B_iB_j)$ denotes a particle channel. To be more precise, the sets of labels $\{k',\rho',\nu' = (B_1B_2)\}$, $\{k'',\rho'',\nu'' = (B_3B_4)\}$, and $\{k,\rho,\nu = (B_5B_6)\}$ denote the initial, final, and intermediate state, respectively.
In practice, the calculations are conducted up to a maximum total angular momentum $J_{max} = 5$. One should note that the angular dependence of the integral in eq. (4.14) has been removed by replacing Q/e with its angle-averaged counterparts $\bar{Q}/\bar{e}$. This approximation is necessary to make calculations in the partial wave basis feasible at all.
The angle-averaged version of the Pauli-blocking operator is given by

$$\begin{aligned} \bar{Q}_\nu(K,k) &= \frac{1}{2}\int_{-1}^{1} \mathrm{d}\cos\theta \cdot \Theta\Big(\Big|\vec{k}_5\Big| - k_F^{(5)}\Big)\Theta\Big(\Big|\vec{k}_6\Big| - k_F^{(6)}\Big) \\ &= \left[0\left|\frac{[-1|z_5|1] + [-1|z_6|1]}{2}\right|1\right], \end{aligned} \tag{4.15}$$

$$\text{where} \qquad z_5 = \frac{1+\xi_{56}}{2kK}\left(\left(\frac{K}{1+\xi_{56}}\right)^2 + k^2 - \left(k_F^{(5)}\right)^2\right)$$

$$z_6 = \frac{1+1/\xi_{56}}{2kK}\left(\left(\frac{\xi_{56}K}{1+\xi_{56}}\right)^2 + k^2 - \left(k_F^{(6)}\right)^2\right), \tag{4.16}$$

using the convenient notation $[a|b|c] = \max(a, \min(b, c))$.
The energy-denominator reads

$$\bar{e}_\nu(K, k; \omega) = \omega - \frac{K^2}{2M_\nu} - \frac{k^2}{2\mu_\nu} - M_\nu - \mathrm{Re}\, U_{B_5}(\bar{k}_5) - \mathrm{Re}\, U_{B_6}(\bar{k}_6)\,, \tag{4.17}$$

$$\text{with} \qquad M_\nu = M_5 + M_6, \qquad \mu_\nu = \frac{M_5 M_6}{M_5 + M_6}\,, \tag{4.18}$$

where the angle-averaged momenta $\bar{k}_5$ and $\bar{k}_6$ of the intermediate state baryons are calculated from K and k by rearranging eq. (4.13) and replacing $\cos\theta$ with its angle average:

$$\bar{k}_5 = \left(\frac{1}{(1+\xi_{56})^2} K^2 + k^2 + 2\frac{1}{1+\xi_{56}} K k \overline{\cos\theta} \right)^{1/2}, \tag{4.19}$$

$$\bar{k}_6 = \left(\frac{\xi_{56}}{(1+\xi_{56})^2} K^2 + k^2 + 2\frac{\xi_{56}}{1+\xi_{56}} K k \overline{\cos\theta} \right)^{1/2}, \tag{4.20}$$

with

$$\overline{\cos\theta} = \frac{\int_{-1}^{1} \mathrm{d}\cos\theta \cos\theta\, Q(\vec{K}, \vec{k})}{\int_{-1}^{1} \mathrm{d}\cos\theta\, Q(\vec{K}, \vec{k})} = \frac{1}{2}\left([-1|z_5|1] - [-1|z_6|1] \right)\,. \tag{4.21}$$

Note that $\overline{\cos\theta} = 0$ in the case of two nucleons in symmetric nuclear matter, because $z_5 = z_6$. Alternatively one can use the root of the mean squared cosine

$$\sqrt{\overline{\cos^2\theta}} = \sqrt{\frac{\int_{-1}^{1} \mathrm{d}\cos\theta \cos^2\theta\, Q(\vec{K}, \vec{k})}{\int_{-1}^{1} \mathrm{d}\cos\theta\, Q(\vec{K}, \vec{k})}} = \frac{1}{\sqrt{3}} \left[0 \middle| \frac{1}{kK} \left(\frac{K^2}{4} + k^2 - k_F^2 \right) \middle| 1 \right]. \tag{4.22}$$

There are two options for introducing the single-particle potentials (SPPs) to the energy-denominator (4.17): The first one is the so-called *gap choice*, where the SPP is set to zero above the Fermi sea, i.e. $U_B(k > k_F) = 0$. Since this introduces a discontinuity at the Fermi sea, it is also referred to as the *discontinuous choice*. While the gap choice is computationally much simpler[2], it underestimates the nuclear binding energy (see fig. 4.5).
The other one is the so-called *continuous choice*, where the discontinuity is lifted by applying eq. (4.17) to all states. While it provides more accurate results in terms of nuclear binding energies and features some favorable analytical properties [102], it is computationally much more challenging. In this work, the continuous choice will be employed throughout.

The equation for the single-particle potential of baryon B_1 due to the Fermi sea of baryon B_2, based on eq. (4.12), reads

$$\begin{aligned} U_{B_1}^{B_2}(k_1) = &\left(1 + \delta_{B_1 B_2}(-1)^{L+S}\right) \frac{(1+\xi_{12})^3}{2} \\ &\times \sum_{J,\rho} (2J+1) \int_{k_{min}}^{k_{max}} \frac{dk\ k^2}{(2\pi)^3} W(k_1, k) G^{\rho\rho,J}_{(B_1B_2)(B_1B_2)}(k, k; \bar{K}, \omega_{o.s.})\,. \end{aligned} \tag{4.23}$$

The weighting function W includes an angular integral and takes the explicit form

$$W(k_1, k) = \frac{1}{4\pi} \int_{|\vec{k}_2| \le k_F^{(2)}} \mathrm{d}\Omega_k = \frac{1}{2}(1 - [-1|x_0|1])\,, \tag{4.24}$$

2 Only a moderate number points on the momentum grid need to be calculated.

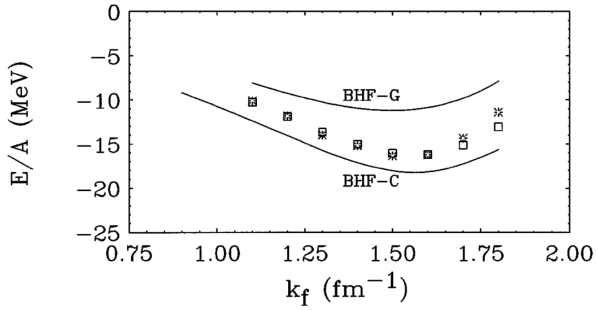

Figure 4.5: Energy per particle E/A of symmetric nuclear matter for different choices of the single-particle potential and perturbation orders. *BHF-G* and *BHF-C* refer to the Brueckner-Hartree-Fock (=two hole-line contributions) with gap and continous choice, respectively. Squares and stars also include (higher order) three hole-line contributions. Figure taken from [103].

with the auxiliary quantity

$$x_0 = \frac{\xi_{12}^2 k_1^2 + (1+\xi_{12})^2 k^2 - (k_F^{(2)})^2}{2\xi_{12}(1+\xi_{12}) k_1 k} \,. \tag{4.25}$$

The integration limits in eq. (4.23) are

$$k_{min} = \max\left(0, \frac{-k_F^{(2)} + \xi_{12} k_1}{1+\xi_{12}}\right), \tag{4.26}$$

$$k_{max} = \frac{k_F^{(2)} + \xi_{12} k_1}{1+\xi_{12}} \,, \tag{4.27}$$

and the on-shell starting energy is

$$\omega_{o.s.} = E_{B_1}(k_1) + E_{B_2}(\bar{k}_2) \,, \tag{4.28}$$

$$\text{where} \qquad E_{B_i}(k_i) = M_i + \frac{k_i^2}{2M_i} + \mathrm{Re}\, U_{B_i}(k_i) \,. \tag{4.29}$$

At this point, further angle-averaged momenta are introduced, namely for the square of the momentum of the second incoming baryon and the square of the total momentum:

$$\bar{k}_2^2(k_1,k) = \frac{\xi_{12}}{1+\xi_{12}} \bar{K}^2(k_1,k) + (1+\xi_{12}) k^2 - \xi_{12} k_1^2 \,, \tag{4.30}$$

$$\bar{K}^2(k_1,k) = (1+\xi_{12})^2 \big(k_1^2 + k^2 - k_1 k (1 + [-1|x_0|1])\big) \,. \tag{4.31}$$

4.3 NUCLEAR MATTER PROPERTIES

The density ρ of baryonic matter is the sum over the densities of each baryon species and it reads

$$\rho = \sum_B \rho_B = \sum_B \frac{\left(k_F^{(B)}\right)^3}{3\pi^2} \,. \tag{4.32}$$

In particular, for isospin-symmetric nuclear matter we have $\rho_n = \rho_p = \rho/2$, whereas pure neutron corresponds to $\rho_n = \rho$, $\rho_p = 0$.

From the (nucleon) single-particle potentials we can calculate several properties of nuclear matter that will be used for comparisons in the following chapter. The energy density of the system is

$$\epsilon = \sum_B \left(\frac{\left(k_F^{(B)}\right)^5}{10\pi^2 M_B} + \frac{1}{2\pi^2} \int_0^{k_F^{(B)}} \mathrm{d}k\, k^2 \,\mathrm{Re}\, U_B(k) \right) , \tag{4.33}$$

with the binding energy per particle

$$\frac{E}{A} = \frac{\epsilon}{\rho} \tag{4.34}$$

and the chemical potential of a baryon species B follows from it as

$$\mu_B = \frac{\partial \epsilon}{\partial \rho_B} . \tag{4.35}$$

quickly following from it. Furthermore, the pressure of a system can be obtained from the Gibbs-Duhem relation $\mathrm{d}E = -p\,\mathrm{d}V$ at $T = 0$:

$$p(\epsilon) = \rho \frac{\partial \epsilon}{\partial \rho} - \epsilon . \tag{4.36}$$

4.4 INPUT POTENTIALS

For the calculation of nuclear matter properties, the bare potential V is given by SU(2) chiral EFT at next-to-next-to-next-to leading order (N3LO)[33]. It is available for different cutoffs (414, 450, and 500 MeV) and we will distinguish between these versions by appending the cutoff in parentheses behind the order, e.g. N3LO(500). Moving over to the strangeness sector $S = -1$, hyperon-nucleon potentials are given by chiral SU(3) EFT at NLO, plus the density-dependent effective two-body potentials obtained from chiral three-baryon forces.

As mentioned in section 2, chiral two-body potentials are fitted to scattering data, which makes them yield similar on-shell predictions for different cutoffs. However, their results in nuclear matter will differ because of their off-shell behavior that becomes relevant when integrating over intermediate states in the BGE. Adopting the same notation as before, different cutoffs of the NLO13 or NLO19 potentials will also be specified when necessary, e.g. NLO13(500).

When including three-body forces in the calculation of U, it is important to note that the procedure of closing nucleon-lines is used both for the transcription of 3BFs to 2BFs in eq. (3.8) and for calculating U from G in eq. (4.23). Since these steps happen independently from each other, some interaction diagrams are over-counted: For NNN [YNN] interactions, the contraction from 3BF to 2BF (figure 4.6a) has 9 [4] possibilities and the subsequent contraction from 2BF to U has 4 [1] possibilities, for a total of 36 [4]. On the other hand, the direct contraction from 3BF to U (figure 4.6b)) only has 18 [2] possibilities. Therefore a statistical factor of $\frac{1}{2}$ needs to be applied to the effective two-body interaction when it is used to compute the single-particle potential.
Analogously, a factor of $\frac{1}{3}$ has to be applied when adding the 3N-forces through density-dependent NN-potentials to calculations of the energy per particle of nuclear matter. In this case, all three nucleon lines get contracted.

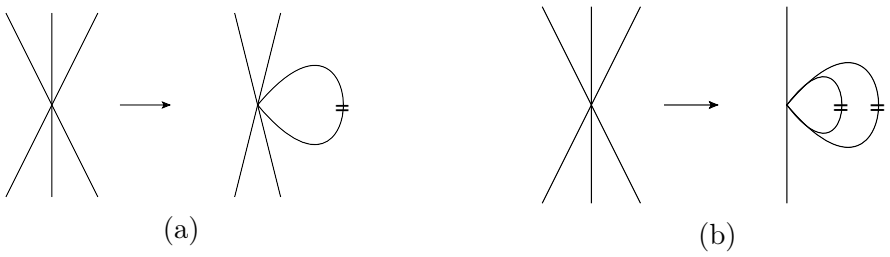

Figure 4.6: Comparison of (a) the single medium-insertion from 3BF to 2BF and (b) the double contraction from 3BF to the single-particle potential.

4.5 NUMERIC APPROACH

The self-consistent eqs. (4.14), (4.23) are solved numerically by alternately iterating both equations until U converges. For this purpose $U(k)$ is interpolated on a uniformly-spaced grid with a momentum spacing of 33.33 MeV. Moreover, the Bethe-Goldstone equation in eq. (4.14) is discretized so that G assumes matrix-form and the integral equation becomes a matrix equation which can be solved by methods of linear algebra [104].

4.5.1 *Treatment of poles in the BGE*

Integrals over poles in the BGE are treated either by manually adding a small imaginary increment $i\varepsilon$ to the numerator (in the nucleonic case) or by invoking the principal value prescription for the real part (in the hyperon case). In the latter case one uses the identity

$$\int_0^\infty dk \frac{N(k)}{D(k)+i\varepsilon} = \int_0^\infty \left(\frac{N(k)}{D(k)} - 2k_0 \frac{N(k_0)}{D'(k_0)} \frac{1}{k^2-k_0^2} \right) - i\pi \frac{N(k_0)}{|D'(k_0)|} \tag{4.37}$$

for a simple pole located at $k = k_0$, i.e. $D(k_0) = 0$, $D'(k_0) \neq 0$.

4.5.2 *Optimization*

There are several ways to improve the runtime of the calculations. First of all, we can use the information about the particle channels that couple with each other (c.f. table 4.1). As NN two-body states do not couple to YN states, the calculation can be split up by first computing U_n and U_p and employing them in the calculation of U_Λ and U_Σ.
In case of pure neutron matter, the calculations of hyperon single-particle potentials can be split up even further by the charge. As $\Sigma^- n$ does not couple to any other YN state, U_{Σ^-} does not depend on U_Λ, U_{Σ^+}, or U_{Σ^0} and thus can be computed on its own. Next, U_Λ and U_{Σ^0} can be computed at the same time regardless of U_{Σ^+}, because Λn and $\Sigma^0 n$ do not couple to $\Sigma^+ N$. At this point, the calculation of U_{Σ^+} may be omitted since the focus of this work lies on U_Λ.
In symmetric nuclear matter, isospin symmetry implies that all three Σ single-particle potentials are equal, i.e. $U_{\Sigma^-} = U_{\Sigma^0} = U_{\Sigma^+}$, so that only one of them needs to be calculated, which is chosen to be U_{Σ^0}.

S	Q	coupled states
	0	nn
0	1	np
	2	pp
	-1	$\Sigma^- n$
	0	$\Lambda n, \Sigma^0 n, \Sigma^- p$
0	1	$\Lambda p, \Sigma^+ n, \Sigma^0 p$
	2	$\Sigma^+ p$

Table 4.1: Coupled particle channels, sorted by strangeness S and charge Q

4.5.3 *Solving the BGE*

Throughout this work, the Bethe-Goldstone equation will be solved via discretization to a matrix equation, thus summing up all orders of V and Q/e. The disadvantage is that no libraries exist to solve this kind of problem, making a custom-tailored solution prone to coding bugs and numerical instabilities.

Another approach that is worth mentioning is to solve the BGE iteratively up to a certain order:

$$\begin{aligned} G &= G^{(0)} + G^{(1)} + G^{(2)} + \dots , \\ G^{(0)} &= V , \\ G^{(1)} &= V \frac{Q}{e} V , \\ G^{(2)} &= V \frac{Q}{e} V \frac{Q}{e} V , \end{aligned} \tag{4.38}$$

where the integrations are performed with the help of Monte-Carlo methods. The advantage of this method is the availability of a robust library [105], which makes the programming relatively easy. While this approach has yielded very similar results to the full solution in the nucleonic sector, it has failed for hyperons due to the large size of some YN potentials. In particular, the ${}^3S_1$ partial wave is so large that the above series becomes divergent.

4.5.4 *Numerical instabilities*

For large densities $\rho \gtrsim 3\rho_0$, especially in pure neutron matter, the convergence of U_Λ is getting more and more unreliable. One reason for U_Λ to overshoot its fixed point are the strong input potentials. To allow for more stable convergence, one can artificially slow down the process by introducing a brake parameter N: Let $U_\Lambda^{(i)}$ denote the single-particle potential after iteration step i, starting with $U_\Lambda^{(0)} \equiv 0$. Instead of using $U_\Lambda^{(i-1)}$ as input when calculating $U_\Lambda^{(i)}$, one takes the weighted average

$$\frac{U_\Lambda^{(i-1)} + N \cdot U_\Lambda^{(i-2)}}{1+N} . \tag{4.39}$$

Another reason for the unreliability of the outcome are numerical artifacts that produce sudden sign changes or spikes in the order of GeV to the potential. Dealing with these issues

is straight-forward, but rather time-consuming: By manually guessing the correct shape of the single-particle potential, it can be brought close enough to its fixed point to allow for convergence after further iterations. Likewise, results of similar configurations (e.g. same density, but different interaction) can serve as a reasonable starting point for further calculations.

5 RESULTS AND DISCUSSION

When performing the BHF calculations as described in the previous chapter, there are several options – like the choice of the hyperon-nucleon potential or the values of the LECs – which all can have a significant impact on the results. Given the large number of possible configurations, we will isolate certain options and separately investigate their effect on the calculational results one at a time.

For the sake of simplicity, we have chosen one specific set of options that will be used if not stated otherwise. It consists of the continuous choice for the spectrum of intermediate states, N3LO(500) for the NN two-body interaction, NLO13(500) for the YN two-body interaction, and a single-particle potential cutoff (see section 5.1.2) of $\Lambda_{\text{spp}} = 600$ MeV.

5.1 TECHNICAL CHALLENGES AND LIMITATIONS

Several technical challenges begin to emerge when investigating the single-particle potentials for densities around $3\rho_0$. Some of these are pitfalls of the numerics that can be easily dealt with once they are recognized, while some will prove to be real obstacles. In any case, all of them need to be examined first before one can turn to the actual results.

5.1.1 *Fitting the single-particle potentials*

Early optimization attempts consisted of approximating each single-particle potential by the form

$$U(k) = (U_0 + ak^2 + bk^4) \cdot \exp\left\{-2\left(\frac{k}{\Lambda}\right)^e\right\}, \tag{5.1}$$

where U_0 is $U(k = 0)$, and the other parameters a, b, Λ, and e were obtained from fitting the k-dependence. The number of grid points on which U was calculated ranged around 8 points, roughly spaced in steps of 150 MeV. This approach lead to a significant speed-up in comparison to pure grid calculations with dozens of points.
While this proved to be a viable strategy at lower densities, severe problems showed up at higher densities ($\rho \gtrsim 2.5\rho_0$), making it impossible to reasonably fit $U(k)$ to the data points. The origins of this issue will be further investigated in sections 5.1.2 and 5.1.4. It is almost impossible to (manually) detect and exclude faulty results if only a handful of data points are computed, which makes a full grid calculation with dozens of grid points a necessary strategy.

5.1.2 *Regulation of single-particle potentials*

As already pointed out in Ref. [66], $U_N(k)$ exhibits oscillations for momenta well above the chiral cutoff (Fig. 5.1). While the oscillations are already present for low densities around ρ_0, they become more pronounced for larger densities, increasing both in size and frequency.

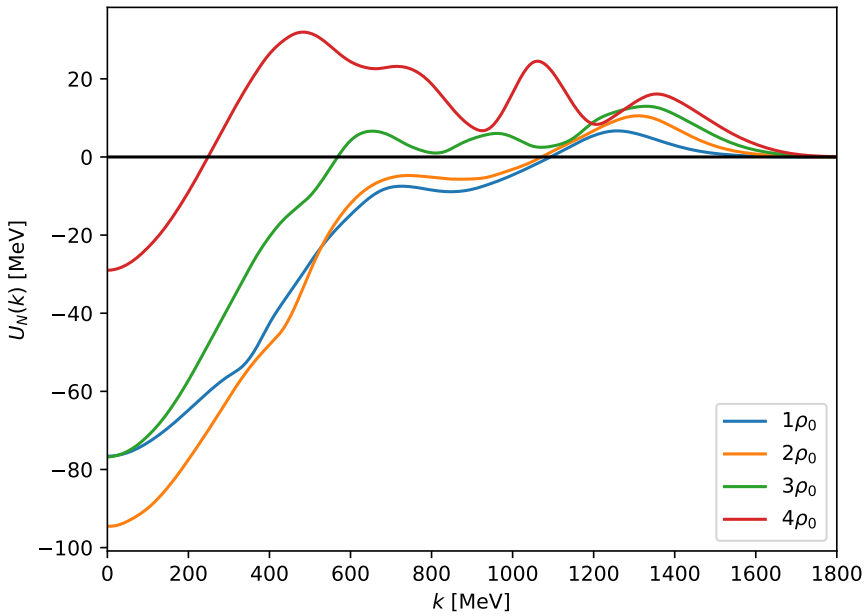

Figure 5.1: $U_N(k)$ in SNM for various densities without a single-particle cutoff. Three-nucleon forces are included.

Because of the chiral cutoff $\Lambda \approx 500$ MeV that suppresses high-momentum interactions, one would not expect such contributions to appear in the single-particle potential. Therefore we apply – in analogy to ChEFT and similar to Ref. [66] – a cutoff to the single-particle potential:

$$U(k) \to U(k) \cdot \exp\left(-(k/\Lambda_{\text{spp}})^6\right). \tag{5.2}$$

For consistency reasons, this cutoff is applied to nucleons and hyperons in the same way. Despite the significant modification of the large-momentum behavior, this cutoff barely changes the potential in the low-momentum region, as shown in Figs. 5.2 and 5.3. Note that around $3\rho_0$ a cutoff of $\Lambda_{\text{spp}} = 600$ MeV will result in a consistently more attractive potential than for other cutoffs, which is not only the case in this example, but a general observation. This is to be expected because of the almost purely repulsive nature of both U_Λ and U_Σ at these densities, which gets more suppressed by lower cutoffs. For the sake of computational speed, we will adopt $\Lambda_{\text{spp}} = 600$ by default. With this in mind, all results should be understood as a lower boundary to the "actual value", i.e. if the cutoff had not been applied.

5.1.3 *Density dependence of U_Λ beyond $3.5\rho_0$*

For large enough densities, around $3.5\rho_0$, the results for $U_\Lambda(k_1 = 0)$ start to flatten (see Fig. 5.4), which is not to be expected from naive considerations, because the interactions are not expected to weaken with increasing densities and the integral limits in eq. (4.23) already contribute by a factor of ρ.

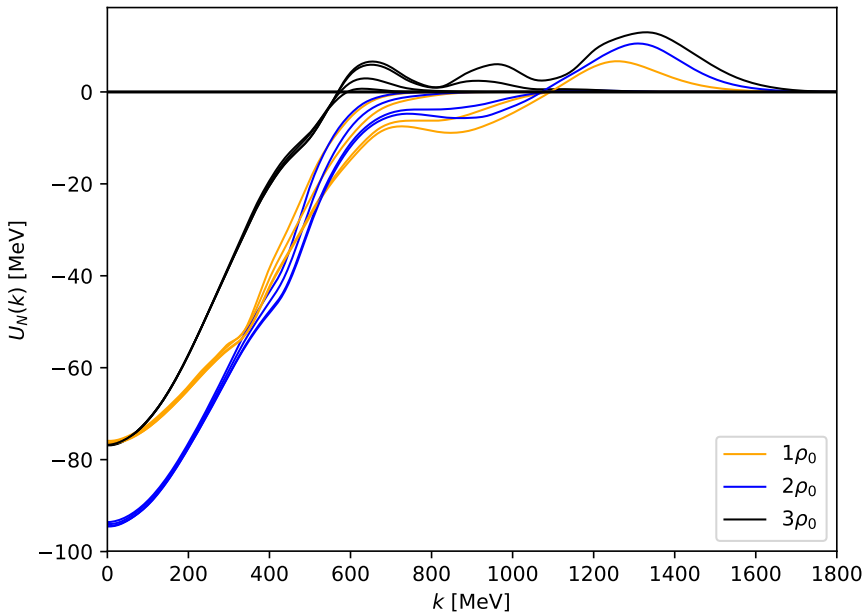

Figure 5.2: $U_N(k)$ in SNM for various choices of $\Lambda_{\text{spp}} \in \{600, 700, 1000, \infty\}$ MeV. Three-nucleon forces are included.

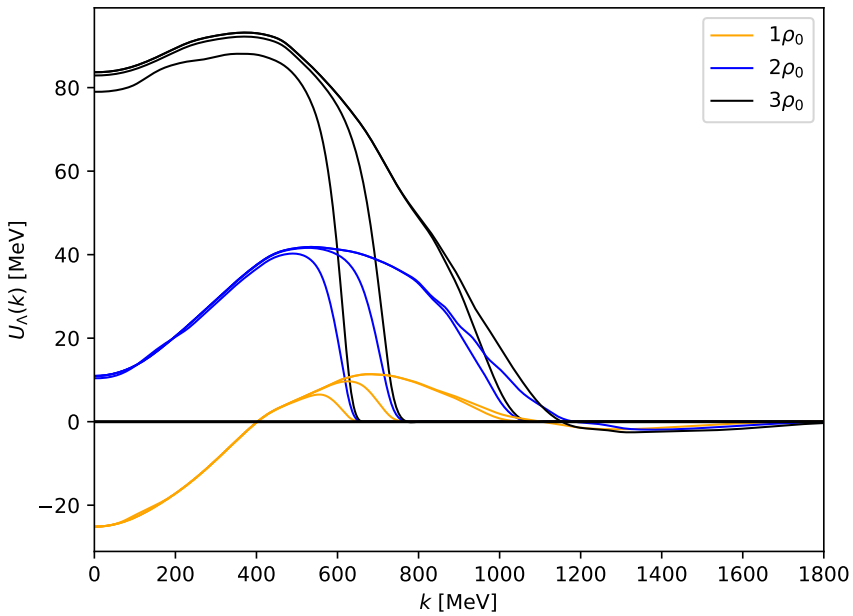

Figure 5.3: $U_\Lambda(k)$ in SNM for various choices of $\Lambda_{\text{spp}} \in \{600, 700, 1000, \infty\}$ MeV. Three-body forces are included, with $(H_1, H_2) = (-0.1, 0.5)$.

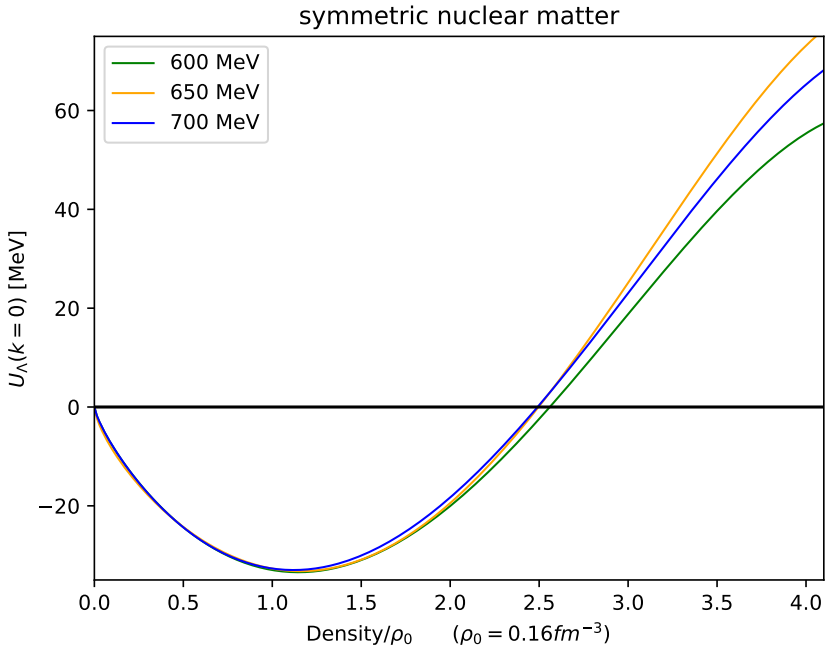

Figure 5.4: U_Λ in SNM for densities above $3.5\rho_0$. Only two-body forces are considered. The curves represent different values of Λ_{spp}.

The observed behavior in Fig. 5.4 is an artifact of the cutoff, as can be seen by first looking at the Pauli blocking operator Q in eq. (4.15): For $k_1 = 0$ and $k_F^{(\Lambda)} = 0$, Q only contributes if $k_{\text{BGE}} > k_F^{(N)} - \xi_{12} k_{\text{spp}}$, which for $k_{\text{spp}} \in [k_{\min}, k_{\max}]$ ranges from $k_{\text{BGE}} > k_F^{(N)}$ to $k_{\text{BGE}} > \frac{k_F^{(N)}}{1+\xi_{12}}$.

With the chiral cutoff of 500 MeV in mind, the support of Q is

$$\frac{k_F^{(N)}}{1+\xi_{12}} \lesssim k \lesssim 500 \text{ MeV}\,. \tag{5.3}$$

In the limit of very large Fermi momenta, this interval shrinks progressively, which implies the suppression of higher-order ladder contributions, with only the Hartree approximation $G = V$ eventually remaining. In reality, densities of $3.5\rho_0$ correspond to Fermi momenta of around 500 MeV in PNM and 400 MeV in SNM, which seem to be sufficient for this effect to kick in.

By further investigating the single-particle potential as given in eq. (4.23), we see that for large $k_F^{(N)}$ its derivative with respect to the density becomes

$$\frac{d}{d\rho} U_\Lambda^{(N)}(k_1 = 0) \propto V_{(\Lambda N)(\Lambda N)}(k_{\max}, k_{\max}) \overset{k_F^{(N)} \gtrsim 500 \text{ MeV}}{\approx} 0\,, \tag{5.4}$$

thus explicitly exhibiting the flattening property.

A proper understanding of this artifact is crucial for the high-density extrapolations as described in section 5.3.1.

5.1.4 *Instabilities at higher densities*

For densities around $4\rho_0$, it may become prohibitively difficult to obtain stable solutions. One source of these instabilities is the strength of the bare potential V. When solving the discretized

Bethe-Goldstone-equation, one needs to invert the matrix $(\mathbb{1} - V\frac{Q}{e})$, whose determinant may become zero for large enough densities or low-energy constants $H_{1,2}$, resulting in poles of $G(k,k)$. Simple roots of the determinant with respect to k can be dealt with by principal value treatment, but eventually this will not suffice for certain configurations, e.g. when the G-matrix has a double pole.

The process in which these instabilities arise typically is a rather gradual one. Once the density or the LECs become too large, U_Σ will more often exhibit an erratic behavior and even feature sharp peaks with unphysical values in the GeV region. The procedure on how to deal with this was discussed in section 4.5.4. Because of this slow onset of the instabilities, we err on the side of caution and choose $3.5\rho_0$ to be the upper limit at which trustworthy results may still be obtained.

5.2 NUCLEAR MATTER PROPERTIES

The calculation of the nucleon single-particle potential fulfills two purposes. Firstly, it is needed for subsequent calculations of the hyperon single-particle potentials. Secondly, nuclear matter properties like the energy per particle can be inferred from it, c.f. section 4.3.

An important thing to note is that Brueckner-Hartree-Fock calculations of nuclear matter properties have already been performed by far more sophisticated and reliable approaches [106, 107]. Therefore, in section 5.3.6 we will not use the neutron chemical potential obtained from BHF calculations, but rather use a state-of-the-art chemical potential obtained from functional renormalization group (FRG) approaches [107].

Nevertheless, in this section we will compute (density-dependent) properties of symmetric nuclear matter and pure neutron matter from BHF theory and compare them against other findings, like the results from the variational chain summation method of Akmal et al. [106] (APR) that uses the Argonne v_{18} potential [24] (AV18), results from Brueckner-Hartree-Fock calculations of Isaule et al. [108] (IAR) that also employ AV18, and results from gravitational wave constraints of Annala et al. [109]. The goal is to establish the fact that our nucleon single-particle potential provides a sensible baseline for subsequent hyperon calculations.

Fortunately, even if our U_N cannot perfectly reproduce sophisticated many-body approaches, the hyperon calculations will not be affected considerably, because the exact shape of the potential is not that relevant at low densities. See section 5.3.2, where we see that a difference between N3LO(500) and AV18 is basically non-existent for densities below $2.5\rho_0$.

5.2.1 *Energy per particle and chemical potential*

We start with computing the energy per particle E/A and chemical potential μ according to eqs. (4.34) and (4.35), yielding the results shown in Fig. 5.5. For comparison, results are given for pure two-body calculations – N3LO(414), N3LO(450), and N3LO(500) – as well as for the inclusion of three-body forces as elaborated on in section 3.3.

It is apparent that 3BFs are required to reproduce the APR results shown in black. The results for E/A turn out to be flatter than those of APR, with PNM being close to the lower border of the APR band and SNM lying even above APR for intermediate densities around ρ_0. While the low-density behavior ($\rho \ll \rho_0$) of ChEFT and APR coincide for PNM, this is not the case for SNM, where APR lies substantially higher. Interestingly, the result of IAR

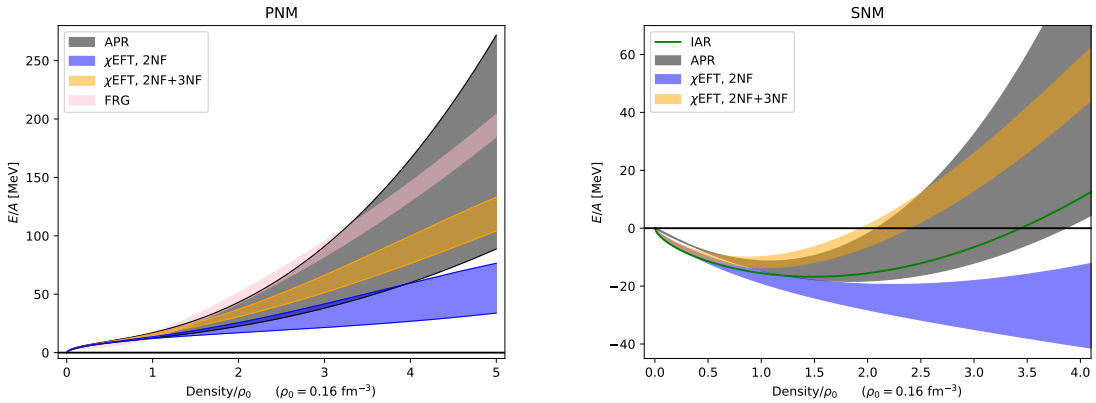

Figure 5.5: Energy per particle E/A for PNM (left) and SNM (right). The pure chiral N3LO two-body force calculations are shown in blue. They comprise the three chiral cutoff choices of 414, 450, and 500 MeV. The orange curve additionally incorporates N2LO three-nucleon forces. For comparison, APR (black), FRG (pink) and IAR (green) results are given.

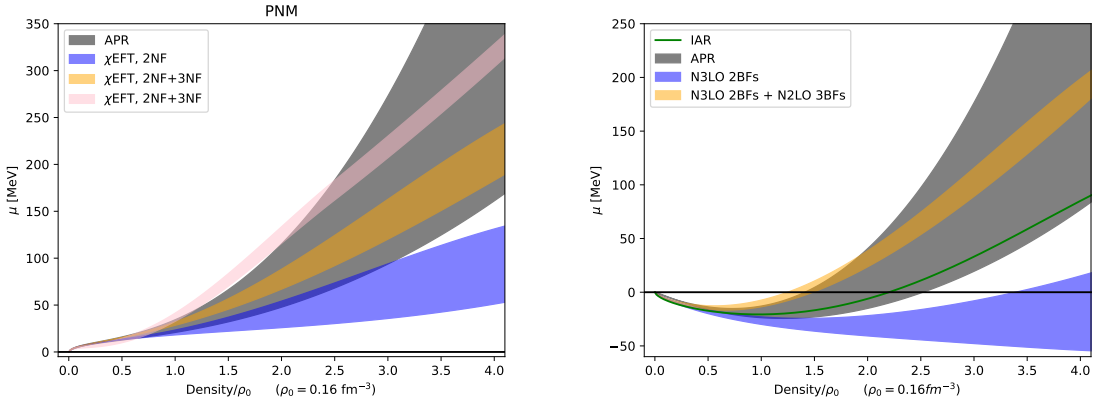

Figure 5.6: Chemical potential μ derived from E/A for PNM (left) and SNM (right). Same description as figure 5.5.

has the same shortcomings in reproducing the APR equation of state, even though the lower boundary of the APR band exactly comes from the AV18 potential as well. This suggests that the difference of the low-density behavior stems from the calculational procedure instead of the input potentials.

5.2.2 *Pressure*

The next quantity we compute is the pressure $p(\epsilon)$ as given in eq. (4.36) of PNM as a function of the energy density ϵ according to eq. (4.36). Our results are plotted against those from Fig. 3 of Ref. [109], where constraints on the pressure were obtained from gravitational wave observations (see Fig. 5.7). Note that the energy density in Ref. [109] is relativistic, which differs from the one given in eq.(4.34) by the term $M_N \cdot \rho$ and needs to be included.

Again, it is apparent that the two-body forces (blue lines) are insufficient to describe pure neutron matter, entering the light-blue region of the plot around $\epsilon \approx 200 - 300$ MeV/fm^{-3} and

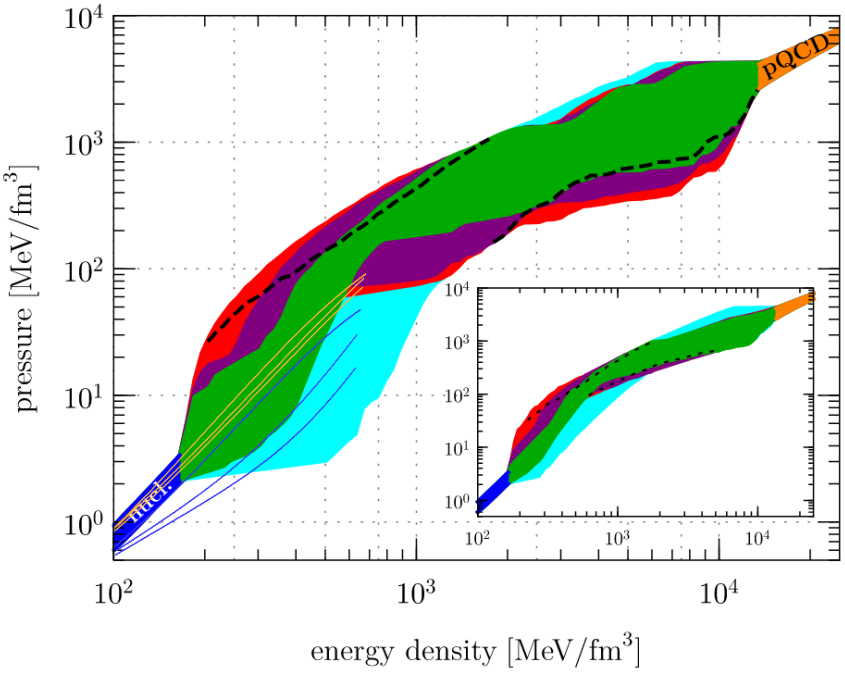

Figure 5.7: Comparison of chiral BHF calculations of the pressure in PNM with constraints from gravitational wave observations. Colored regions are taken from [109]. Light-blue areas indicate EOSs that can not support 2 $M_\odot$ neutron stars. Matter in the red and purple regions is excluded at a certain confidence level. The 3NF calculations are orange, the 2BF are blue. For both colours, top to bottom: (500/414/450) MeV cutoff.

even leaving the shaded region at lower densities. The results with 3NF included (orange lines), on the other hand, fit very well into the green range up to around $\epsilon = 550 - 650$ MeV/fm^{-3}, at which the N3LO(450) curve enters the light-blue region and the N3LO(414)/N3LO(500) lines hit the red/purple areas, respectively. This energy density corresponds to a matter density of roughly $3.5\rho_0$, further indicating that this should be the upper limit for the present calculations.

5.3 LAMBDA HYPERONS IN NUCLEAR MATTER

Now we turn towards calculations of the Λ single-particle potential. At first, we analyze results from YN two-body interactions alone and later include YNN three-body forces. A central constraint when adjusting the strength of the three-body forces in symmetric nuclear matter is the potential depth

$$U_\Lambda(\rho_0) = -30 \text{ MeV}\,, \tag{5.5}$$

which is empirically obtained from the spectroscopy of Λ hypernuclei [6, 110–112]. From the single-particle potential, we then compute the (relativistic) chemical potential of the Λ as

$$\mu_\Lambda(\rho) = \left.\frac{\partial\epsilon}{\partial\rho_\Lambda}\right|_{\rho_\Lambda=0} = M_\Lambda + U_\Lambda(k_1 = 0, \rho)\,. \tag{5.6}$$

5.3.1 *Fit of the density-dependence*

A simple polynomial fit of $U_\Lambda(k_1 = 0, \rho)$ is not possible because of the flattening discussed in section 5.1.3, which is characteristic for regularized potentials. This requires special care in order to sensibly incorporate high-density results into the fitting procedure.

The first step is to establish which density dependence is expected for higher densities. For $\rho \gtrsim 2\rho_0$, the results for YN two-body interactions exhibit a linear dependence in ρ, reminiscent of a Hartree potential, where the only density contribution comes from the integral limits in eq. (4.23). The YN three-body body interactions lead to an additional factor ρ, so $U_\Lambda(k_1 = 0, \rho)$ is then expected to scale quadratically for $\rho \gtrsim 2\rho_0$

Fits of the low-density region still require a cubic polynomial, which will then smoothly turn over into a linear or quadratic behavior for calculations using two-body or three-body interactions, respectively. Since the numerical data exhibit a significant flattening already around $3.0 - 3.5\rho_0$, this transition point is chosen to be around $2.5 - 3\rho_0$.

5.3.2 *Gap vs continuous choice, ChEFT vs AV18*

Both the gap and the continuous choice are prominent options in BHF calculations [65, 66]. Therefore it is instructive to directly compare them against each other. In order to check our results against Ref. [65], we also investigate the effect of using the IAR results for U_N [108]. For the sake of simplicity and comparability, this calculation is limited to YN two-body interactions only.

Fig. 5.8 shows that the results for the gap choice (dashed curves) are flatter than those for the continuous choice and more repulsive for lower densities, which qualitatively coincides with Fig. 4.5. It is important to note that $U_\Lambda(\rho_0) = -30$ MeV cannot be reproduced by the gap choice. This seems troublesome, because three-body forces are expected to add repulsive contributions, which would make it almost impossible to reproduce this empirical value. Repulsive forces only work very well with the continuous choice, where $U_\Lambda(\rho_0)$ lies below -30 MeV. This supports our decision of using the continuous choice.

AV18 on the other hand mostly yields more repulsive results. There is almost no difference between N3LO(500) and AV18 up to $2.5\rho_0$ for the continuous choice, whereas the difference is more pronounced for the gap choice, where it already becomes noticeable around ρ_0. Since there is no advantage in choosing one of the nucleon potentials over another in terms of reproducing empirical data, we will use ChEFT in order to stay consistent with YN interactions. Note that this choice will also lead to more conservative results in section 5.3.6.

The combined usage of the gap choice and AV18 reproduces the results of Ref. [65], serving as a non-trivial check for the correctness of our numerical implementation.

5.3.3 *NLO13 vs NLO19 YN two-body forces*

As elaborated on in section 2.6, there are two different outcomes of fitting the chiral YN two-body interaction, NLO13 and NLO19. Fig. 5.9 shows that NLO19(500) is substantially more attractive than NLO13(500), already lying 15 MeV lower at nuclear saturation density. This qualitatively coincides with the results in Ref. [96], although our results are considerably more attractive. Unlike NLO13, even using the gap choice and nucleon single-particle potentials

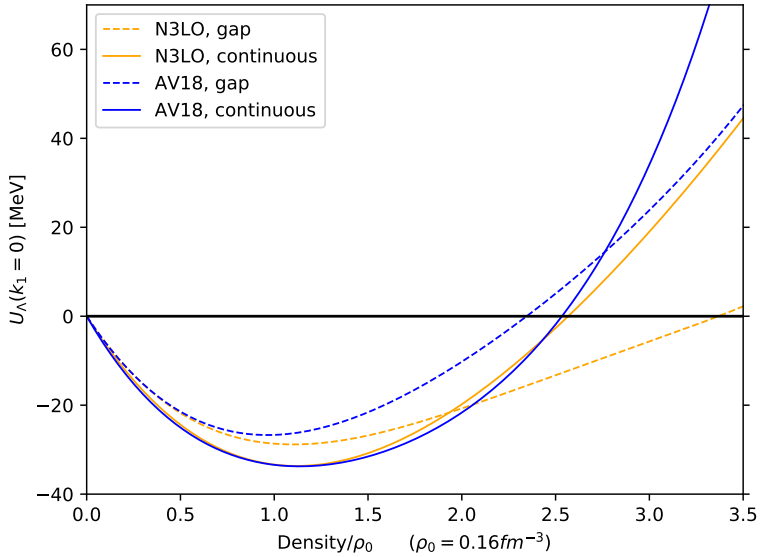

Figure 5.8: Λ single-particle potential for various combinations of continuous vs. gap choice and chiral N3LO vs. AV18 for the NN interaction. Only YN 2BFs are considered. Solid/dashed curves represent the continuous/gap choice, respectively. Orange/blue curves correspond to N3LO/AV18, respectively. The gray dotted line represents $U_\Lambda = -30$ MeV and will be featured in all SNM plots hereafter.

of IAR does not fully explain these differences. This indicates that there might be another influence that is not accounted for.

5.3.4 *Chiral cutoff dependence*

The YN two-body interaction NLO13 is available for several cutoffs, of which we will adapt those with the smallest χ^2 values when fitted to experimental YN-scattering data, namely $500, 550, 600, 650$, and 700 MeV [51]. Figure 5.10 shows a strong dependence of U_Λ on the cutoff. NLO(550) and NLO(600) provide the most repulsion with $U_\Lambda(\rho_0)$ staying well above the -30 MeV benchmark, making them unsuitable for further calculations, just like the gap choice. The other three cutoff choices yield enough attraction for $U_\Lambda(\rho_0)$ to fall well below -30 MeV, with NLO(700) introducing so much attraction that U_Λ will stay attractive even for densities up to $3.5\rho_0$. For computational simplicity, only NLO13(500) and NLO13(650) will be used in the following, as they are the most repulsive choices while still staying below -30 MeV, thus requiring the least amount of repulsion from three-body interactions.

5.3.5 *Exploring the H_1H_2-plane*

In the ΛNN diagonal channel, H_1 and H_2 contribute only through the linear combination $H' = H_1 + 3H_2$. Dimensional arguments have been invoked to estimate its order of magnitude to $H' \approx \pm 1/f_0^2$ [65], with the pion decay constant $f_0 \approx 92$ MeV. Consequently, we expect H_1

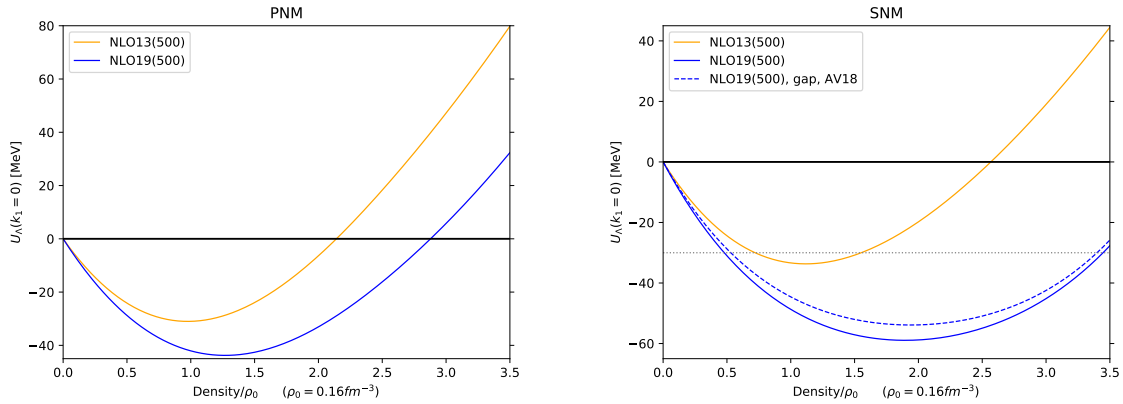

Figure 5.9: $U_\Lambda(k_1 = 0)$ calculated from NLO13 (orange) and NLO19 (blue) in PNM and SNM. The SNM results also feature a different set that applies the gap choice and uses IAR results for U_N.

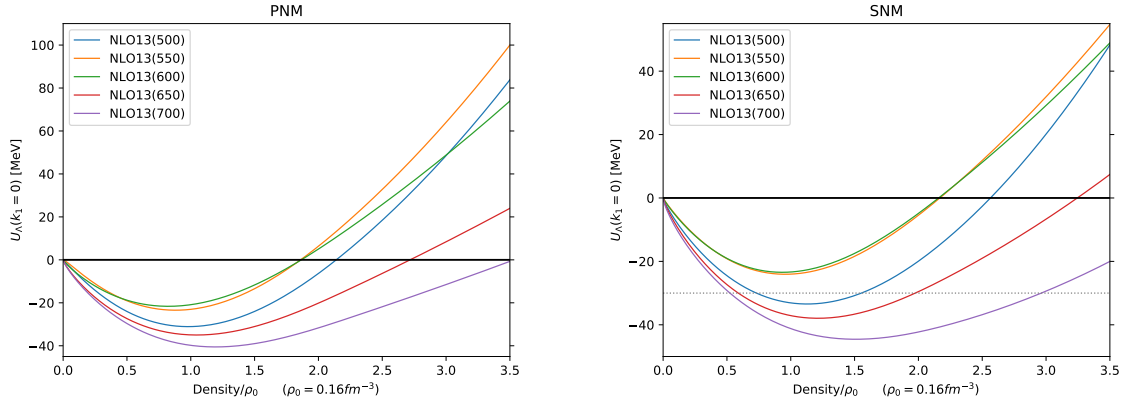

Figure 5.10: $U_\Lambda(k_1 = 0)$, calculated from NLO13 using different chiral cutoffs, ranging from 500 to 700 MeV.

NLO13(500)				NLO13(650)				NLO19(500)			
line 1		line 2		line 1		line 2		line 1		line 2	
H_1	H_2	H_1	H_2	H_1	H_2	H_1	H_2	H_1	H_2	H_1	H_2
−2.65	0.1	−2.47	1.2	−3.0	−0.4	−1.4	1.9	−2.7	−0.3	−2.5	1.67
−2.2	0	−2	1	−1.8	−0.5	−1.1	1.7	−1.6	−0.6	−2	1.47
−1.8	−0.1	−1.55	0.8	−0.9	−0.6	−0.4	1.2	−0.5	−0.91	−1.5	1.27
−1.35	−0.2	−1.1	0.6	0	−0.7	0.1	0.9	0	−1.06	−1.0	1.07
−0.9	−0.3	−0.6	0.4	0.6	−0.8	0.7	0.6	0.5	−1.2	0	0.72
−0.05	−0.5	−0.1	0.2	1.6	−1	1.5	0.2	1.45	−1.5	0.5	0.52
0.9	−0.7	0.5	0	2.3	−1.2	2.7	−0.2			1.2	0.3
1.5	−0.9	1.05	−0.2							2.15	0
		1.6	−0.4								
		1.9	−0.5								

Table 5.1: Pairs of H_1 and H_2 that reproduce $U_\Lambda(\rho_0) = -30$ MeV for the given YN two-body interaction, c.f. Figs. 5.11 and 5.12

and H_2 themselves to be of similar magnitude. In the following, H_1 and H_2 will always be given in units of $1/f_0^2$.

Within this range, both LECs have a substantial influence on the properties of the hyperon single-particle potentials, being able to introduce both repulsion and attraction at nuclear saturation density. While the amount of repulsion can be almost arbitrary by choosing extreme values, the amount of attraction is limited to a few MeV, which rules out two-body interactions that yield $U_\Lambda(\rho_0) > -30$ MeV to begin with.

Since H_1 and H_2 are not (yet) fixed from experimental data, we take the liberty of choosing them in a way that suits best for our purpose. By calculating $U_\Lambda(\rho_0)$ in symmetric nuclear matter on the two-dimensional H_1H_2-grid (Figs. 5.11 and 5.12), we identify two curves in the H_1H_2-plane that satisfy the constraint 5.5. As these curves do not intersect, they divide the plane into three regions: The area between the curves, where $U_\Lambda(\rho_0) < -30$ MeV, and the areas outside, where $U_\Lambda(\rho_0) > -30$ MeV.

Since NLO13(650) and NLO13(700) both yield more attractive results for U_Λ than NLO13(500) (c.f. Fig. 5.10) and thus require more repulsion coming from the three-body interaction, it comes as no surprise that the lines in the H_1H_2-plane become more separated for higher cutoffs, with no sign of them intersecting even outside of the plotted region. Interestingly, even though NLO19(500) yields the largest attraction out of the examined YN two-body forces (c.f. Fig. 5.9) and would therefore be expected to require the most extreme values of $H_{1,2}$, this is actually not the case. While the two lines indeed are more separated than those of NLO13(500), they stay relatively close to the black reference line, as opposed to NLO13(650) and especially NLO13(700), which seem to wander off for smaller H_1 or larger H_2.

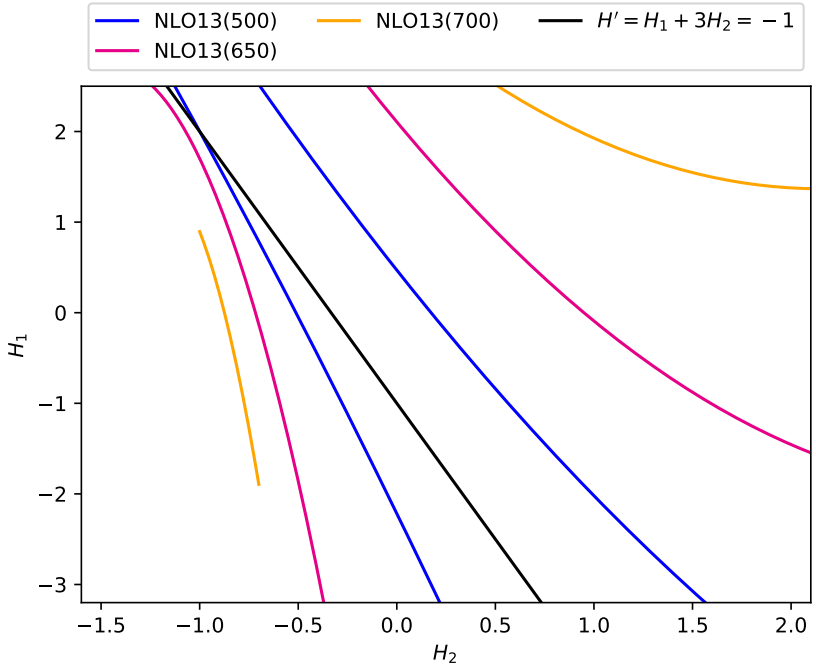

Figure 5.11: $U_\Lambda(\rho_0)$ calculated on H_1H_2-grid. $H_{1,2}$ are given in units of $1/f_0^2$. Colored lines represent those (H_1, H_2)-pairs that reproduce $U_\Lambda(\rho_0) = -30$ MeV in SNM. For reference, the black line indicates $H_1 + 3H_2 = -1$

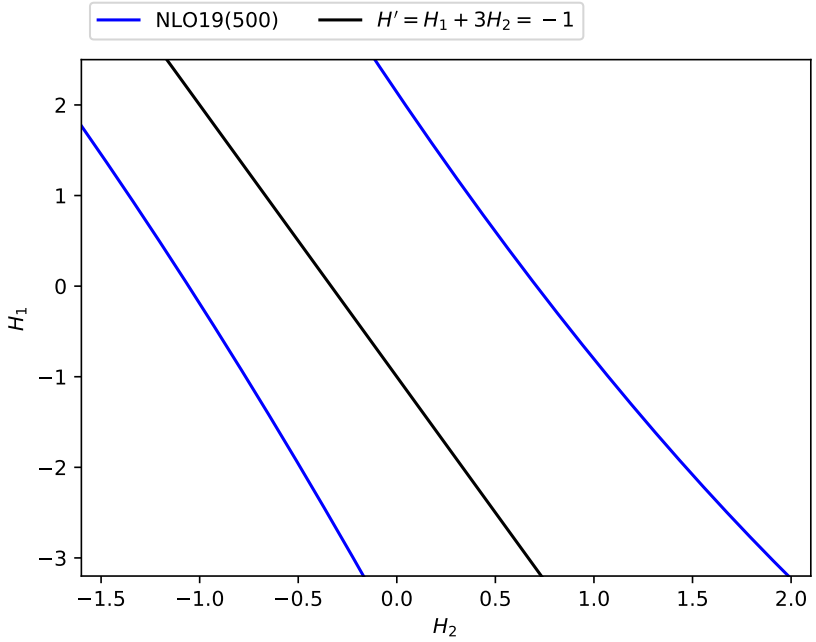

Figure 5.12: $U_\Lambda(\rho_0)$ calculated on H_1H_2-grid. Same caption as Fig. 5.11

5.3.6 *Comparison of chemical potentials in pure neutron matter*

While staying on the aforementioned lines in the H_1H_2-plane, we calculated $U_\Lambda(3\rho_0)$ in PNM for various (H_1, H_2)-pairs. The value of $3\rho_0$ was chosen in order to avoid the flattening effect discussed in section 5.1.3.

For the calculations in this section, we used $\Lambda_{\text{spp}} = 700$ MeV in order to obtain sufficient repulsion, in contrast to $\Lambda_{\text{spp}} = 600$ MeV which would yield too attractive results, as discussed in section 5.1.2.

The neutron chemical potential from Ref. [107] takes values of $\mu_n(2.5\rho_0) = 1126.6$ MeV and $\mu_n(3\rho_0) = 1180.5$ MeV, so that $U_\Lambda(2.5\rho_0) > 10.9$ MeV and $U_\Lambda(3\rho_0) > 64.8$ MeV need to hold in order to be repulsive enough for $\mu_\Lambda > \mu_n$ at the respective densities. The range in which H_1 and H_2 provide sufficient repulsion is strongly dependent on the YN two-body interaction, as can be seen in Figs. 5.13a, 5.13b, 5.14 for NLO13(500), NLO19(500), and NLO13(650), respectively.

For NLO13(500), increasingly large absolute values of H_1 mostly provide more repulsion to $U_\Lambda(3\rho_0)$. Both curves exhibit a minimum around $H_1 \approx -0.5$, with both minima not falling below the threshold, so no (H_1, H_2)-combination can be instantly ruled out. By calculating lower-density values, however, it becomes apparent that the slope of $U_\Lambda(\rho)$ is too flat for some combinations to yield enough repulsion at higher densities, as shown in figures 5.15 and 5.16. For line 1, the combinations that provide enough repulsion are roughly characterized by $H_1 \notin [-1.5, 0.5]$. For line 2, this range is $H_1 \gtrsim 0.5$.

Unlike NLO13(500), there is no local minimum for NLO19(500). Instead, $U_\Lambda(H_1)$ seems to fall indefinitely for low values of $H_{1,2}$. This makes it readily apparent that some choices for H_i are not repulsive enough. Further looking at the density dependence in total (see Figs. 5.17 and 5.18), we can identify that $H_1 \gtrsim -2.5$ for line 1 and $H_1 \gtrsim -1.5$ for line 2 provide enough repulsion.

Note that the results for NLO13(500) and NLO19(500) are of comparable size, even though NLO19(500) introduced substantial attraction (c.f. Fig. 5.9). This might not come as a surprise, since H_1 and H_2 need to be chosen in such a way that they compensate the mentioned attraction. Since this repulsion grows with density, it will eventually close the gap between NLO13(500) and NLO19(500) at high densities as well.

As mentioned in section 5.1.2, we can expect U_Λ to be a few MeV more repulsive than given here because of the choice of Λ_{spp}. Therefore, the given ranges for $H_{1,2}$ can be seen as somewhat conservative. Similarly, using AV18 would also make it more repulsive: The two lines in the H_1H_2-plane would stay unchanged, since AV18 does not change the results for $U_\Lambda(\rho_0)$ in SNM, but we have seen that is adds substantial repulsion at large densities.

In contrast to the other results, NLO13(650) yields so much attraction that it is sufficient to compare the chemical potentials at $2.5\rho_0$ instead. This is also necessary, because the amount of attraction compromises the stability, as discussed in section 5.1.4. While there are two combinations that provide enough repulsion for $U_\Lambda(2.5\rho_0)$ to surpass the threshold of 10.9 MeV, $(0, -0.7)$ and $(0.6, -0.7)$, they only yield 30 and 27 MeV at $3\rho_0$, respectively, which is too attractive. Therefore, we conclude that there is no (H_1, H_2) combination that can introduce enough repulsion for NLO13(650). Similar observations can be made for NLO13(700), where $U_\Lambda(2.5\rho_0)$ shows a comparable level of attraction. Furthermore, we observed that NLO13(650) and NLO13(700) may yield attractive Σ single-particle potentials, a feature which is absent for

NLO13(500) and NLO19(500). This is unfavorable, as the repulsiveness of $U_\Sigma(\rho_0)$ in symmetric nuclear matter has been fairly well established [6] and therefore should be expected for higher densities in PNM as well. Hence, it is highly questionable whether NLO13(650) and NLO13(700) are suitable choices for a YN two-body interaction in the first place.

It is important to note that for a proper discussion of neutron star properties, the effect of a proton admixture needs to be accounted for. The proton fraction of beta-stable matter lies in the few percent range and is governed by the equilibrium condition $\mu_n = \mu_p + \mu_e$. Test calculations in which we used the proton fraction of the APR EoS indicate that $U_\Lambda(3\rho_0)$ becomes at most 10 MeV more attractive than in PNM, which is well within the uncertainty bands.

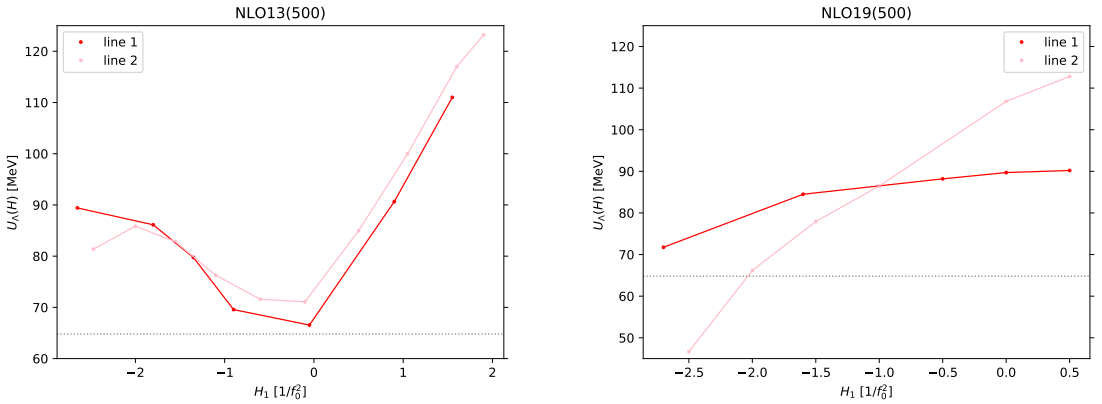

(a) (b)

Figure 5.13: $U_\Lambda(H_1)$ at $3\rho_0$ in PNM for NLO13(500) (a) and NLO19(500) (b) along the two lines in the H_1H_2-plane. The horizontal line represents the minimum-required value of 64.8 MeV. Only H_1 is given on the horizontal axis, the corresponding value for H_2 (on either line) can be looked up in Table 5.1.

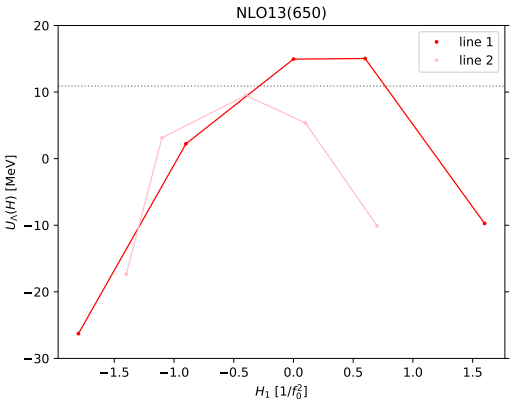

Figure 5.14: $U_\Lambda(H_1)$ at $2.5\rho_0$ in PNM for NLO13(650) along the two lines in the H_1H_2-plane. The horizontal line represents the minimum-required value of 10.9 MeV. Only H_1 is given on the horizontal axis, the corresponding value for H_2 (for either line) can be looked up in table 5.1.

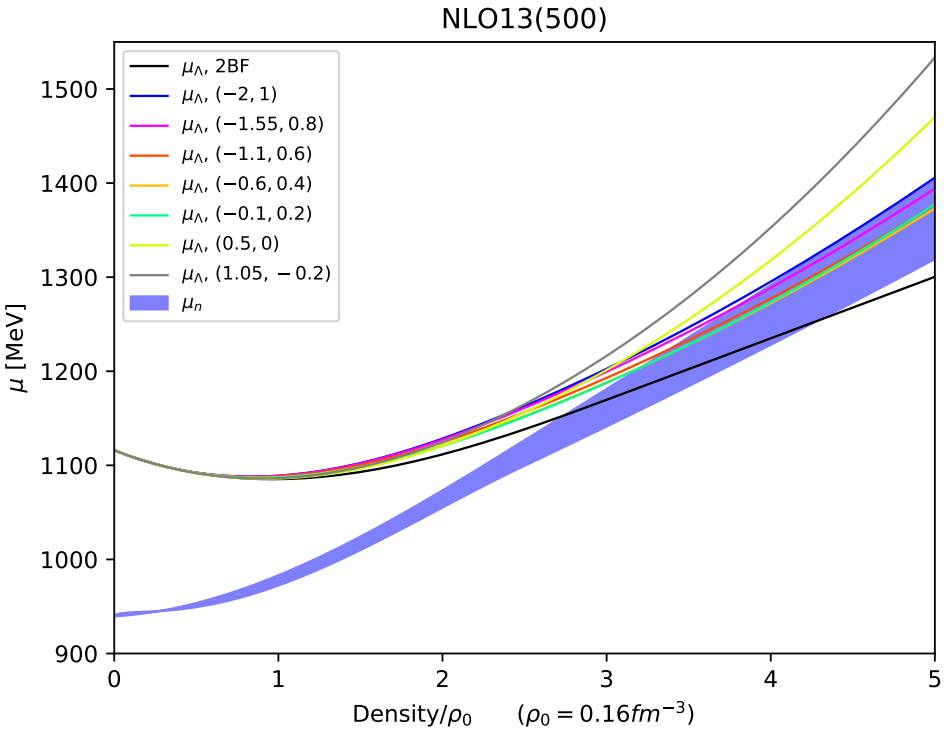

Figure 5.15: Comparison of the chemical potentials of the Λ-baryon and neutrons in pure neutron matter for various choices of H_1 and H_2 along line 1. 2BF results from NLO13(500) are given in black for comparison.

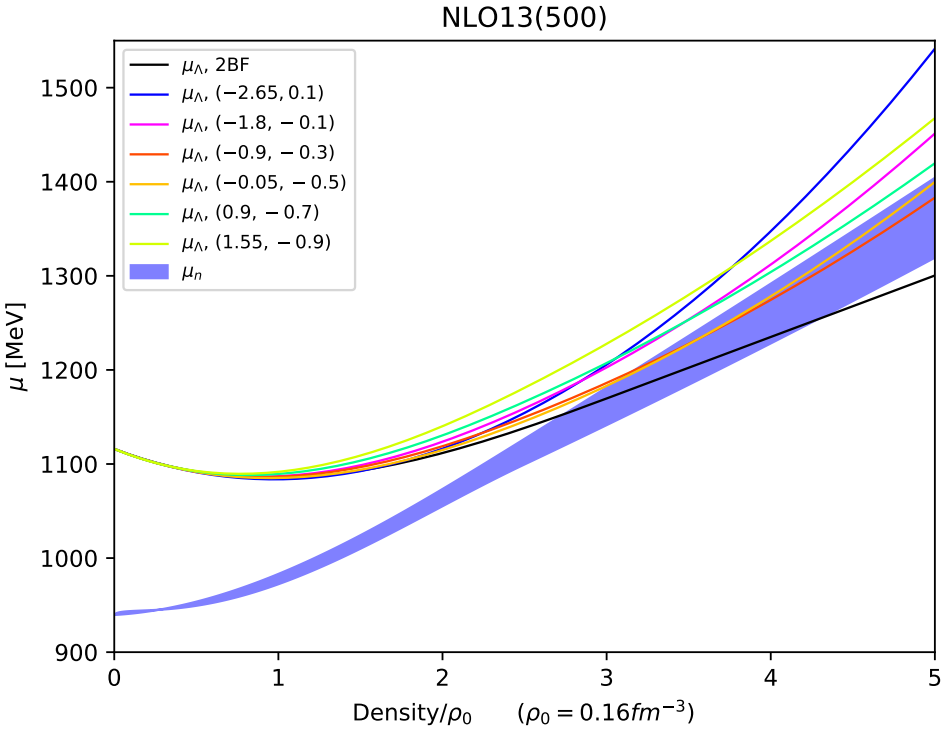

Figure 5.16: Comparison of the chemical potentials of the Λ-baryon and neutrons in pure neutron matter for various choices of H_1 and H_2 along line 2. 2BF results from NLO13(500) are given in black for comparison.

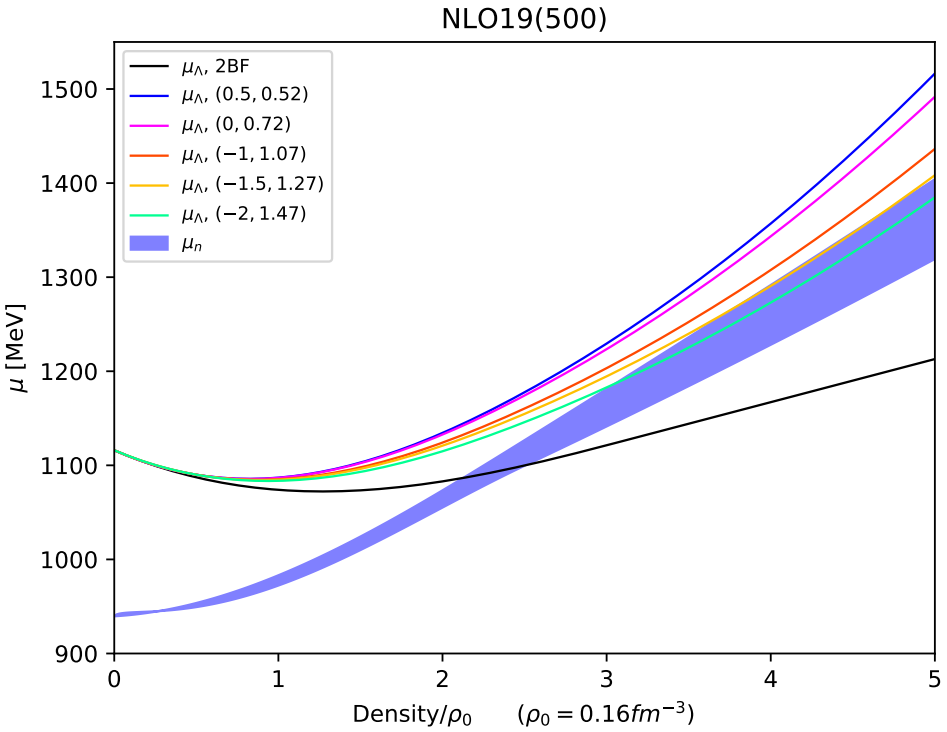

Figure 5.17: Comparison of the chemical potentials of the Λ-baryon and neutrons in pure neutron matter for various choices of H_1 and H_2 along line 1. 2BF results from NLO19(500) are given in black for comparison.

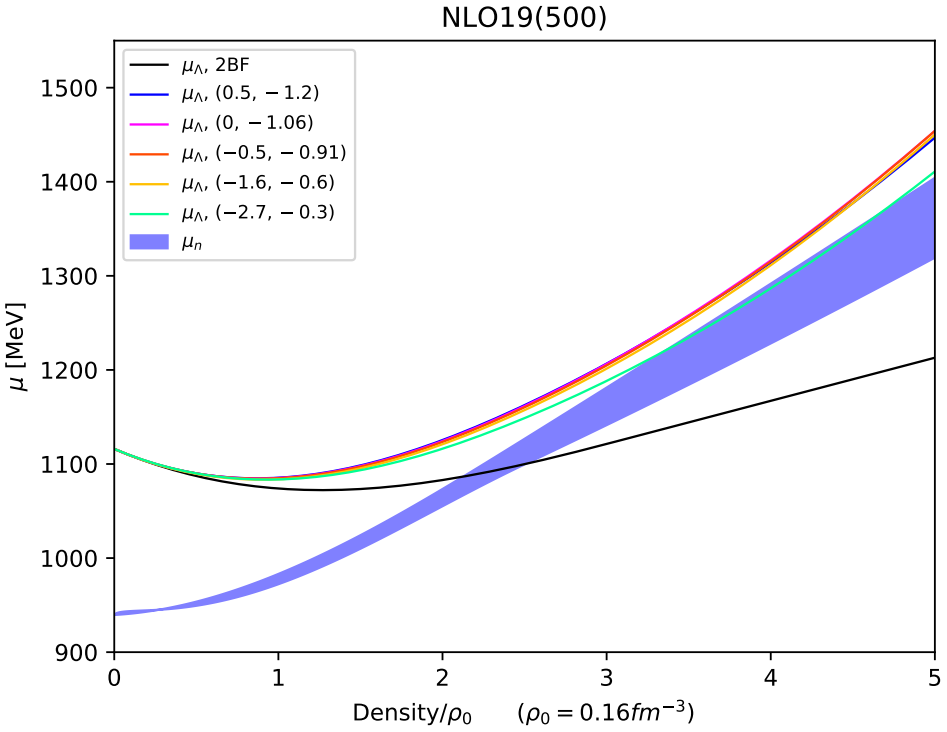

Figure 5.18: Comparison of the chemical potentials of the Λ-baryon and neutrons in pure neutron matter for various choices of H_1 and H_2 along line 2. 2BF results from NLO19(500) are given in black for comparison.

6

SUMMARY AND CONCLUSION

In this work, we investigated the condition for the onset of Λ-baryon formation in neutron stars by employing Brueckner theory at first order in the hole-line expansion and computing the single-particle potentials of nucleons and hyperons. The two-body interactions used were obtained from SU(2) ChEFT at N3LO for nucleon-nucleon interactions and from SU(3) ChEFT at NLO for hyperon-nucleon interactions. Three-body forces, which arise at N2LO, were incorporated as density-dependent effective two-body interactions. As a novelty, we derived the expressions for all YNN channels involving exactly one hyperon of strangeness $S = -1$, i.e. ΛNN-ΛNN, ΛNN-ΣNN, and ΣNN-ΣNN, in isospin-asymmetric nuclear matter.

We investigated the effect of several options that are available when performing Bruecker calculations. The single-particle potential of a Λ in the gap choice has a weaker dependence on the density than in the continuous choice, rendering it too shallow to fall below -30 MeV for the examined two-body interactions. Consequently, they leave no room for repulsive three-body forces. Similar shortcomings are observed for some of the chiral YN-interactions in the continuous choices, where only NLO13(500), NLO13(650), NLO13(700), and NLO19(500) are sufficiently attractive, while NLO13(550) and NLO13(600) yield too repulsive single-particle potentials.

The choice of different NN-potentials barely changes the low-density behaviour of U_Λ, but has a significant effect on the high-density results. As an alternative to ChEFT at N3LO, we explored AV18, which introduces substantial repulsion above $2.5\rho_0$, consequently favoring the absence of Λs. The addition of three-nucleon forces to AV18 is expected to underline this trend even more.

Since the experimental data on strange three-body forces is very scarce, the related LECs H_1 and H_2, which parametrize the 3-octet-1-decuplet contact interaction, are currently unconstrained. Even though different YN two-body potentials yield distinctive levels of attraction for U_Λ, we can always find continuous sets of (H_1, H_2)-pairs that are able to introduce the right amount of three-body repulsion to reproduce $U_\Lambda(\rho_0) = -30$ MeV. Each set takes the form of two separate lines in the H_1H_2-plane that vary significantly in position, depending on the YN two-body interaction. Furthermore, for NLO13(500) and NLO19(500) there are intervals along those two lines within which the LECs introduce sufficient repulsion such that $\mu_\Lambda > \mu_n$ holds for any density. Remarkably, NLO13(650) and NLO13(700) yield too attractive results for any (H_1, H_2)-combination, even though their results from two-body calculations alone are less attractive than NLO19(500).

At such high cutoffs, higher order terms in the chiral expansion might become relevant already, which are beyond what is currently achievable with the limited amount of YN-scattering data, as discussed before. The availability of NLO13 and NLO19, which provide substantially different results for U_Λ while excluding three-body forces, allows for an uncertainty estimate to some extent.

To conclude, we require a larger database for YN-scattering data and hypernuclei in order to obtain more reliable two- and three-body interactions. Even though a conclusive statement is not possible at this point, we were able to show that ΛNN three-body forces can indeed allow for sufficient repulsion in order to suppress the onset of Λ formation in neutron stars.

A

NOTATION AND BASICS

A.1 NOTATION

- We use natural units where $\hbar = c = 1$.
  Momentum units are written as MeV instead of MeV/c.
  Energy units are given as MeV instead of MeV/c^2.
- Latin indices range from 1 to 3, Greek indices range from 0 to 3.
- Summation over repeated indices is implied (Einstein summation convention)
  Latin indices then typically are both subscripts or both superscripts.
  Greek indices will feature one subscript and one superscript.
- The Minkowski metric tensor takes the form $g_{\mu\nu} = g^{\mu\nu} = \text{diag}(+1, -1, -1, -1)$
- Covariant and contravariant vectors are related by $x_\mu = g_{\mu\nu} x^\nu$
- The four-gradient can be written as $\partial_\mu = \frac{\partial}{\partial x^\mu}$
- The four-momentum of a particle reads $p^\mu = (E, \vec{p})$ with $p^2 = p^\mu p_\mu = E^2 - \vec{p}^2$
- The commutator or anticommutator of two operators reads:
  $[a, b] = ab - ba \quad \text{or} \quad \{a, b\} = ab + ba$
- A Lorentz scalar is obtained from Dirac spinors by $\bar{\Psi}\Psi$ with $\bar{\Psi} = \Psi^\dagger \gamma_0$
- The totally antisymmetric Levi-Civita tensor ϵ_{ijk} is normalized as $\epsilon_{123} = 1$
- Unitary group of degree N: $\text{U}(N) = \{U \in \mathbb{C}_{N\times N} |\ U^\dagger U = \mathbb{1}\}$
- Special unitary group of degree N: $\text{SU}(N) = \{U \in \text{U}(N) |\ \det(U) = 1\}$
- Its Lie algebra is the tangent space at the identity:

$$\mathfrak{su}(N) = \{X = c'(0) \in \mathbb{C}_{N\times N} \big|\ \text{ smooth } c : \mathbb{R} \to \text{SU}(N),\ c(0) = \mathbb{1}\}\,. \tag{A.1}$$

  A basis of $\mathfrak{su}(N)$ is also referred to as *generators* of SU(N).
- The generators of SU(2) are chosen as $\{i\sigma_i/2\}$, with the Pauli matrices σ_i:

$$\sigma_1 = \begin{pmatrix} 0 & 1 \\ 1 & 0 \end{pmatrix}, \qquad \sigma_2 = \begin{pmatrix} 0 & -i \\ i & 0 \end{pmatrix}, \qquad \sigma_3 = \begin{pmatrix} 1 & 0 \\ 0 & -1 \end{pmatrix}, \tag{A.2}$$

  with

$$\sigma_i \sigma_j = \delta_{ij} + i\epsilon_{ijk}\sigma_k, \qquad [\sigma_i, \sigma_j] = 2i\epsilon_{ijk}\sigma_k, \qquad \{\sigma_i, \sigma_j\} = 2\delta_{ij}\,. \tag{A.3}$$

  In the case of isospin space, the Pauli matrices τ_i are used instead.

- The generators of SU(3) are chosen as $\{i\lambda_i/2\}$, with the Gell-Mann matrices λ_i:

$$\lambda_1 = \begin{pmatrix} 0 & 1 & 0 \\ 1 & 0 & 0 \\ 0 & 0 & 0 \end{pmatrix}, \qquad \lambda_2 = \begin{pmatrix} 0 & -i & 0 \\ i & 0 & 0 \\ 0 & 0 & 0 \end{pmatrix}, \qquad \lambda_3 = \begin{pmatrix} 1 & 0 & 0 \\ 0 & 1 & 0 \\ 0 & 0 & 0 \end{pmatrix}$$
$$\lambda_4 = \begin{pmatrix} 0 & 0 & 1 \\ 0 & 0 & 0 \\ 1 & 0 & 0 \end{pmatrix}, \qquad \lambda_5 = \begin{pmatrix} 0 & 0 & -i \\ 0 & 0 & 0 \\ i & 0 & 0 \end{pmatrix}, \qquad \lambda_6 = \begin{pmatrix} 0 & 0 & 0 \\ 0 & 0 & 1 \\ 0 & 1 & 0 \end{pmatrix}$$
$$\lambda_7 = \begin{pmatrix} 0 & 0 & 0 \\ 0 & 0 & -i \\ 0 & i & 0 \end{pmatrix}, \qquad \lambda_8 = \frac{1}{\sqrt{3}} \begin{pmatrix} 1 & 0 & 0 \\ 0 & 1 & 0 \\ 0 & 0 & -2 \end{pmatrix}, \tag{A.4}$$

where

$$tr(\lambda_a) = 0, \qquad \lambda_a^\dagger = \lambda_a, \qquad \mathrm{tr}(\lambda_a \lambda_b) = 2\delta_{ab}\,. \tag{A.5}$$

The Lie bracket of two generators takes the form

$$\left[\frac{\lambda_a}{2}, \frac{\lambda_b}{2}\right] = i f_{abc} \frac{\lambda_c}{2}, \tag{A.6}$$

with the real and totally antisymmetric structure constants f_{abc}, which have the non-zero values

$$f_{123} = 1, \qquad f_{458} = f_{678} = \frac{\sqrt{3}}{2}$$
$$f_{147} = f_{165} = f_{246} = f_{257} = f_{345} = f_{376} = \frac{1}{2}\,. \tag{A.7}$$

- The gamma matrices read - in Dirac representation -

$$\gamma^0 = \begin{pmatrix} \mathbb{1} & 0 \\ 0 & -\mathbb{1} \end{pmatrix}, \qquad \gamma^i = \begin{pmatrix} 0 & \sigma^i \\ -\sigma^i & 0 \end{pmatrix}. \tag{A.8}$$

Together with

$$\gamma^5 = \gamma_5 = i\gamma^0\gamma^1\gamma^2\gamma^3 = \begin{pmatrix} 0 & \mathbb{1} \\ \mathbb{1} & 0 \end{pmatrix} \quad \text{and} \quad \sigma^{\mu\nu} = \frac{i}{2}[\gamma^\mu, \gamma^\nu]\,, \tag{A.9}$$

the set $\{\mathbb{1}, \gamma^\mu, \gamma_5, \gamma^\mu\gamma_5, \sigma_{\mu\nu}\}$ forms a basis for the space of all 4×4 Dirac matrices. The elements satisfy the relations

$$\{\gamma^\mu, \gamma^\nu\} = 2g^{\mu\nu}\,, \qquad \{\gamma^\mu, \gamma_5\} = 0\,,$$
$$\gamma_0^\dagger = \gamma_0\,, \qquad \gamma^{i\dagger} = -\gamma^i\,,$$
$$\gamma_5^\dagger = \gamma_5\,, \qquad \gamma_5^2 = \mathbb{1}\,, \qquad \sigma^{\mu\nu} = -\sigma^{\nu\mu}\,. \tag{A.10}$$

- The Feynman slash notation is an abbreviation for $\not{a} \coloneqq \gamma^\mu a_\mu$

B

DENSITY-DEPENDENT 2BFS IN ASYMMETRIC NUCLEAR MATTER

In this appendix we give explicit expressions for all density-dependent effective YN-potentials derived from YNN 3-body-potentials in the strangeness $S = -1$ sector for isospin-asymmetric matter, as sketched in chapter 3. We were able to reproduce the results from Ref. [64] for ΛN-ΛN. Furthermore, the results for ΛN-ΣN and ΣN-ΣN coincide in symmetric matter. As isospin symmetry cannot be used in asymmetric matter anymore, the results are given in the particle basis.

For the purpose of comparison with Ref. [64], the ΛN-ΛN potentials are split into two-pion-exchange, one-pion-exchange, and contact term contributions. The ΛN-ΣN and ΣN-ΣN transitions are broken down into contributions from each three-body topology, c.f. chapter 3. Furthermore, a conversion factor of $\sqrt{\frac{2}{3}}$ between isospin- and particle basis is factored out where convenient.

In addition to the notation introduced in Ref. [64],

$$\tilde{\Gamma}_i(p) = \Gamma_i(p, k_f^n) + 2\Gamma_i(p, k_f^p)\,, \tag{B.1}$$

$$\tilde{G}_i(p,q) = G_i(p, q, k_f^n) + 2G_i(p, q, k_f^p)\,, \tag{B.2}$$

we define

$$\Gamma^n(p) = \frac{2}{3}\,(k_F^n)^3 - m_\pi^2 \Gamma_0(p, k_F^n)\,, \tag{B.3}$$

$$\Gamma^p(p) = \frac{2}{3}\,\left(k_F^p\right)^3 - m_\pi^2 \Gamma_0(p, k_F^p)\,, \tag{B.4}$$

$$\Gamma_4(p, k_F) = \Gamma_0(p, k_F) + 2\Gamma_1(p, k_F) + \Gamma_3(p, k_F)\,, \tag{B.5}$$

$$\Gamma_5(p, k_F) = \Gamma_2(p, k_F) + \frac{1}{4} q^2 \Gamma_4(p, k_F)\,, \tag{B.6}$$

$$\hat{G}(p, q, k_F) = G_0(p, q, k_F) + 4G_1(p, q, k_F) + 4G_3(p, q, k_F)\,, \tag{B.7}$$

$$\gamma(p, q, k_F) = 2\Gamma_0(p, k_F) + 2\Gamma_1(p, k_F) - (q^2 + 2m_\pi^2)(G_0(p, q, k_F) + 2G_1(p, q, k_F))\,, \tag{B.8}$$

$$\begin{aligned}\kappa(p, q, k_F) = {} & \frac{8}{3}(k_F)^3 - 4(q^2 + 2m_\pi^2)\Gamma_0(p, k_F) \\ & - 2q^2\Gamma_1(p, k_F) + (q^2 + 2m_\pi^2)^2 G_0(p, q, k_F)\,,\end{aligned} \tag{B.9}$$

with $G_{0,1,2,3}(p, q)$ and $\Gamma_{0,1,2,3}(p)$ given in Ref. [63]

B.1 $\Lambda N \to \Lambda N$

B.1.1 $\Lambda n \to \Lambda n$

Two-pion-exchange:

$$\begin{aligned}\frac{C^2 g_A^2}{48 f_0^4 \pi^2 \Delta}\Bigg(&\frac{8}{3}\left(\left(k_F^n\right)^3+2\left(k_F^p\right)^3\right)\\&-4\left(q^2+2m_\pi^2\right)\tilde{\Gamma}_0(p)-2q^2\tilde{\Gamma}_1(p)+\left(q^2+2m_\pi^2\right)^2\cdot\tilde{G}_0(p,q)\\&+2i(\vec{q}\times\vec{p})\cdot\vec{\sigma}_2\left[2\tilde{\Gamma}_0(p)+2\tilde{\Gamma}_1(p)-\left(q^2+2m_\pi^2\right)\left(\tilde{G}_0(p,q)+2\tilde{G}_0(p,q)\right)\right]\Bigg)\end{aligned} \tag{B.10}$$

One-pion-exchange:

$$\frac{C g_A}{18 f_0^2 \pi^2 \Delta}(H_1+3H_2)\left(\frac{2}{3}\left(\left(k_F^n\right)^3+2\left(k_F^p\right)^3\right)-m_\pi^2\tilde{\Gamma}_0(p)\right) \tag{B.11}$$

Contact term:

$$\frac{\rho_n+2\rho_p}{18\Delta}\left(H_1+3H_2\right)^2 \tag{B.12}$$

B.1.2 $\Lambda p \to \Lambda p$

$$V_{\Lambda p\to\Lambda p}=V_{\Lambda n\to\Lambda n}\Big|_{k_n\leftrightarrow k_p} \tag{B.13}$$

B.2 $\Lambda N \to \Sigma N$

B.2.1 $\Lambda n \to \Sigma^0 n$

topology 1

$$\frac{8C^2 D g_A}{9\sqrt{3} f_0^4 \Delta}\, q^2\, \frac{(\vec{\sigma}_1 \cdot \vec{q})\,(\vec{\sigma}_2 \cdot \vec{q})}{(q^2+m_\pi^2)^2}(\rho_n + \rho_p) \tag{B.14}$$

topology 2

$$-\frac{2C^2 D g_A}{9\sqrt{3} f_0^4 \pi^2 \Delta}\frac{(\vec{\sigma}_1 \cdot \vec{q})\,(\vec{\sigma}_2 \cdot \vec{q})}{q^2+m_\pi^2}\left(2\Gamma_5(p,k_F^n) - \Gamma_5(p,k_F^p) + \Gamma^p(p)\right)$$

topology 3

$$\begin{aligned}\frac{C^2 g_A^2}{12\sqrt{3} f_0^4 \pi^2 \Delta}\Bigg(&\left((\vec{\sigma}_1 \cdot \vec{q})\,(\vec{\sigma}_2 \cdot \vec{q}) - q^2 \vec{\sigma}_1 \cdot \vec{\sigma}_2\right) G_2(p,q,k_F^p) \\ &- \vec{\sigma}_1 \cdot (\vec{q}\times\vec{k})\,\vec{\sigma}_2 \cdot (\vec{q}\times\vec{k})\,\hat{G}(p,q,k_F^p) + \frac{i}{2}(\vec{q}\times\vec{p})\cdot\vec{\sigma}_1\,\gamma(p,q,k_F^p)\Bigg)\end{aligned} \tag{B.15}$$

topology 4

$$\frac{2C g_A H_2}{3\sqrt{3} f_0^2 \Delta}\,\frac{(\vec{\sigma}_1 \cdot \vec{q})\,(\vec{\sigma}_2 \cdot \vec{q})}{q^2+m_\pi^2}\,(\rho_n + \rho_p) \tag{B.16}$$

topology 5

$$\begin{aligned}\frac{C g_A}{144\sqrt{3}\pi^2 \Delta f_0^2}\Bigg(&12(H_1 - H_2)\Gamma^n(p) \\ &+ \vec{\sigma}_1 \cdot \vec{\sigma}_2\Big[-48 H_2 \Gamma_2\,(p,k_F^n) \\ &\qquad - 16(H_1+3H_2)(\Gamma^p(p) - \Gamma_2\left(p,k_F^p\right))\Big] \\ &+ \left(\vec{\sigma}_1 \cdot \vec{p}\,'\right)\left(\vec{\sigma}_2 \cdot \vec{p}\,'\right)\left[24(H_1+2H_2)\Gamma_4\left(p,k_F^p\right) - (5H_1+39H_2)\Gamma_4\,(p,k_F^n)\right] \\ &+ (\vec{\sigma}_1 \cdot \vec{p})\,(\vec{\sigma}_2 \cdot \vec{p})\left[(5H_1 - 9H_2)\Gamma_4\,(p,k_F^n) - 8H_1\Gamma_4\left(p,k_F^p\right)\right]\Bigg)\end{aligned} \tag{B.17}$$

topology 6

$$\frac{\rho_n}{6\sqrt{3}\Delta}(H_1 + 2H_1H_2 - 3H_2^2) - \vec{\sigma}_1 \cdot \vec{\sigma}_2 \frac{\rho_p}{9\sqrt{3}\Delta}(H_1^2 + 4H_1H_2 + 3H_2^2) \tag{B.18}$$

B.2.2 $\Lambda p \to \Sigma^0 p$

$$V_{\Lambda p \to \Sigma^0 p} = -V_{\Lambda n \to \Sigma^0 n}\Big|_{k_F^n \leftrightarrow k_F^p} \tag{B.19}$$

B.2.3 $\Lambda n \to \Sigma^- p$

topology 1

$$-\sqrt{\frac{2}{3}}\,\frac{8C^2Dg_A}{9\Delta f_0^4}\,q^2\,\frac{\vec{\sigma}_1\cdot\vec{\sigma}_2}{(m_\pi^2+q^2)^{\,2}}\;(\rho_n+\rho_p) \tag{B.20}$$

topology 2

$$\sqrt{\frac{2}{3}}\,\frac{C^2Dg_A}{9\pi^2\Delta f_0^4}\frac{(\vec{\sigma}_1\cdot\vec{q})\,(\vec{\sigma}_2\cdot\vec{q})}{m_\pi^2+q^2}\left(\Gamma^n(p)+\Gamma^p(p)+3\Gamma_5(p,k_F^n)-\Gamma_5(p,k_F^p)\right)$$

topology 3

$$\begin{aligned}-\sqrt{\frac{2}{3}}\,\frac{C^2g_A^2}{24\pi^2\Delta f_0^4}\Big(&-\vec{\sigma}_1\cdot(\vec{q}\times\vec{k})\,\vec{\sigma}_2\cdot(\vec{q}\times\vec{k})\left[\hat{G}\left(p,q,k_F^n\right)+\hat{G}\left(p,q,k_F^p\right)\right]\\&+\left((\vec{\sigma}_1\cdot\vec{q})\,(\vec{\sigma}_2\cdot\vec{q})-q^2\vec{\sigma}_1\cdot\vec{\sigma}_2\right)\left[G_2\left(p,q,k_F^n\right)+G_2\left(p,q,k_F^p\right)\right]\\&+\frac{i}{2}(\vec{q}\times\vec{p})\cdot\vec{\sigma}_1\left[\gamma\left(p,q,k_F^n\right)+\gamma\left(p,q,k_F^p\right)\right]\Big)\end{aligned} \tag{B.21}$$

topology 4

$$\sqrt{\frac{2}{3}}\,\frac{Cg_A}{9\Delta f_0^2}\frac{(\vec{\sigma}_1\cdot\vec{q})\,(\vec{\sigma}_2\cdot\vec{q})}{m_\pi^2+q^2}\left(2H_1\left(\rho_n-\rho_p\right)-3H_2\left(\rho_n+3\rho_p\right)\right) \tag{B.22}$$

topology 5

$$\begin{aligned}\sqrt{\frac{2}{3}}\,\frac{Cg_A}{432\pi^2\Delta f_0^2}\Big(&-18(H_1-H_2)\left[\Gamma^n(p)+\Gamma^p(p)\right]\\&+3\vec{\sigma}_1\cdot\vec{\sigma}_2\Big[3(H_1+3H_2)\Gamma^n(p)+13(H_1+3H_2)\Gamma^p(p)\\&\qquad-3(H_1-5H_2)\Gamma_2\left(p,k_F^n\right)-(13H_1+15H_2)\Gamma_2\left(p,k_F^p\right)\Big]\\&+\left(\vec{\sigma}_1\cdot\vec{p}\,'\right)\left(\vec{\sigma}_2\cdot\vec{p}\,'\right)\left[-3(7H_1-15H_2)\Gamma_4\left(p,k_F^n\right)-36(H_1+2H_2)\Gamma_4\left(p,k_F^p\right)\right]\\&+(\vec{\sigma}_1\cdot\vec{p})\,(\vec{\sigma}_2\cdot\vec{p})\left[12H_1\Gamma_4\left(p,k_F^n\right)-3(H_1-9H_2)\Gamma_4\left(p,k_F^p\right)\right]\Big)\end{aligned}$$

topology 6

$$\begin{aligned}&-\sqrt{\frac{2}{3}}\,\frac{\rho_n+\rho_p}{12\Delta}\;\left[H_1^2+2H_2H_1-3H_2^2\right]\\&+\sqrt{\frac{2}{3}}\,\frac{1}{36\Delta}\,\vec{\sigma}_1\cdot\vec{\sigma}_2\;\left[(3H_1^2+10H_2H_1+3H_2^2)\rho_n+(H_1+3H_2)^2\rho_p\right]\end{aligned} \tag{B.23}$$

B.2.4 $\Lambda p \to \Sigma^+ n$

$$=\left(\Lambda n\to\Sigma^- p\right)\Big|_{k_F^n\leftrightarrow k_F^p} \tag{B.24}$$

B.3 $\Sigma N \to \Sigma N$ (I=3/2)

B.3.1 $\Sigma^+ p \to \Sigma^+ p$

topology 1

$$-\frac{8C^2 F g_A}{9\Delta f_0^4}\, q^2\, \frac{(\vec{\sigma}_1\cdot\vec{q})\,(\vec{\sigma}_2\cdot\vec{q})}{(m_\pi^2+q^2)^2}\,(\rho_n+\rho_p) \tag{B.25}$$

topology 2

$$\frac{2C^2 g_A F}{9\pi^2\Delta f_0^4}\,\frac{(\vec{\sigma}_1\cdot\vec{q})\,(\vec{\sigma}_2\cdot\vec{q})}{m_\pi^2+q^2}\left(2\Gamma_5(p,k_F^p)-\Gamma_5(p,k_F^n)+\Gamma^n(p)\right)$$

topology 3

$$\begin{aligned}\frac{C^2 g_A^2}{72\pi^2\Delta f_0^4}\Bigg(&\left((\vec{\sigma}_1\cdot\vec{q})\,(\vec{\sigma}_2\cdot\vec{q})-q^2\vec{\sigma}_1\cdot\vec{\sigma}_2\right)G_2\,(p,q,k_F^n)\\ &-\vec{\sigma}_1\cdot(\vec{q}\times\vec{k})\,\vec{\sigma}_2\cdot(\vec{q}\times\vec{k})\hat{G}\,(p,q,k_F^n)+\frac{1}{2}\left(\kappa\,(p,k_F^n)+\kappa\left(p,k_F^p\right)\right)\\ &+\frac{i}{2}(\vec{q}\times\vec{p})\cdot\vec{\sigma}_1\gamma\,(p,q,k_F^n)+i(\vec{q}\times\vec{p})\cdot\vec{\sigma}_2\left(\gamma\,(p,q,k_F^n)+\gamma\left(p,q,k_F^p\right)\right)\Bigg)\end{aligned} \tag{B.26}$$

topology 4

$$-\frac{4Cg_A}{9\Delta f_0^2}\,\frac{(\vec{\sigma}_1\cdot\vec{q})\,(\vec{\sigma}_2\cdot\vec{q})}{m_\pi^2+q^2}\left(H_1\,(\rho_n+\rho_p)+H_2\rho_n\right) \tag{B.27}$$

topology 5

$$\begin{aligned}\frac{Cg_A}{216\pi^2\Delta f_0^2}\Bigg(&12(H_1+H_2)\Gamma^n(p)+24H_1\Gamma^p(p)\\ &+6\,\vec{\sigma}_1\cdot\vec{\sigma}_2\Big[+(3H_1+H_2)\Gamma^n(p)\\ &\qquad+8H_1\Gamma_2\left(p,k_F^p\right)-3(H_1-H_2)\Gamma_2\,(p,k_F^n)\Big]\\ &+3\left(\left(\vec{\sigma}_1\cdot\vec{p}\,'\right)\left(\vec{\sigma}_2\cdot\vec{p}\,'\right)+(\vec{\sigma}_1\cdot\vec{p})\,(\vec{\sigma}_2\cdot\vec{p})\right)\times\\ &\qquad\Big[8H_1\Gamma_4\left(p,k_F^p\right)-3(H_1-H_2)\Gamma_4\,(p,k_F^n)\Big]\Bigg)\end{aligned} \tag{B.28}$$

topology 6

$$\begin{aligned}&-\frac{\rho_n}{18\Delta}\,\vec{\sigma}_1\cdot\vec{\sigma}_2\,(H_1+H_2)^2+\\ &\frac{1}{18\Delta}\left[3(H_1+H_2)^2\rho_n+12H_1^2\rho_p\right]\end{aligned} \tag{B.29}$$

B.3.2 $\Sigma^- n \to \Sigma^- n$

$$V_{\Sigma^- n\to\Sigma^- n}=V_{\Sigma^+ p\to\Sigma^+ p}\Big|_{k_F^n\leftrightarrow k_F^p} \tag{B.30}$$

B.3.3 $\Sigma^+ n \to \Sigma^+ n$

topology 1

$$\frac{8C^2 F g_A}{9\Delta f_0^4}\, q^2\, \frac{(\vec{\sigma}_1\cdot\vec{q})\,(\vec{\sigma}_2\cdot\vec{q})}{\left(m_\pi^2+q^2\right)^2}\,(\rho_n+\rho_p) \tag{B.31}$$

topology 2

$$-\frac{2C^2 F g_A}{9\pi^2\Delta f_0^4}\frac{(\vec{\sigma}_1\cdot\vec{q})\,(\vec{\sigma}_2\cdot\vec{q})}{(m_\pi^2+q^2)}\left(2\Gamma_5(p,k_F^n)-\Gamma_5(p,k_F^p)+\Gamma^p(p)\right)$$

topology 3

$$\begin{aligned}\frac{C^2 g_A^2}{72\pi^2\Delta f_0^4}\Bigg(&\left(q^2\vec{\sigma}_1\cdot\vec{\sigma}_2-(\vec{\sigma}_1\cdot\vec{q})\,(\vec{\sigma}_2\cdot\vec{q})\right)G_2\left(p,q,k_F^p\right)\\ &+\vec{\sigma}_1\cdot(\vec{q}\times\vec{k})\,\vec{\sigma}_2\cdot(\vec{q}\times\vec{k})\hat{G}\left(p,q,k_F^p\right)+\frac{1}{2}\left(\kappa\left(p,k_F^n\right)+\kappa\left(p,k_F^p\right)\right)\\ &-\frac{i}{2}(\vec{q}\times\vec{p})\cdot\vec{\sigma}_1\gamma\left(p,q,k_F^p\right)+i(\vec{q}\times\vec{p})\cdot\vec{\sigma}_2\left(\gamma\left(p,q,k_F^n\right)+\gamma\left(p,q,k_F^p\right)\right)\Bigg)\end{aligned} \tag{B.32}$$

topology 4

$$\frac{4C g_A}{9\Delta f_0^2}\frac{(\vec{\sigma}_1\cdot\vec{q})\,(\vec{\sigma}_2\cdot\vec{q})}{m_\pi^2+q^2}\left(H_1\left(\rho_n+\rho_p\right)+H_2\rho_n\right) \tag{B.33}$$

topology 5

$$\begin{aligned}\frac{C g_A}{216\pi^2\Delta f_0^2}\Bigg(&12(H_1+H_2)\Gamma^p(p)+24H_2\Gamma^n(p)\\ &+6\,\vec{\sigma}_1\cdot\vec{\sigma}_2\Big[-(3H_1+H_2)\Gamma^p(p)\\ &\qquad-8(H_1+H_2)\Gamma_2\left(p,k_F^n\right)+(3H_1+5H_2)\Gamma_2\left(p,k_F^p\right)\Big]\\ &+3\left((\vec{\sigma}_1\cdot\vec{p})\,(\vec{\sigma}_2\cdot\vec{p})+\left(\vec{\sigma}_1\cdot\vec{p}\,'\right)\left(\vec{\sigma}_2\cdot\vec{p}\,'\right)\right)\cdot\\ &\qquad\left[-8(H_1+H_2)\Gamma_4\left(p,k_F^n\right)+(3H_1+5H_2)\Gamma_4\left(p,k_F^p\right)\right]\Bigg)\end{aligned}$$

topology 6

$$\begin{aligned}\frac{1}{18\Delta}\Bigg(&12H_2^2\rho_n+3(H_1+H_2)^2\rho_p\\ &+\ \vec{\sigma}_1\cdot\vec{\sigma}_2\ \left(H_1+H_2\right)^2\rho_p\Bigg)\end{aligned} \tag{B.34}$$

B.3.4 $\Sigma^- p \to \Sigma^- p$

$$V_{\Sigma^- p\to\Sigma^- p}=V_{\Sigma^+ n\to\Sigma^+ n}\Big|_{k_F^n\leftrightarrow k_F^p} \tag{B.35}$$

B.3.5 $\Sigma^0 p \to \Sigma^0 p$

topology 1

$$0 \tag{B.36}$$

topology 2

$$0 \tag{B.37}$$

topology 3

$$\frac{C^2 g_A^2}{72\pi^2 \Delta f_0^4} \left(\kappa\left(p, k_F^n\right) + 2i(\vec{q} \times \vec{p}) \cdot \vec{\sigma}_2 \gamma\left(p, q, k_F^n\right)\right) \tag{B.38}$$

topology 4

$$\frac{4CH_2 g_A}{9\Delta f_0^2} \frac{\left(\vec{\sigma}_1 \cdot \vec{q}\right)\left(\vec{\sigma}_2 \cdot \vec{q}\right)}{m_\pi^2 + q^2} \left(\rho_n - \rho_p\right) \tag{B.39}$$

topology 5

$$\begin{aligned} \frac{Cg_A}{9\pi^2 \Delta f_0^2} \Bigg(& (H_1 + H_2)\Gamma^n(p) \\ & - H_2 \left(\left(\vec{\sigma}_1 \cdot \vec{p}\right)\left(\vec{\sigma}_2 \cdot \vec{p}\right) + \left(\vec{\sigma}_1 \cdot \vec{p}\,'\right)\left(\vec{\sigma}_2 \cdot \vec{p}\,'\right)\right)\left[\Gamma_4\left(p, k_F^n\right) - \Gamma_4\left(p, k_F^p\right)\right] \\ & - 2H_2\, \vec{\sigma}_1 \cdot \vec{\sigma}_2 \left[\Gamma_2\left(p, k_F^n\right) - \Gamma_2\left(p, k_F^p\right)\right] \Bigg) \end{aligned} \tag{B.40}$$

topology 6

$$\frac{1}{6\Delta}\left(2(H_1 + H_2)^2 \rho_n + (H_1 - H_2)^2 \rho_p\right) \tag{B.41}$$

B.3.6 $\Sigma^0 n \to \Sigma^0 n$

$$V_{\Sigma^0 n \to \Sigma^0 n} = V_{\Sigma^0 p \to \Sigma^0 p}\Big|_{k_F^n \leftrightarrow k_F^p} \tag{B.42}$$

B.4 $\Sigma N \to \Sigma N$ (I=I/2)

B.4.1 $\Sigma^0 n \to \Sigma^- p$

topology 1

$$-\frac{8\sqrt{2}C^2 F g_A}{9\Delta f_0^4}\, q^2\, \frac{(\vec{\sigma}_1\cdot\vec{q})\,(\vec{\sigma}_2\cdot\vec{q})}{\left(m_\pi^2+q^2\right)^2}\,(\rho_n+\rho_p) \tag{B.43}$$

topology 2

$$\frac{\sqrt{2}C^2 F g_A}{9\pi^2\Delta f_0^4}\,\frac{(\vec{\sigma}_1\cdot\vec{q})\,(\vec{\sigma}_2\cdot\vec{q})}{m_\pi^2+q^2}\left(3\Gamma_5(p,k_F^n)-\Gamma_5(p,k_F^p)+\Gamma^n(p)+\Gamma^p(p)\right)$$

topology 3

$$\begin{aligned}\frac{\sqrt{2}C^2 g_A^2}{144\pi^2\Delta f_0^4}\Big(&\frac{1}{2}\left[\kappa\left(p,k_F^n\right)-\kappa\left(p,k_F^p\right)\right]\\ &\left((\vec{\sigma}_1\cdot\vec{q})\,(\vec{\sigma}_2\cdot\vec{q})-q^2\vec{\sigma}_1\cdot\vec{\sigma}_2\right)\left[G_2\left(p,q,k_F^n\right)+G_2\left(p,q,k_F^p\right)\right]\\ &-\vec{\sigma}_1\cdot(\vec{q}\times\vec{k})\,\vec{\sigma}_2\cdot(\vec{q}\times\vec{k})\left[\hat{G}\left(p,q,k_F^p\right)+\hat{G}\left(p,q,k_F^n\right)\right]\\ &+\frac{i}{2}(\vec{q}\times\vec{p})\cdot\vec{\sigma}_1\left[\gamma\left(p,q,k_F^n\right)+\gamma\left(p,q,k_F^p\right)\right]\\ &+i(\vec{q}\times\vec{p})\cdot\vec{\sigma}_2\left[\gamma\left(p,q,k_F^n\right)-\gamma\left(p,q,k_F^p\right)\right]\Big)\end{aligned} \tag{B.44}$$

topology 4

$$-\frac{\sqrt{2}C g_A}{9\Delta f_0^2}\,\frac{(\vec{\sigma}_1\cdot\vec{q})\,(\vec{\sigma}_2\cdot\vec{q})}{m_\pi^2+q^2}\left((4H_1-H_2)\rho_n+(4H_1+5H_2)\rho_p\right) \tag{B.45}$$

topology 5

$$\begin{aligned}\frac{\sqrt{2}C g_A}{72\pi^2\Delta f_0^2}\Big(&4H_1\Gamma^n(p)-4H_2\Gamma^p(p)\\ &+\vec{\sigma}_1\cdot\vec{\sigma}_2\Big[(3H_1+H_2)\left(\Gamma^n(p)+\Gamma^p(p)\right)\\ &\qquad+(5H_1-9H_2)\Gamma_2\left(p,k_F^n\right)+5(H_1+3H_2)\Gamma_2\left(p,k_F^p\right)\Big]\\ &+\left(\vec{\sigma}_1\cdot\vec{p}\,'\right)\left(\vec{\sigma}_2\cdot\vec{p}\,'\right)\left[3(13H_1-5H_2)\Gamma_4\left(p,k_F^n\right)-3(3H_1-11H_2)\Gamma_4\left(p,k_F^p\right)\right]\\ &+(\vec{\sigma}_1\cdot\vec{p})\,(\vec{\sigma}_2\cdot\vec{p})\left[-3(3H_1+13H_2)\Gamma_4\left(p,k_F^n\right)+3(13H_1+19H_2)\Gamma_4\left(p,k_F^p\right)\right]\Big)\end{aligned} \tag{B.46}$$

topology 6

$$\begin{aligned}\frac{\sqrt{2}}{36\Delta}\Big(&(9H_1^2+6H_1H_2-3H_2^2)\rho_n+(3H_1^2-6H_1H_2-9H_2^2)\rho_p\\ &-\vec{\sigma}_1\cdot\vec{\sigma}_2(H_1+H_2)^2(\rho_n+\rho_p)\Big)\end{aligned} \tag{B.47}$$

B.4.2 $\Sigma^0 p \to \Sigma^+ n$

$$V_{\Sigma^0 p\to\Sigma^+ n} = -V_{\Sigma^0 n\to\Sigma^- p}\Big|_{k_F^n\leftrightarrow k_F^p} \tag{B.48}$$

BIBLIOGRAPHY

[1] Dominik Gerstung, Norbert Kaiser, and Wolfram Weise. "Hyperon-nucleon three-body forces and strangeness in neutron stars." In: (Jan. 2020). arXiv: 2001.10563 [nucl-th].

[2] Paul Demorest, Tim Pennucci, Scott Ransom, Mallory Roberts, and Jason Hessels. "Shapiro Delay Measurement of A Two Solar Mass Neutron Star." In: *Nature* 467 (2010), pp. 1081–1083. DOI: 10.1038/nature09466. arXiv: 1010.5788 [astro-ph.HE].

[3] John Antoniadis et al. "A Massive Pulsar in a Compact Relativistic Binary." In: *Science* 340 (2013), p. 6131. DOI: 10.1126/science.1233232. arXiv: 1304.6875 [astro-ph.HE].

[4] H. Thankful Cromartie et al. "A very massive neutron star: relativistic Shapiro delay measurements of PSR J0740+6620." In: (2019). arXiv: 1904.06759 [astro-ph.HE].

[5] V. A. Ambartsumyan and G. S. Saakyan. "The Degenerate Superdense Gas of Elementary Particles." In: *Soviet Astronomy* 4 (Oct. 1960), p. 187.

[6] A. Gal, E. V. Hungerford, and D. J. Millener. "Strangeness in nuclear physics." In: *Rev. Mod. Phys.* 88.3 (2016), p. 035004. DOI: 10.1103/RevModPhys.88.035004. arXiv: 1605.00557 [nucl-th].

[7] Diego Lonardoni, Alessandro Lovato, Stefano Gandolfi, and Francesco Pederiva. "Hyperon Puzzle: Hints from Quantum Monte Carlo Calculations." In: *Phys. Rev. Lett.* 114.9 (2015), p. 092301. DOI: 10.1103/PhysRevLett.114.092301. arXiv: 1407.4448 [nucl-th].

[8] É. Massot, J. Margueron, and G. Chanfray. "On the maximum mass of hyperonic neutron stars." In: *EPL (Europhysics Letters)* 97.3 (2012), p. 39002. DOI: 10.1209/0295-5075/97/39002. URL: https://doi.org/10.1209%2F0295-5075%2F97%2F39002.

[9] H. Đapo, B.-J. Schaefer, and J. Wambach. "Appearance of hyperons in neutron stars." In: *Phys. Rev. C* 81 (3 2010), p. 035803. DOI: 10.1103/PhysRevC.81.035803. URL: https://link.aps.org/doi/10.1103/PhysRevC.81.035803.

[10] H.-J. Schulze and T. Rijken. "Maximum mass of hyperon stars with the Nijmegen ESC08 model." In: *Phys. Rev. C* 84 (3 2011), p. 035801. DOI: 10.1103/PhysRevC.84.035801. URL: https://link.aps.org/doi/10.1103/PhysRevC.84.035801.

[11] I. Vidaña, D. Logoteta, C. Providência, A. Polls, and I. Bombaci. "Estimation of the effect of hyperonic three-body forces on the maximum mass of neutron stars." In: *EPL (Europhysics Letters)* 94.1 (2011), p. 11002. DOI: 10.1209/0295-5075/94/11002. URL: https://doi.org/10.1209%2F0295-5075%2F94%2F11002.

[12] Ignazio Bombaci and Domenico Logoteta. "Neutron stars: Cosmic laboratories for matter under extreme conditions." In: *EPJ Web Conf.* 117 (2016). Ed. by V. Greco, M. La Cognata, S. Pirrone, F. Rizzo, and C. Spitaleri, p. 07005. DOI: 10.1051/epjconf/201611707005.

[13] J. N. Hu, A. Li, H. Toki, and W. Zuo. "Extended quark mean-field model for neutron stars." In: *Phys. Rev. C* 89 (2 2014), p. 025802. DOI: 10.1103/PhysRevC.89.025802. URL: https://link.aps.org/doi/10.1103/PhysRevC.89.025802.

[14] Tsuyoshi Miyatsu, Myung-Ki Cheoun, and Koichi Saito. "Equation of state for neutron stars in SU(3) flavor symmetry." In: *Phys. Rev. C* 88 (1 2013), p. 015802. DOI: 10.1103/PhysRevC.88.015802. URL: https://link.aps.org/doi/10.1103/PhysRevC.88.015802.

[15] Tsuyoshi Miyatsu, Sachiko Yamamuro, and Ken'ichiro Nakazato. "A NEW EQUATION OF STATE FOR NEUTRON STAR MATTER WITH NUCLEI IN THE CRUST AND HYPERONS IN THE CORE." In: *The Astrophysical Journal* 777.1 (2013), p. 4. DOI: 10.1088/0004-637x/777/1/4. URL: https://doi.org/10.1088%2F0004-637x%2F777%2F1%2F4.

[16] Neha Gupta and P. Arumugam. "Impact of hyperons and antikaons in an extended relativistic mean-field description of neutron stars." In: *Phys. Rev. C* 88 (1 2013), p. 015803. DOI: 10.1103/PhysRevC.88.015803. URL: https://link.aps.org/doi/10.1103/PhysRevC.88.015803.

[17] Ritam Mallick. "Maximum mass of a hybrid star having a mixed-phase region based on constraints set by the pulsar PSR J1614-2230." In: *Phys. Rev. C* 87 (2 2013), p. 025804. DOI: 10.1103/PhysRevC.87.025804. URL: https://link.aps.org/doi/10.1103/PhysRevC.87.025804.

[18] Bednarek, I., Haensel, P., Zdunik, J. L., Bejger, M., and Ma´nka, R. "Hyperons in neutron-star cores and a 2lsar." In: *A&A* 543 (2012), A157. DOI: 10.1051/0004-6361/201118560. URL: https://doi.org/10.1051/0004-6361/201118560.

[19] S. Weissenborn, D. Chatterjee, and J. Schaffner-Bielich. "Hyperons and massive neutron stars: Vector repulsion and SU(3) symmetry." In: *Phys. Rev. C* 85 (6 2012), p. 065802. DOI: 10.1103/PhysRevC.85.065802. URL: https://link.aps.org/doi/10.1103/PhysRevC.85.065802.

[20] Wei-Zhou Jiang, Bao-An Li, and Lie-Wen Chen. "LARGE-MASS NEUTRON STARS WITH HYPERONIZATION." In: *The Astrophysical Journal* 756.1 (2012), p. 56. DOI: 10.1088/0004-637x/756/1/56. URL: https://doi.org/10.1088%2F0004-637x%2F756%2F1%2F56.

[21] A. Sulaksono and B.K. Agrawal. "Existence of hyperons in the pulsar PSRJ1614-2230." In: *Nuclear Physics A* 895 (2012), pp. 44 –58. ISSN: 0375-9474. DOI: https://doi.org/10.1016/j.nuclphysa.2012.09.006. URL: http://www.sciencedirect.com/science/article/pii/S0375947412002679.

[22] Luiz L. Lopes and Debora P. Menezes. "Hypernuclear matter in a complete SU(3) symmetry group." In: *Phys. Rev. C* 89 (2 2014), p. 025805. DOI: 10.1103/PhysRevC.89.025805. URL: https://link.aps.org/doi/10.1103/PhysRevC.89.025805.

[23] V.G.J. Stoks, R.A.M. Klomp, C.P.F. Terheggen, and J.J. de Swart. "Construction of high quality N N potential models." In: *Phys. Rev. C* 49 (1994), pp. 2950–2962. DOI: 10.1103/PhysRevC.49.2950. arXiv: nucl-th/9406039.

[24] Robert B. Wiringa, V.G.J. Stoks, and R. Schiavilla. "An Accurate nucleon-nucleon potential with charge independence breaking." In: *Phys. Rev. C* 51 (1995), pp. 38–51. DOI: 10.1103/PhysRevC.51.38. arXiv: nucl-th/9408016.

[25] R. Machleidt. "The High precision, charge dependent Bonn nucleon-nucleon potential (CD-Bonn)." In: *Phys. Rev. C* 63 (2001), p. 024001. DOI: 10.1103/PhysRevC.63.024001. arXiv: nucl-th/0006014.

[26] Bruce H.J. McKellar and R. Rajaraman. "Three-Body Forces in Nuclear Matter." In: *Phys. Rev. Lett.* 21 (1968), pp. 450–453. DOI: 10.1103/PhysRevLett.21.450.

[27] Sidney A. Coon, Michael D. Scadron, and Bruce R. Barrett. "The Three-Body Force, Off-Shell Pion Nucleon Scattering, and Binding Energies in Nuclear Matter." In: *Nucl. Phys. A* 242 (1975). [Erratum: Nucl.Phys.A 254, 542–543 (1975)], pp. 467–480. DOI: 10.1016/0375-9474(75)90235-3.

[28] H.T. Coelho, T.K. Das, and M.R. Robilotta. "TWO PION EXCHANGE THREE NUCLEON FORCE AND THE H-3 AND HE-3 NUCLEI." In: *Phys. Rev. C* 28 (1983), pp. 1812–1828. DOI: 10.1103/PhysRevC.28.1812.

[29] B.S. Pudliner, V.R. Pandharipande, J. Carlson, Steven C. Pieper, and Robert B. Wiringa. "Quantum Monte Carlo calculations of nuclei with A <= 7." In: *Phys. Rev. C* 56 (1997), pp. 1720–1750. DOI: 10.1103/PhysRevC.56.1720. arXiv: nucl-th/9705009.

[30] Steven C. Pieper, V.R. Pandharipande, Robert B. Wiringa, and J. Carlson. "Realistic models of pion exchange three nucleon interactions." In: *Phys. Rev. C* 64 (2001), p. 014001. DOI: 10.1103/PhysRevC.64.014001. arXiv: nucl-th/0102004.

[31] Evgeny Epelbaum, Hans-Werner Hammer, and Ulf-G. Meissner. "Modern Theory of Nuclear Forces." In: *Rev. Mod. Phys.* 81 (2009), pp. 1773–1825. DOI: 10.1103/RevModPhys.81.1773. arXiv: 0811.1338 [nucl-th].

[32] R. Machleidt and D.R. Entem. "Chiral effective field theory and nuclear forces." In: *Phys. Rept.* 503 (2011), pp. 1–75. DOI: 10.1016/j.physrep.2011.02.001. arXiv: 1105.2919 [nucl-th].

[33] D. R. Entem and R. Machleidt. "Accurate charge dependent nucleon nucleon potential at fourth order of chiral perturbation theory." In: *Phys. Rev.* C68 (2003), p. 041001. DOI: 10.1103/PhysRevC.68.041001. arXiv: nucl-th/0304018 [nucl-th].

[34] D.R. Entem, R. Machleidt, and Y. Nosyk. "High-quality two-nucleon potentials up to fifth order of the chiral expansion." In: *Phys. Rev. C* 96.2 (2017), p. 024004. DOI: 10.1103/PhysRevC.96.024004. arXiv: 1703.05454 [nucl-th].

[35] P. Reinert, H. Krebs, and E. Epelbaum. "Semilocal momentum-space regularized chiral two-nucleon potentials up to fifth order." In: *Eur. Phys. J. A* 54.5 (2018), p. 86. DOI: 10.1140/epja/i2018-12516-4. arXiv: 1711.08821 [nucl-th].

[36] Patrick Reinert, Hermann Krebs, and Evgeny Epelbaum. "High-Precision Nucleon-Nucleon Potentials from Chiral EFT." In: *Springer Proc. Phys.* 238 (2020), pp. 497–501. DOI: 10.1007/978-3-030-32357-8_82.

[37] E. Epelbaum, A. Nogga, Walter Gloeckle, H. Kamada, Ulf G. Meissner, and H. Witala. "Three nucleon forces from chiral effective field theory." In: *Phys. Rev. C* 66 (2002), p. 064001. DOI: 10.1103/PhysRevC.66.064001. arXiv: nucl-th/0208023.

[38] Steven Weinberg. "Nuclear forces from chiral Lagrangians." In: *Phys. Lett.* B251 (1990), pp. 288–292. DOI: 10.1016/0370-2693(90)90938-3.

[39] Steven Weinberg. "Effective chiral Lagrangians for nucleon - pion interactions and nuclear forces." In: *Nucl. Phys.* B363 (1991), pp. 3–18. DOI: 10.1016/0550-3213(91)90231-L.

[40] Steven Weinberg. "Three body interactions among nucleons and pions." In: *Phys. Lett.* B295 (1992), pp. 114–121. DOI: 10.1016/0370-2693(92)90099-P. arXiv: hep-ph/9209257 [hep-ph].

[41] U. van Kolck. "Few nucleon forces from chiral Lagrangians." In: *Phys. Rev. C* 49 (1994), pp. 2932–2941. DOI: 10.1103/PhysRevC.49.2932.

[42] S. Ishikawa and M.R. Robilotta. "Two-pion exchange three-nucleon potential: O(q**4) chiral expansion." In: *Phys. Rev. C* 76 (2007), p. 014006. DOI: 10.1103/PhysRevC.76.014006. arXiv: 0704.0711 [nucl-th].

[43] V. Bernard, E. Epelbaum, H. Krebs, and Ulf-G. Meissner. "Subleading contributions to the chiral three-nucleon force. I. Long-range terms." In: *Phys. Rev. C* 77 (2008), p. 064004. DOI: 10.1103/PhysRevC.77.064004. arXiv: 0712.1967 [nucl-th].

[44] V. Bernard, E. Epelbaum, H. Krebs, and U.-G. Meissner. "Subleading contributions to the chiral three-nucleon force II: Short-range terms and relativistic corrections." In: *Phys. Rev. C* 84 (2011), p. 054001. DOI: 10.1103/PhysRevC.84.054001. arXiv: 1108.3816 [nucl-th].

[45] Hermann Krebs, A. Gasparyan, and Evgeny Epelbaum. "Chiral three-nucleon force at N^4LO I: Longest-range contributions." In: *Phys. Rev. C* 85 (2012), p. 054006. DOI: 10.1103/PhysRevC.85.054006. arXiv: 1203.0067 [nucl-th].

[46] Hermann Krebs, A. Gasparyan, and Evgeny Epelbaum. "Chiral three-nucleon force at N^4LO II: Intermediate-range contributions." In: *Phys. Rev. C* 87.5 (2013), p. 054007. DOI: 10.1103/PhysRevC.87.054007. arXiv: 1302.2872 [nucl-th].

[47] Steven C. Pieper and Robert B. Wiringa. "Quantum Monte Carlo calculations of light nuclei." In: *Ann. Rev. Nucl. Part. Sci.* 51 (2001), pp. 53–90. DOI: 10.1146/annurev.nucl.51.101701.132506. arXiv: nucl-th/0103005.

[48] R. Engelmann, H. Filthuth, V. Hepp, and E. Kluge. "Inelastic Σ^-p-interactions at low momenta." In: *Physics Letters* 21.5 (1966), pp. 587 –589. ISSN: 0031-9163. DOI: https://doi.org/10.1016/0031-9163(66)91310-2. URL: http://www.sciencedirect.com/science/article/pii/0031916366913102.

[49] G. Alexander, U. Karshon, A. Shapira, G. Yekutieli, R. Engelmann, H. Filthuth, and W. Lughofer. "Study of the lambda-n system in low-energy lambda-p elastic scattering." In: *Phys. Rev.* 173 (1968), pp. 1452–1460. DOI: 10.1103/PhysRev.173.1452.

[50] B. Sechi-Zorn, B. Kehoe, J. Twitty, and R.A. Burnstein. "Low-energy lambda-proton elastic scattering." In: *Phys. Rev.* 175 (1968), pp. 1735–1740. DOI: 10.1103/PhysRev.175.1735.

[51] J. Haidenbauer, S. Petschauer, N. Kaiser, U. G. Meissner, A. Nogga, and W. Weise. "Hyperon-nucleon interaction at next-to-leading order in chiral effective field theory." In: *Nucl. Phys.* A915 (2013), pp. 24–58. DOI: 10.1016/j.nuclphysa.2013.06.008. arXiv: 1304.5339 [nucl-th].

[52] Stefan Petschauer, Norbert Kaiser, Johann Haidenbauer, Ulf-G. Meißner, and Wolfram Weise. "Leading three-baryon forces from SU(3) chiral effective field theory." In: *Phys. Rev.* C93.1 (2016), p. 014001. DOI: 10.1103/PhysRevC.93.014001. arXiv: 1511.02095 [nucl-th].

[53] R.K. Bhaduri, B.A. Loiseau, and Y. Nogami. "Effect of three-body ΛNN long-range potential in nuclear matter." In: *Nucl. Phys. B* 3 (1967), pp. 380–386. DOI: 10.1016/0550-3213(67)90007-7.

[54] R.K Bhaduri, B.A Loiseau, and Y Nogami. "Effects of three-body ΛNN forces in light hypernuclei." In: *Annals of Physics* 44.1 (1967), pp. 57 –73. ISSN: 0003-4916. DOI: https://doi.org/10.1016/0003-4916(67)90264-3. URL: http://www.sciencedirect.com/science/article/pii/0003491667902643.

[55] A. Gal, J.M. Soper, and R.H. Dalitz. "Shell-model analysis of lambda binding energies for p-shell hypernuclei. 1. Basic formulas and matrix elements for lambda N and lambda NN forces." In: *Annals Phys.* 63 (1971), pp. 53–126. DOI: 10.1016/0003-4916(71)90297-1.

[56] A Gal, J.M Soper, and R.H Dalitz. "Shell-model analysis of lambda binding-energies for p-shell hypernuclei. 2. Numerical fitting, interpretation, and hypernuclear predictions." In: *Annals Phys.* 72 (1972), pp. 445–488. DOI: 10.1016/0003-4916(72)90222-9.

[57] A. Gal, J.M. Soper, and R.H. Dalitz. "A Shell Model Analysis of Lambda Binding Energies for the p Shell Hypernuclei. 3. Further Analysis and Predictions." In: *Annals Phys.* 113 (1978), pp. 79–97. DOI: 10.1016/0003-4916(78)90250-6.

[58] A.R. Bodmer and Q.N. Usmani. "Binding Energies of the S Shell Hypernuclei and the Λ Well Depth." In: *Nucl. Phys. A* 477 (1988), pp. 621–651. DOI: 10.1016/0375-9474(88)90410-1.

[59] A.A. Usmani. "The Three baryon Lambda N N potential." In: *Phys. Rev. C* 52 (1995), pp. 1773–1777. DOI: 10.1103/PhysRevC.52.1773. arXiv: nucl-th/9503023.

[60] D. Lonardoni, S. Gandolfi, and F. Pederiva. "Effects of the two-body and three-body hyperon-nucleon interactions in Λ-hypernuclei." In: *Phys. Rev. C* 87 (2013), p. 041303. DOI: 10.1103/PhysRevC.87.041303. arXiv: 1301.7472 [nucl-th].

[61] D. Lonardoni, F. Pederiva, and S. Gandolfi. "Accurate determination of the interaction between Λ hyperons and nucleons from auxiliary field diffusion Monte Carlo calculations." In: *Phys. Rev. C* 89.1 (2014), p. 014314. DOI: 10.1103/PhysRevC.89.014314. arXiv: 1312.3844 [nucl-th].

[62] F. Sammarruca, R. Machleidt, and N. Kaiser. "Spin-polarized neutron-rich matter at different orders of chiral effective field theory." In: *Phys. Rev.* C92.5 (2015), p. 054327. DOI: 10.1103/PhysRevC.92.054327. arXiv: 1505.04836 [nucl-th].

[63] J. W. Holt, N. Kaiser, and W. Weise. "Density-dependent effective nucleon-nucleon interaction from chiral three-nucleon forces." In: *Phys. Rev.* C81 (2010), p. 024002. DOI: 10.1103/PhysRevC.81.024002. arXiv: 0910.1249 [nucl-th].

[64] Stefan Petschauer, Johann Haidenbauer, Norbert Kaiser, Ulf-G. Meißner, and Wolfram Weise. "Density-dependent effective baryon–baryon interaction from chiral three-baryon forces." In: *Nucl. Phys.* A957 (2017), pp. 347–378. DOI: 10.1016/j.nuclphysa.2016.09.010. arXiv: 1607.04307 [nucl-th].

[65] J. Haidenbauer, U. G. Meißner, N. Kaiser, and W. Weise. "Lambda-nuclear interactions and hyperon puzzle in neutron stars." In: *Eur. Phys. J.* A53.6 (2017), p. 121. DOI: 10.1140/epja/i2017-12316-4. arXiv: 1612.03758 [nucl-th].

[66] M. Kohno. "Single-particle potential of the Λ hyperon in nuclear matter with chiral effective field theory NLO interactions including effects of YNN three-baryon interactions." In: *Phys. Rev.* C97.3 (2018), p. 035206. DOI: 10.1103/PhysRevC.97.035206. arXiv: 1802.05388 [nucl-th].

[67] J. Haidenbauer and Ulf-G. Meissner. "The Julich hyperon-nucleon model revisited." In: *Phys. Rev. C* 72 (2005), p. 044005. DOI: 10.1103/PhysRevC.72.044005. arXiv: nucl-th/0506019.

[68] Thomas A. Rijken, M.M. Nagels, and Yasuo Yamamoto. "Baryon-baryon interactions: Nijmegen extended-soft-core models." In: *Prog. Theor. Phys. Suppl.* 185 (2010), pp. 14–71. DOI: 10.1143/PTPS.185.14.

[69] Sinya Aoki, Takumi Doi, Tetsuo Hatsuda, Yoichi Ikeda, Takashi Inoue, Noriyoshi Ishii, Keiko Murano, Hidekatsu Nemura, and Kenji Sasaki. "Lattice QCD approach to Nuclear Physics." In: *PTEP* 2012 (2012), 01A105. DOI: 10.1093/ptep/pts010. arXiv: 1206.5088 [hep-lat].

[70] S.R. Beane, W. Detmold, K. Orginos, and M.J. Savage. "Nuclear Physics from Lattice QCD." In: *Prog.Part.Nucl.Phys.* 66 (2011), pp. 1–40. DOI: 10.1016/j.ppnp.2010.08.002. arXiv: 1004.2935 [hep-lat].

[71] S.R. Beane, E. Chang, S.D. Cohen, W. Detmold, H.-W. Lin, T.C. Luu, K. Orginos, A. Parreno, M.J. Savage, and A. Walker-Loud. "Hyperon-Nucleon Interactions and the Composition of Dense Nuclear Matter from Quantum Chromodynamics." In: *Phys.Rev.Lett.* 109 (2012), p. 172001. DOI: 10.1103/PhysRevLett.109.172001. arXiv: 1204.3606 [hep-lat].

[72] Hidekatsu Nemura et al. "Baryon interactions from lattice QCD with physical masses — strangeness $S = -1$ sector —." In: *Proceedings, 35th International Symposium on Lattice Field Theory (Lattice 2017): Granada, Spain, June 18-24, 2017*. Vol. 175. 2018, p. 05030. DOI: 10.1051/epjconf/201817505030. arXiv: 1711.07003 [hep-lat].

[73] G.'t Hooft. "A planar diagram theory for strong interactions." In: *Nuclear Physics B* 72.3 (1974), pp. 461 –473. ISSN: 0550-3213. DOI: https://doi.org/10.1016/0550-3213(74)90154-0. URL: http://www.sciencedirect.com/science/article/pii/0550321374901540.

[74] Edward Witten. "Baryons in the 1/n Expansion." In: *Nucl. Phys.* B160 (1979), pp. 57–115. DOI: 10.1016/0550-3213(79)90232-3.

[75] Aneesh V. Manohar. *Large N QCD*. 1998. arXiv: hep-ph/9802419 [hep-ph].

[76] S. Scherer. *Introduction to Chiral Perturbation Theory*. 2002. arXiv: hep-ph/0210398 [hep-ph].

[77] C. S. Wu, E. Ambler, R. W. Hayward, D. D. Hoppes, and R. P. Hudson. "Experimental Test of Parity Conservation in Beta Decay." In: *Phys. Rev.* 105 (1957), pp. 1413–1414. DOI: 10.1103/PhysRev.105.1413.

[78] J. H. Christenson, J. W. Cronin, V. L. Fitch, and R. Turlay. "Evidence for the 2π Decay of the K_2^0 Meson." In: *Phys. Rev. Lett.* 13 (1964), pp. 138–140. DOI: 10.1103/PhysRevLett.13.138.

[79] C. A. Baker et al. "An Improved experimental limit on the electric dipole moment of the neutron." In: *Phys. Rev. Lett.* 97 (2006), p. 131801. DOI: 10.1103/PhysRevLett.97.131801. arXiv: hep-ex/0602020 [hep-ex].

[80] Stephen L. Adler. "Axial vector vertex in spinor electrodynamics." In: *Phys.Rev.* 177 (1969), pp. 2426–2438. DOI: 10.1103/PhysRev.177.2426.

[81] J.S. Bell and R. Jackiw. "A PCAC puzzle: $\pi^0 \to \gamma\gamma$ in the σ model." In: *Nuovo Cim.A* 60 (1969), pp. 47–61. DOI: 10.1007/BF02823296.

[82] Stephen L. Adler and William A. Bardeen. "Absence of higher order corrections in the anomalous axial vector divergence equation." In: *Phys.Rev.* 182 (1969), pp. 1517–1536. DOI: 10.1103/PhysRev.182.1517.

[83] J. Goldstone. "Field Theories with Superconductor Solutions." In: *Nuovo Cim.* 19 (1961), pp. 154–164. DOI: 10.1007/BF02812722.

[84] Jeffrey Goldstone, Abdus Salam, and Steven Weinberg. "Broken Symmetries." In: *Phys. Rev.* 127 (1962), pp. 965–970. DOI: 10.1103/PhysRev.127.965.

[85] J. Gasser and H. Leutwyler. "Chiral Perturbation Theory to One Loop." In: *Annals Phys.* 158 (1984), p. 142. DOI: 10.1016/0003-4916(84)90242-2.

[86] Steven Weinberg. "Phenomenological Lagrangians." In: *Physica* A96.1-2 (1979), pp. 327–340. DOI: 10.1016/0378-4371(79)90223-1.

[87] J. Gasser and H. Leutwyler. "Chiral Perturbation Theory: Expansions in the Mass of the Strange Quark." In: *Nucl. Phys.* B250 (1985), pp. 465–516. DOI: 10.1016/0550-3213(85)90492-4.

[88] B. Borasoy. "Baryon axial currents." In: *Phys. Rev. D* 59 (1999), p. 054021. DOI: 10.1103/PhysRevD.59.054021. arXiv: hep-ph/9811411.

[89] A. Krause. "Baryon Matrix Elements of the Vector Current in Chiral Perturbation Theory." In: *Helv. Phys. Acta* 63 (1990), pp. 3–70. DOI: 10.5169/seals-116214.

[90] Jose Antonio Oller, Michela Verbeni, and Joaquim Prades. "Meson-baryon effective chiral lagrangians to O(q**3)." In: *JHEP* 09 (2006), p. 079. DOI: 10.1088/1126-6708/2006/09/079. arXiv: hep-ph/0608204.

[91] Henk Polinder, Johann Haidenbauer, and Ulf-G. Meissner. "Hyperon-nucleon interactions: A Chiral effective field theory approach." In: *Nucl. Phys.* A779 (2006), pp. 244–266. DOI: 10.1016/j.nuclphysa.2006.09.006. arXiv: nucl-th/0605050 [nucl-th].

[92] Stefan Petschauer and Norbert Kaiser. "Relativistic SU(3) chiral baryon-baryon Lagrangian up to order q^2." In: *Nucl. Phys.* A916 (2013), pp. 1–29. DOI: 10.1016/j.nuclphysa.2013.07.010. arXiv: 1305.3427 [nucl-th].

[93] E. Epelbaum, W. Glockle, and Ulf-G. Meissner. "The Two-nucleon system at next-to-next-to-next-to-leading order." In: *Nucl. Phys.* A747 (2005), pp. 362–424. DOI: 10.1016/j.nuclphysa.2004.09.107. arXiv: nucl-th/0405048 [nucl-th].

[94] F. Eisele, H. Filthuth, W. Foehlisch, V. Hepp, and Gunter Zech. "Elastic sigma+- p scattering at low energies." In: *Phys. Lett. B* 37 (1971), pp. 204–206. DOI: 10.1016/0370-2693(71)90053-0.

[95] V. Hepp and H. Schleich. "A New Determination of the Capture Ratio r(c) = Sigma- p –> Sigma0 n / (Sigma- p –> Sigma0 n) + (Sigma- p –> Lambda n), the Lambda0-Lifetime and Sigma- Lambda0 Mass Difference." In: *Z. Phys.* 214 (1968), p. 71. DOI: 10.1007/BF01380085.

[96] J. Haidenbauer, U. G. Meißner, and A. Nogga. "Hyperon-nucleon interaction within chiral effective field theory revisited." In: (2019). arXiv: 1906.11681 [nucl-th].

[97] J. W. Holt, N. Kaiser, and T. R. Whitehead. "Tensor Fermi liquid parameters in nuclear matter from chiral effective field theory." In: *Phys. Rev.* C97.5 (2018), p. 054325. DOI: 10.1103/PhysRevC.97.054325. arXiv: 1712.05013 [nucl-th].

[98] B. D. Day. "Elements of the Brueckner-Goldstone Theory of Nuclear Matter." In: *Rev. Mod. Phys.* 39 (1967), pp. 719–744. DOI: 10.1103/RevModPhys.39.719.

[99] S. Petschauer, J. Haidenbauer, N. Kaiser, Ulf-G. Meißner, and W. Weise. "Hyperons in nuclear matter from SU(3) chiral effective field theory." In: *Eur. Phys. J.* A52.1 (2016), p. 15. DOI: 10.1140/epja/i2016-16015-4. arXiv: 1507.08808 [nucl-th].

[100] J. Goldstone. "Derivation of the Brueckner Many-Body Theory." In: *Proc. Roy. Soc. Lond.* A239 (1957), pp. 267–279. DOI: 10.1098/rspa.1957.0037.

[101] H. A. Bethe, B. H. Brandow, and A. G. Petschek. "Reference Spectrum Method for Nuclear Matter." In: *Phys. Rev.* 129.1 (1963), p. 225. DOI: 10.1103/PhysRev.129.225.

[102] J. P. Jeukenne, A. Lejeune, and C. Mahaux. "Many Body Theory of Nuclear Matter." In: *Phys. Rept.* 25 (1976), pp. 83–174. DOI: 10.1016/0370-1573(76)90017-X.

[103] H.Q. Song, M. Baldo, G. Giansiracusa, and U. Lombardo. "Bethe-Brueckner-Goldstone Expansion in Nuclear Matter." In: *Phys. Rev. Lett.* 81 (1998), pp. 1584–1587. DOI: 10.1103/PhysRevLett.81.1584.

[104] E. Anderson et al. *LAPACK Users' Guide*. Third. Philadelphia, PA: Society for Industrial and Applied Mathematics, 1999. ISBN: 0-89871-447-8 (paperback).

[105] Peter Lepage. *gplepage/vegas: vegas version 3.4*. Version 3.4. Apr. 11, 2019. URL: http://doi.org/10.5281/zenodo.2636746.

[106] A. Akmal, V.R. Pandharipande, and D.G. Ravenhall. "The Equation of state of nucleon matter and neutron star structure." In: *Phys. Rev. C* 58 (1998), pp. 1804–1828. DOI: 10.1103/PhysRevC.58.1804. arXiv: nucl-th/9804027.

[107] Bengt Friman and Wolfram Weise. "Neutron Star Matter as a Relativistic Fermi Liquid." In: *Phys. Rev. C* 100.6 (2020), p. 065807. DOI: 10.1103/PhysRevC.100.065807. arXiv: 1908.09722 [nucl-th].

[108] Felipe Isaule, H. F. Arellano, and Arnau Rios. "Di-neutrons in neutron matter within a Brueckner-Hartree-Fock approach." In: *Phys. Rev.* C94.3 (2016), p. 034004. DOI: 10.1103/PhysRevC.94.034004. arXiv: 1602.05234 [nucl-th].

[109] Eemeli Annala, Tyler Gorda, Aleksi Kurkela, and Aleksi Vuorinen. "Gravitational-Wave Constraints on the Neutron-Star-Matter Equation of State." In: *Phys. Rev. Lett.* 120 (17 2018), p. 172703. DOI: 10.1103/PhysRevLett.120.172703. URL: https://link.aps.org/doi/10.1103/PhysRevLett.120.172703.

[110] T. Motoba, H. Bando, R. Wunsch, and J. Zofka. "Hypernuclear Production by the (π^+, K^+) Reaction." In: *Phys. Rev. C* 38 (1988), pp. 1322–1334. DOI: 10.1103/PhysRevC.38.1322.

[111] D. J. Millener, C. B. Dover, and A. Gal. "Lambda Nucleus Single Particle Potentials." In: *Phys. Rev.* C38 (1988), pp. 2700–2708. DOI: 10.1103/PhysRevC.38.2700.

[112] Y. Yamamoto, H. Bando, and J. Zofka. "On the Λ Hypernuclear Single Particle Energies." In: *Prog. Theor. Phys.* 80 (1988), pp. 757–761. DOI: 10.1143/PTP.80.757.

ACKNOWLEDGMENTS

I would like to express my gratitude to Prof. Dr. Norbert Kaiser for giving me the opportunity to write this thesis under his supervision. The countless discussions with him and Prof. Dr. Wolfram Weise decisively shaped this work into what it has become, which I'm very grateful for. I would like to thank Dr. Johann Haidenbauer for insightful conversations. I am very thankful to Dr. Stefan Petschauer for providing insights, notes, and code at the start of the project. Thanks to all my colleagues, in particular Susanne Strohmeier, for the enjoyable working atmosphere.

In terms of financial support, I would like to thank the Sino-German CRC 110 "Symmetries and the Emergence of Structure in QCD" by DFG and NSFC, the Excellence Cluster "Origin and Structure of the Universe", the Excellence Cluster ORIGINS, the TUM Graduate School, and the Wilhelm und Else Heraeus-Stiftung.

I am deeply grateful to my family for constantly providing support throughout the years. I would like to thank my friends in Gelsenkirchen for the enjoyable time spent together. Special thanks go to my best friends for the emotional support. Walking around with my friends on campus for hours has always been a pleasure. I would like to thank my housemates for the countless fun evenings. Last but not least, I want to give a shout-out to all my colleagues on The Silph Road and especially The Silph Research Group, which all make this project such an amazing experience.